Design and Characterisation of Nanostructured Gradient Index Lenses

Florian Hudelist

Submitted for the degree of Doctor of Philosophy

Heriot-Watt University
School of Engineering and Physical Sciences

May 2010

Abstract

The design and characterisation of nanostructured gradient index lenses is investigated in this thesis. Nanostructured gradient index materials achieve their refractive index profile by creating a pattern with feature sizes of $\lambda/5$ and smaller from two glasses with different refractive indices. These structures are fabricated by the stack-and-draw technology generally used for photonic crystal fibres. The rigorous theoretical analysis is performed with the Fourier modal method or the finite difference time domain algorithm. A comprehensive introduction of the Fourier modal method for one and two dimensional gratings is given. Due to the inherit periodicity of the Fourier modal method, an algorithm to calculate the transmitted field of isolated non-periodic lamellar gratings is developed and tested experimentally with a multi layer lens grating in the microwave regime. Furthermore, the field stitching method for the analysis of large two dimensional gratings with very small feature sizes is developed. The numerical performance is tested with a diffractive element consisting of 32×32 pixels and shown to reduce the required memory as well as the computation time by more than an order of magnitude in certain configurations. Considerations of symmetries in the grating structure are also included in the derivation of the field stitching method. The effective medium theory for nanostructured gradient index materials is introduced which allows to describe nanostructured materials with the equations for standard gradient index lenses. The stack-and-draw fabrication process is described including the choice of glass types, assembly and drawing of the preforms. For the design of the required binary pattern, the simulated annealing algorithm is used in conjunction with the effective medium theory. In order to provide experimental evidence of the simulations, two lenses were assembled from PTFE rods with a diameter of 6 mm and characterised in the microwave regime at $\lambda = 3\,\mathrm{cm}$. It is shown that with this wavelength to feature size ratio, the nanostructured gradient index lenses can have properties nearly identical to conventional gradient index lenses. Finally, a spherical and an elliptical nanostructured microlens are characterised in the optical regime. On the elliptical microlens, phase and intensity measurements are performed and compared to simulations obtained with the Fourier modal method.

Acknowledgements

I would like to thank Prof. Mohammad Taghizadeh, my supervisor, for recruiting me into the Diffractive Optics Group at Heriot-Watt University and giving me the chance to enter the field of diffractive optics. I also thank Andrew Waddie for his for his help with programming issues and many discussions about numerical problems. From the University of Warsaw I thank Ryszard Buczynski, who was closely involved in my research on microlenses. Furthermore I thank Jedrzej Nowosielski for designing the microlenses, Professor Lindlein from the University of Erlangen for allowing me to perform the phase measurements of the elliptical microlens in his laboratory and George Goussetis for his help with the microwave experiments.

My greatest thanks go to my parents who made all this possible with their continuous support. Without their moral encouragement and financial help I would have not been able to come to Scotland in the first place. Also thank you for your understanding for my decision to explore the world even further and move on to China.

In addition to that I have had a lot of personal support from many friends, too many to name individually, that is much appreciated. Last but not least I thank coffee for keeping me awake for so many hours.

ACADEMIC REGISTRY
Research Thesis Submission

Name*:*	Florian Hudelist		
School/PGI:	School of Engineering and Physical Sciences		
Version: *(i.e. First, Resubmission, Final)*	Final	Degree Sought (Award **and** Subject area)	Ph.D, Physics

Declaration

In accordance with the appropriate regulations I hereby submit my thesis and I declare that:

1) the thesis embodies the results of my own work and has been composed by myself
2) where appropriate, I have made acknowledgement of the work of others and have made reference to work carried out in collaboration with other persons
3) the thesis is the correct version of the thesis for submission and is the same version as any electronic versions submitted*.
4) my thesis for the award referred to, deposited in the Heriot-Watt University Library, should be made available for loan or photocopying and be available via the Institutional Repository, subject to such conditions as the Librarian may require
5) I understand that as a student of the University I am required to abide by the Regulations of the University and to conform to its discipline.

* *Please note that it is the responsibility of the candidate to ensure that the correct version of the thesis is submitted.*

Signature of Candidate*:*		Date:	

Submission

Submitted By *(name in capitals):*	
Signature of Individual Submitting:	
Date Submitted:	

For Completion in Academic Registry

Received in the Academic Registry by *(name in capitals):*			
Method of Submission *(Handed in to Academic Registry; posted through internal/external mail):*			
*E-thesis Submitted (**mandatory for final theses from January 2009)***			
Signature:		Date:	

Please note this form should bound into the submitted thesis.

Updated February 2008, November 2008, February 2009

Contents

Chapter 1

Introduction

The main theme of this thesis are the design and the theoretical as well as experimental characterisation of nanostructured gradient index (NSGRIN) microlenses which have a diameter of 10 µm to 250 µm and and sub-wavelength features.

Microlenses and other micro-optical beam shapers play an important role in the ever increasing field of ultra compact optical devices and integrated optics. With the advent of optical telecommunications, such as broadband internet through optical fibres, the demand and requirements for smaller and highly accurate optical components has increased strongly. A wide range of applications for microlenses have emerged over the years. They are used for optical data interconnects where they play a crucial role for the connection of data processing units with waveguides and fibres. Other applications include 2D and 3D imaging, wavefront sensing and the collimation of beams emitted from diode lasers. Microlens arrays are used to increase the efficiency of CCD chips by focusing light onto sensitive areas of each pixel of the sensor.

In 1974, Cohen and Schneider [1] published a fabrication method for microlenses with diameters of 5 µm to 10 µm and since then a large number of fabrication technologies and applications have been developed. Today, fabrication methods for plano-convex lenses include etching, lithography, electron beam writing, ink jet fabrication and many other not so commonly used technologies. A different approach is taken for gradient index (GRIN) lenses where the refractive index is modified rather than the lens surface. The most common fabrication methods for GRIN lenses are ion diffusion and the sol gel method. With these techniques the refractive index inside a cylindrical rod is changed so that the light rays follow a curved path and intersect the optical axis at a defined focal length.

In the past years, the Diffractive Optics Group at Heriot-Watt University has developed a new fabrication technology for gradient index microlenses. The gradient index is achieved by creating a nano structured binary refractive index pattern that can be described with the effective medium theory which is hereafter also referred to

as EMT. The fabrication is based on the stack-and-draw method, which is normally used to make photonic crystal fibres. It has been adapted to generate large patterns of two different glass types that are assembled from several thousand individual rods to form an effective gradient index material. Photonic crystal fibres, in contrast, only contain typically tens to a few hundred of rods. A further important difference is that the nanostructured grin structures are not used as guiding devices but are cut to disks of typically 100 µm to 300 µm thickness to be used as phase modulators.

Such NSGRIN lenses have feature sizes of $\lambda/5$ and smaller. The interaction properties in this regime are just at the upper limit of the effective medium theory. Various different algorithms are used in the theoretical analysis of the NSGRIN lenses. Depending on the length scale on which the refractive index or the surface profile varies, the right method from a rich pool of methods and approximations has to be chosen. The methods are categorised into four main regimes: the geometric domain, the scalar domain, the rigorous domain and the effective medium domain.

The geometric domain is applied if the surfaces and refractive indices change on a macroscopic scale. The path of the light is assumed to be straight, the refraction angles are calculated with Snell's law and interference is not taken into account.

The scalar domain covers structures with feature sizes of a few wavelengths. In this regime the fields do not have to be treated vectorial and the interference pattern is calculated from the phase difference of optical paths or by propagating waves with a complex amplitude. Common methods are the angular spectrum of plane wave algorithm (ASPW), the beam propagation method and the ray tracing approach. Diffractive optical elements are usually analysed with Fourier optics. In this thesis the ASPW algorithm will be used for the free-space propagation of the transmitted light from the microlenses.

The rigorous domain is the most difficult regime to calculate the light matter interactions. In structures, with a surface or refractive index distribution that varies on dimensions similar to or smaller than the wavelength of the light, the light propagation has to be calculated by solving Maxwell's equations directly. In this case, the light cannot be assumed to be a scalar field, it needs to be described fully vectorial. Advances in this regime have brought very interesting and counterintuitive effects. Photonic crystals which have a periodic pattern of the permittivity with periods of the order of $\lambda/5$ to $\lambda/2$ have been studied extensively over the past decade. Other structures that have to be solved rigorously are metamaterials which have feature sizes smaller than photonic crystals and also include very small metallic features.

Maxwell's equations cannot be solved analytically in most cases, therefore numerical algorithms have to be applied. Especially for three dimensional simula-

tions these numerical algorithms have very high requirements for both memory and calculation time. The most common methods are the finite difference time domain (FDTD) algorithm and modal approaches such as the Fourier modal method (FMM), the coordinate transform method (C-Method) and the method of moments. In this thesis the FDTD and FMM algorithms are used to analyse the nanostructured GRIN lenses.

The effective medium domain can be applied for elements with structures that are much smaller than the wavelength of the light. Sub-wavelength gratings and finely dispersed mixtures of different materials can be treated as a homogeneous medium with macroscopic properties that are defined by the mixing parameters without having to know the exact microscopic distribution. These material mixtures can be described with electromagnetic mixing formulas such as the Maxwell-Garnett equation. The NSGRIN lenses that are introduced in chapter 4 are designed using the effective medium theory. It will be shown, that under certain circumstances the EMT is a very good approximation for these lenses. After calculating the effective refractive index distribution the light propagation can be verified with one of the above mentioned methods from the rigorous domain. Depending on the shape of the material inclusions, the permittivity is described either as a scalar or as a tensor if the mixture has birefringent properties. The form birefringence of lamellar subwavelength gratings is used for example for thin film polarisers and to create polarisation sensitive blazed gratings.

Chapter 2, contains a comprehensive introduction to the Fourier modal method. The Fourier modal method is a rigorous method to solve Maxwell's equations numerically. By finding the eigenstates of the electromagnetic field and applying the field matching conditions at each boundary between adjacent layers of the grating, the propagation properties of light through the grating can be calculated. Firstly, the one dimensional FMM for analysing multi layer lamellar gratings is derived in detail. Secondly, two algorithms to calculate the boundary conditions are presented: the transmission matrix (T-Matrix) approach and the scattering matrix (S-Matrix) approach. In the last part of Chapter 2, the derivation of the two dimensional FMM for crossed gratings is summarised. The boundary conditions can be implemented in the same way as in the one dimensional Fourier modal method.

In *Chapter 3*, the field stitching method for crossed gratings is developed, which is used for the electromagnetic analysis of large gratings with very small feature sizes. A mathematical derivation and physical assumptions are outlined. It is shown how the computational performance can be improved by exploiting symmetric features of the grating. At last, numerical verification of this algorithm is provided by comparing

the results of the field-stitching method to the solution of the standard FMM.

The concept of nanostructured gradient index lenses is introduced in *Chapter 4*. It is a very broad chapter that covers several aspects of the theoretical description, fabrication and the design of NSGIN structures. Firstly, an overview of the historic development of nanostructured optical devices is outlined. Secondly, a brief introduction to the theoretical descriptions of GRIN lenses is given, because the nanostructured materials have properties of gradient index materials. Thirdly, the fabrication technology of NSGRIN lenses, that has been developed by the Diffractive Optics Group at Heriot-Watt University, is described. It is based on the stack-and-draw method for photonic crystal fibres. The last two sections of Chapter 4 cover the design of such nano structured elements. Two dimensional lenses, such as spherical or elliptical microlenses, are designed using the effective medium theory and a simulated annealing algorithm. For the design and characterisation of multilayer lamellar sub-wavelength gratings, the FMM is used with a modified algorithm to calculate the transmitted field of non-periodic elements.

By using the scalability of Maxwell's equations, the functionality of NSGRIN lenses is tested in the microwave regime. In *Chapter 5*, a spherical and an elliptical structured lens are designed, assembled and characterised experimentally as well as theoretically. The lenses are assembled from PTFE rods and tubes with diameter $d = 6\,\mathrm{mm}$ and are illuminated by microwaves with $\lambda = 3\,\mathrm{cm}$. The signal is measured with a vectorial network analyser (VNA) from which intensity and phase information of the field can be extracted.

Chapter 6 covers the experimental and theoretical characterisation of a spherical and an elliptical microlens. The spherical microlens was fabricated to demonstrate the capability of the stack-and-draw technology to fabricate large arrays of microlenses with a wide range of diameters. The propagation of the light inside the lens is simulated with the FDTD algorithm and compared to the properties of an ideal GRIN lens. The elliptical microlens is simulated with the Fourier modal method for crossed gratings. The theoretical results are compared with experimental data obtained from two different experiments. The phase profile of the transmitted field is obtained with a Mach-Zehnder interferometer and the focusing properties are measured by imaging the intensity distribution at several planes behind the lens.

Chapter 7 contains conclusions and suggestions for future work.

Chapter 2

The Fourier Modal Method

2.1 Fourier Modal Method for Lamellar Gratings

2.1.1 Basics

In this section the Fourier modal method for lamellar gratings is reviewed. The FMM was initially introduced for sinusoidally stratified dielectric gratings by C. B. Burkhardt in 1966 [2]. It was improved by Kaspar [3] and Knop [4] to deal with arbitrary one dimensional refractive index distributions and generalised to multi layer gratings by Moharam and Gaylord [5]. It belongs to the family of modal methods such as the rigorous coupled wave algorithm (RCWA) [6–9] and the coordinate transform method (C-method) [10–12]. All modal methods are based on the Fourier expansion of the permittivity of the grating and the electromagnetic field from which the Bloch eigenmodes in each layer are calculated. A Bloch mode is the wave function of a particle in a periodic potential. It is more commonly known for electrons in crystals but it can also be applied to photons in a material with a periodic permittivity distribution. The solution of Bloch modes can be written as a superposition of plane waves.

The approach of the FMM and the RCWA is to assume the permittivity to be independent of z in each layer, whereas for the C-method a coordinate transform is applied to match the computational space with the grating surface. All structures investigated within the scope of this thesis have flat surfaces, therefore the Fourier modal method was chosen to be implemented for the simulations.

The general approach of the Fourier modal method is as follows: The Bloch modes in each layer are calculated by solving Maxwell's equations, which can then be propagated inside the accordant layer. The amplitude of each mode is calculated from the boundary conditions, i.e. the electric and magnetic field at each boundary must be the same coming from the layer above the boundary and from the layer below. In the last step, the boundary conditions are solved either with the transmittance matrix

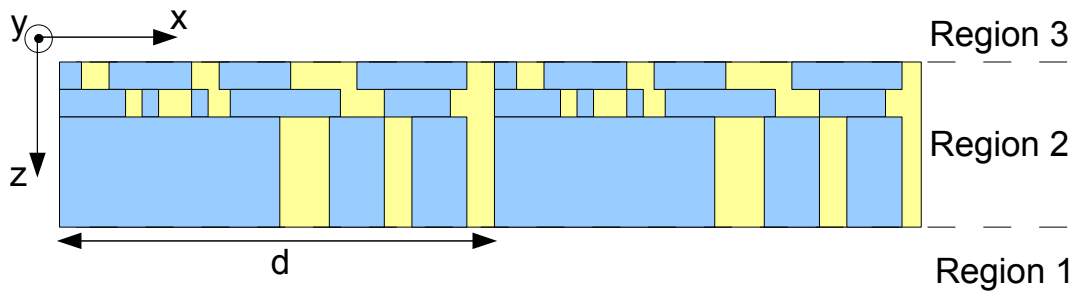

Figure 2.1: The structure of the gratings to be analysed: Each layer can have a different thickness. Within each layer the permittivity is modulated periodically in x and is constant in z. The grating is assumed to be infinite in y direction.

(T-Matrix) approach or the scattering matrix (S-Matrix) approach.

2.1.2 Differential equations

The FMM aims to solve Maxwell's equations rigorously and fully vectorial, therefore the approximations from scalar optics cannot be applied.

As for all rigorous methods, the derivation for the FMM starts with Maxwell's equations in differential form [13]:

$$\nabla \cdot \mathbf{D} = \rho \tag{2.1}$$

$$\nabla \cdot \mathbf{B} = 0 \tag{2.2}$$

$$\nabla \times \mathbf{E} = -\frac{\partial \mathbf{B}}{\partial \mathbf{t}} \tag{2.3}$$

$$\nabla \times \mathbf{H} = \mathbf{j} + \frac{\partial \mathbf{D}}{\partial \mathbf{t}} \tag{2.4}$$

where $\mathbf{E}$ is the electric field, $\mathbf{H}$ is the magnetic field; $\mathbf{D}$ and $\mathbf{B}$ are the displacement and induction fields. ρ is the charge density, $\mathbf{j}$ is the current density, ϵ_0 is the electric permittivity constant and μ_0 is the magnetic permeability constant.

The structure to be analysed is a non-magnetic multilayer grating with period p. It consists of N layers each having an arbitrary thickness t_n but the same period. The permittivity in each layer is modulated in x-direction and there is no modulation in z-direction. Furthermore, the grating is assumed to have infinite extension in y-direction with a constant refractive index. Due to this infinite translational invariance in y, the coordinate system can be reduced to a two dimensional problem with coordinates x and z. This simplifies the mathematical problem significantly. Gratings that do not have a discrete permittivity profile have to be discretised into layers and pixels.

To simplify equations 2.1-2.4, the two polarisations of the electromagnetic field as defined in figure 2.2 are treated separately. All possible polarisations of the incident field can then be written as a superposition of transverse electric (TE) and transverse

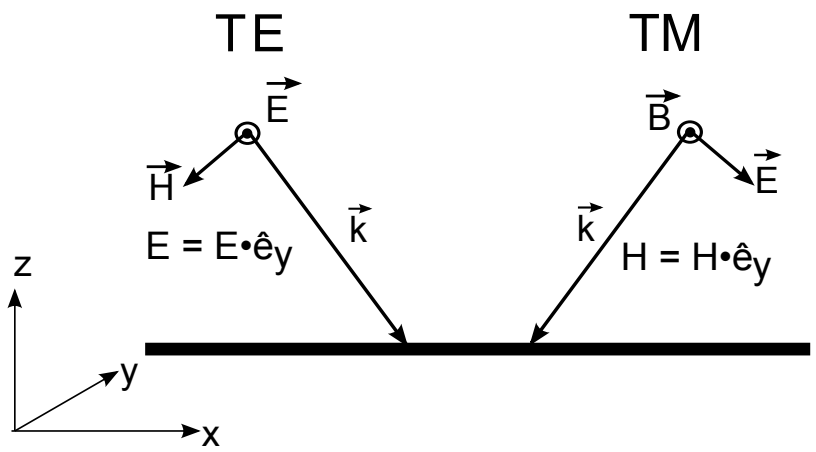

Figure 2.2: The two polarisation modes used in the calculations: In the TE case, the electric field vector is parallel to the y axis, its x and z components are zero. In the TM case the magnetic field vector is parallel to the y axis, respectively. All other polarisations of the incident light can be described as a superposition of these two polarisation modes

magnetic (TM) polarised light. If the incident field is TE polarised, the electric field vector is parallel to the y-axis and therefore only the y component is not equal to zero. In the case of TM polarisation, the magnetic field is parallel to y and the electric field has non-vanishing components in x and z. By restricting the calculations to these two polarisations, the differential equations will be reduced to only a few terms which are considerably easier to solve than the general case.

In the implementation of the FMM used in this thesis, a few simplifications and assumptions are applied to Maxwell's equations:

1. Only non-magnetic materials are considered ($\mu(r) \equiv 1$), therefore the dipole moment $\mathbf{P}$ of the molecules is the only cause for charges and currents. They are calculated by its spatial and temporal derivative:

$$\rho = -\nabla \cdot \mathbf{P} \tag{2.5}$$

$$\mathbf{j} = \frac{\partial \mathbf{P}}{\partial \mathbf{t}} \quad . \tag{2.6}$$

2. The materials are assumed to be isotropic and linear, so the dipole moment is proportional to the electric field:

$$\mathbf{P} = \chi \epsilon_\mathbf{0} \mathbf{E} \quad . \tag{2.7}$$

3. The time dependency of the incident field is $\exp(-i\omega t)$. Due to the sinusoidal time dependency of the field, the time derivative is calculated by multiplying the functions with $i\omega$.

4. The wave vector $\mathbf{k}$ of the incident light has no component in y direction ($\mathbf{k}$=$\mathbf{k}$(x,z)), i.e. the light is propagating only in the xz-plane.

5. In each layer the permittivity only changes in x direction and is constant in y and z.

With simplifications 1, 2 and 3, $\mathbf{D}$ and $\mathbf{E}$ are related in a simple way by $\mathbf{D} = \epsilon_0\epsilon_r(\mathbf{r})\mathbf{E}(\mathbf{r})$, and $\mathbf{B}$ and $\mathbf{H}$ by $\mathbf{B} = \mu_0\mathbf{H}$.

Maxwell's equations can now be reduced to:

$$\begin{aligned} \nabla \cdot [\epsilon_0\epsilon_r(\mathbf{r})\mathbf{E}] &= 0 && (2.8)\\ \nabla \cdot \mathbf{B} &= 0 && (2.9)\\ \nabla \times E &= i\omega\mathbf{B} && (2.10)\\ c^2\nabla \times \mathbf{B} &= -i\omega\epsilon_r(\mathbf{r})\mathbf{E} && (2.11) \end{aligned}$$

where $\omega = 2\pi c/\lambda_0$ is the angular frequency with a vacuum wavelength λ_0. $\epsilon_r = (1+\chi)$ is the permittivity which, in the case of non magnetic materials, is the square of the refractive index n.

It is now possible to calculate the wave equations for the electric field and the magnetic field separately. To get the wave equation for the electric field, the curl of both sides of equation 2.10 is taken.

Furthermore, if the incident light is TE polarised, equation 2.1 can be simplified even more by using simplifications 4 and 5:

$$\begin{aligned} \nabla \cdot \mathbf{D}((r)) &= \epsilon_0\nabla \cdot [\epsilon_r(\mathbf{r})(E)((r))]\\ &= \epsilon_0\mathbf{E}(\mathbf{r})\nabla\epsilon_r(\mathbf{r}) + \epsilon_0\epsilon_r(\mathbf{r})\nabla \cdot \mathbf{E}(\mathbf{r}) \qquad (2.12)\\ &= \epsilon_0\epsilon_r(\mathbf{r})\nabla \cdot \mathbf{E}(\mathbf{r}) \end{aligned}$$

The last step is possible because due to simplification 5, the gradient of $\epsilon_r(\mathbf{r})$ is orthogonal to $\mathbf{E}(\mathbf{r})$ and therefore the product is zero.

Using the vector identity

$$\nabla \times (\nabla \times \mathbf{V}) = \nabla(\nabla \cdot \mathbf{V}) - \nabla^2\mathbf{V} \qquad (2.13)$$

and substituting equations 2.8 and 2.11 into the result gives

$$\nabla^2 + k^2\epsilon_r(r)\mathbf{E} = 0 \qquad (2.14)$$

The wave equation of the magnetic field is obtained by calculating the curl of

equation 2.11 and applying 2.10 to the result. This leads to

$$\nabla \times \left(\frac{1}{\epsilon_r(r)} \nabla \times \mathbf{B} \right) - k^2 \mathbf{B} = 0 \tag{2.15}$$

Equations 2.14 and 2.15 are vector equations with three components each. These two equations for the electric and the magnetic vector field are simplified significantly when ϵ is only modulated in x-direction. Then the vector of the electric field $\mathbf{E}$ or the magnetic field $\mathbf{B}$ has only one component not equal to zero and can therefore be treated as a scalar. Thus, equation 2.14 is used for TE polarised light and equation 2.15 is used for TM polarised light. These equations need to be solved for region 1, 2 and 3. Both region 1, from which the grating is illuminated, and region 3 have a very simple solution because $\epsilon(x, z)$ is constant. In region 2, the solutions have the form of Bloch modes and have to be calculated in each layer separately by the Fourier modal method.

In the transverse electric case, only the y component of the electric field E_y is not equal to zero. With the help of Maxwell's equations both the electric and the magnetic field can be described in terms of E_y:

$$\mathbf{E}(x, z) = E_y(x, z) \cdot \hat{\mathbf{y}} \tag{2.16}$$

$$\mathbf{B}(x, z) = \frac{1}{i\omega} \left[-\frac{\partial E_y(x, z)}{\partial z} \hat{\mathbf{x}} + \frac{\partial E_y(x, z)}{\partial x} \hat{\mathbf{z}} \right] \quad . \tag{2.17}$$

In the transverse magnetic case, the magnetic field is polarised along the y axis. Both the magnetic and the electric fields can then be described as a function of B_y:

$$\mathbf{B}(x, z) = B_y(x, z) \cdot \hat{\mathbf{y}} \tag{2.18}$$

$$\mathbf{E}(x, z) = \frac{c^2}{i\omega\epsilon_r(x, z)} \left[\frac{\partial B_y(x, z)}{\partial z} \hat{\mathbf{x}} - \frac{\partial B_y(x, z)}{\partial x} \hat{\mathbf{z}} \right] \quad . \tag{2.19}$$

The corresponding wave equations 2.14 and 2.15 can now be written explicitly:

$$\left[\frac{\partial^2}{\partial x^2} + \frac{\partial^2}{\partial z^2} + k^2 \epsilon_r(x, z) \right] E_y(x, z) = 0 \tag{2.20}$$

for TE polarised light, and

$$\frac{\partial}{\partial x} \left[\frac{1}{\epsilon_r(x, z)} \frac{\partial B_y(x, z)}{\partial x} \right] + \frac{\partial}{\partial z} \left[\frac{1}{\epsilon_r(x, z)} \frac{\partial B_y(x, z)}{\partial z} \right] + k^2 B_y(x, z) = 0 \tag{2.21}$$

for TM polarised light.

Equations 2.20 and 2.21 describe the system adequately on their own, therefore it is possible to only consider the electric field in the TE case and only the magnetic field in the TM case. In TE polarisation, the magnetic field is obtained from equation

2.17 and in TM polarisation the electric field can be calculated from equation 2.19.

2.1.3 Solution in Region 1 and Region 3

Region 1 and 3 are homogeneous half spaces with permittivity $\epsilon_1 = n_1^2$ and $\epsilon_3 = n_3^2$. Equations 2.14 and 2.15 are reduced to the Helmholtz equation:

$$\left[\nabla^2 + k^2\epsilon_r\right] U(x,z) = 0 \quad , \tag{2.22}$$

where U can be the electric or the magnetic field. The solutions of this equation are a superposition of plane waves.

The incident field vector is assumed to lie in the xz-plane with an angle of incidence θ upon a lamellar grating with period d and a total thickness h. The incident field can be written as a sum of all possible plane waves.

It takes the form of a Fourier series with period d:

$$U_i = \sum_{p=-\infty}^{\infty} I_p \exp(i(\gamma_p x + r_p z)) \tag{2.23}$$

where $\gamma_p = n_1 k \sin\theta + 2\pi p d^{-1}$, $k = 2\pi n_1 \lambda^{-1}$ is the wave number and r_p is the z component of the wave vector, calculated with

$$r_p = \pm\sqrt{(n_1 k)^2 - \gamma_p^2} \quad . \tag{2.24}$$

In this case, the positive square root has to be chosen in order to ensure the correct propagation direction. The reflected field from the grating can be written similarly:

$$U_r = \sum_{p=-\infty}^{\infty} R_p \exp(i(\gamma_p x - r_p z)) \quad . \tag{2.25}$$

In region 1, the total field is the sum of the incident and the reflected field:

$$U_1 = \sum_{p=-\infty}^{\infty} \left[I_p \exp(i(\gamma_p x + r_p z)) + R_p \exp(i(\gamma_p x - r_p z))\right] \tag{2.26}$$

In region 3 the electromagnetic field is the superposition of the transmitted orders:

$$U_t = \sum_{p=-\infty}^{\infty} T_p \exp(i(\gamma_p x + t_p(z+h))) \tag{2.27}$$

with

$$t_p = \pm\sqrt{(n_3 k)^2 - \gamma_p^2} \tag{2.28}$$

In equations 2.24 and 2.28, the positive and negative roots represent upwards and

downwards travelling modes. For the further calculations, r_p and t_p are defined as the positive roots, and for downwards travelling modes $-r_p$ and $-t_p$ are used. Waves with real values of r_p or t_p are propagating modes, i.e. they contribute to the far field of the reflected field or the transmitted field respectively. Waves with an imaginary valued r_p or t_p are called evanescent waves because their amplitude decays exponentially with the distance to the grating. These modes do not carry energy and are not contributing to the far field. They can, however play an important role in near field applications such as near field microscopy [14].

The far field of gratings is often expressed by propagation angles of the reflected and transmitted diffraction orders which are calculated by

$$n_1 \sin(\phi_m) = n_1 \sin(\theta) + \frac{m\lambda}{d} \tag{2.29}$$

$$n_3 \sin(\psi_m) = n_1 \sin(\theta) + \frac{m\lambda}{d} \tag{2.30}$$

where ϕ_m and ψ_m are the propagation angles with respect to the z-axis of the m^{th} reflected order and the m^{th} transmitted order, respectively.

The energy flow of the electromagnetic field is best described by the z component of the time-averaged Pointing vector

$$\langle S_z \rangle = \frac{1}{2} \Re \left\{ E_x B_y^* - E_y B_x^* \right\} \quad . \tag{2.31}$$

where $\Re$ denotes the real part of a number.

With equation 2.31 the axial intensities of the incident, reflected and transmitted light can be calculated by using equations 2.17 and 2.19:

$$\langle S_z \rangle_i = \frac{K_1}{2\omega} \sum_{m=-\infty}^{\infty} \Re(r_m) |I_m|^2 \tag{2.32}$$

$$\langle S_z \rangle_r = \frac{K_1}{2\omega} \sum_{m=-\infty}^{\infty} \Re(r_m) |R_m|^2 \tag{2.33}$$

$$\langle S_z \rangle_t = \frac{K_3}{2\omega} \sum_{m=-\infty}^{\infty} \Re(t_m) |T_m|^2 \quad . \tag{2.34}$$

where $K_m = 1$ for TE polarisation and $K_m = (c/n_m)^2$ for TM polarisation.

In order to get the relative reflection and transmission of a grating, their values need to be divided by the incident intensity:

$$T = \frac{\langle S_z \rangle_t}{\langle S_z \rangle_i} \tag{2.35}$$

$$R = \frac{\langle S_z \rangle_r}{\langle S_z \rangle_i} \tag{2.36}$$

The total transmission or reflectivity is the sum of all relative transmission orders or reflection orders respectively.

2.1.4 Fields Inside the Grating

The grating region lies between $z = 0$ and $z = h$ and is split into N layers. The n^{th} layer extends from z_n to z_{n+1} and has a periodic permittivity distribution $\epsilon_n = \epsilon_n(x) = \epsilon_n(x+d)$ which is independent of z. Its permittivity is expressed as a Fourier series,

$$\epsilon_n(x) = \sum_{p=-\infty}^{\infty} \epsilon_{p,n} \exp\left(i2\pi px/d\right) \tag{2.37}$$

where the Fourier coefficients are given by

$$\epsilon_{p,n} = d^{-1} \int_0^d \epsilon_n(x) \exp\left(-i2\pi px/d\right) \mathrm{dx} \quad . \tag{2.38}$$

The Fourier coefficients of the inverse of the permittivity, which are needed to solve equation 2.15, are calculated by

$$\tilde{\epsilon}_{p,n} = d^{-1} \int_0^d \epsilon_n(x)^{-1} \exp\left(-i2\pi px/d\right) \mathrm{dx} \quad . \tag{2.39}$$

This integral needs to be solved numerically because the permittivity profile can in most cases not be described by an analytical function. The approach that was implemented in the simulations is to assume a piecewise constant permittivity profile. The integral reduces then to a sum of integrals over simple exponential functions.

Inside the grating region the permittivity is not constant, so the simplifications used in region 1 and 3 cannot be applied. Here, the field is expressed as a superposition of Bloch modes which are written as a sum of plane waves.

To find the Bloch modes, the Fourier expansion of the field and the permittivity is substituted into the wave equations. This will lead to a set of linear equations which can be rearranged to an eigenvalue problem. The eigenvectors of this matrix are the Bloch modes of the grating layer. Their amplitudes are determined by the condition that the field from two adjacent layers must converge to the same distribution at their boundary. For both polarisation states the differential equation that describes the field inside each layer is solved by using a separation of variables approach. A solution is formed such that

$$U(x,z) = X(x)Z(z) \quad . \tag{2.40}$$

The differential equations can therefore be solved independently for x and z.

TE polarised light

Substituting $E(x, z)$ in equation 2.20 with the form of equation 2.40 results in the following wave equation for the z dependency:

$$\frac{\mathrm{d}^2 Z}{\mathrm{dz}^2} + \alpha^2 Z(z) = 0 \quad , \tag{2.41}$$

where α is a constant that is introduced by the separation of variables approach.

As the permittivity is constant in z direction, the solution can be written as

$$Z(z) = A \exp\left[i\alpha(z - z_l)\right] + A' \exp\left[-i\alpha(z - z_h)\right] \tag{2.42}$$

where z_l and z_h are the coordinates of the lower boundary and of the higher boundary of the layer respectively. The x-part of equation 2.20 becomes

$$\frac{\mathrm{d}^2 X(x)}{\mathrm{dx}^2} + \left[k^2 \epsilon(x) - \alpha^2\right] X(x) = 0 \quad . \tag{2.43}$$

where α^2 is introduced from the second derivative by z.

By substituting equation 2.37 into equation 2.43 and assuming a solution for $X(x)$ in the form of a Fourier series

$$X(x) = \sum_{l=-\infty}^{\infty} B_l \exp(i\gamma_l x) \tag{2.44}$$

the solution of 2.43 takes the form

$$k^2 \sum_{p=-\infty}^{\infty} \epsilon_p \exp(i\beta_p x) \sum_{l=-\infty}^{\infty} B_l \exp(i\gamma_l x) - \sum_{l=-\infty}^{\infty} B_l \gamma_l^2 \exp(i\gamma_l x) = \alpha^2 \sum_{l=-\infty}^{\infty} B_l \exp(i\gamma_l x) \tag{2.45}$$

with $\gamma_l = n_0 k \sin\theta + 2\pi p d^{-1}$ and $\beta_p = 2\pi p d^{-1}$.

The exponential functions form a set of orthogonal functions, so 2.45 needs to be satisfied for each $\exp(i\gamma_l x)$ independently. By comparing the coefficients for all l, an infinite set of equations is formed:

$$\sum_{p=-\infty}^{\infty} k^2 \epsilon_{i-p} B_p - \gamma_i^2 B_i = \alpha^2 B_i \quad \forall\, i \in [-\infty, \infty] \quad . \tag{2.46}$$

This is true without restrictions if all indices go from minus infinity to plus infinity. To solve this problem numerically however, the range over which the indices go must be limited. The highest number over which the series are summed up is called the

truncation rank or truncation order. Li showed in 1999 [15] that the Bloch orders always converge to a constant and finite value if the truncation rank is high enough.

If the indices are truncated, equation 2.46 can be written in a more concise form as a matrix equation [9]:

$$\left(k^2[\![\epsilon]\!] - [\![\gamma^2]\!]\right)\vec{B} = \alpha^2\vec{B} \tag{2.47}$$

where $[\![\epsilon]\!]$ is a Toeplitz matrix with the elements $[\![\epsilon]\!]_{ik} = \epsilon_{i-k}$ and $[\![\gamma^2]\!]$ is a diagonal matrix with $[\![\gamma^2]\!]_{ii} = \gamma_i^2$. The dimension of the matrices depend on the truncation rank. If all Fourier coefficients from -N to +N are included, the dimension of the matrices is $(2N+1)\times(2N+1)$.

TM polarised light

In the TM mode, where the magnetic field is parallel to the y-axis, the wave equation for the magnetic field (eq. 2.15) is much easier to solve than the wave equation for the electric field (eq. 2.14). The solution of the simplified differential equation (eq. 2.21) in z direction is the same as in the TE polarisation mode:

$$Z(z) = A\exp\left[i\alpha(z-z_l)\right] + A'\exp\left[-i\alpha(z-z_h)\right]. \tag{2.48}$$

The differential equation for the x-part of the magnetic field is more complicated than for the electric field in the TE polarisation mode. By using the solution of the z-dependency, equation 2.21 takes the form

$$\epsilon(x)\frac{d}{dx}\left[\frac{1}{\epsilon(x)}\frac{dX(x)}{dx}\right] + \left[k^2\epsilon(x) - \alpha^2\right] = 0 \quad . \tag{2.49}$$

To solve equation 2.49, the same ansatz is used as in the TE case:

$$X(x) = \sum_{l=-\infty}^{\infty} B_l \exp(i\gamma_l x) \tag{2.50}$$

Again, after substituting the Fourier series for the field, $\epsilon(x)$ and $1/\epsilon(x)$, the obtained equations are rearranged to form an eigenvalue problem whose eigenvectors are the Bloch modes in the according layer. However, if the standard approach to substitute the Fourier coefficients is used, the solution is unstable and converges only very slowly to a constant form. This is due to the first term in 2.49 which contains a product of $\epsilon(x)$ and $\frac{d}{dx}\epsilon(x)^{-1}$. As epsilon is described in most cases by a piecewise constant function with discrete step discontinuities at the pixel edges, the two terms of this product have concurrent discontinuities. Granet et al. [16] and Lalanne et al. [17] showed independently in 1995 that a different way of calculating the Fourier coefficients of this product leads to a highly improved convergence of the eigenvalues and eigenvectors.

Generally, in order to calculate the Fourier coefficients of a function $h(x) = f(x)g(x)$ the n^{th} coefficient of $h(x)$ can be calculated from the coefficients from the two functions $f(x)$ and $g(x)$ by applying Laurent's rule [18]

$$h_n = \sum_{m=-\infty}^{\infty} f_{n-m} g_m \quad . \tag{2.51}$$

If however, $f(x)$ and $g(x)$ have two concurrent discontinuities at $x = x_p$ such that $\lim_{\delta\to 0} h(x_p+\delta) = \lim_{\delta\to 0} h(x_p-\delta)$ then a different rule needs to be applied to calculate the h_n coefficients. In this case Laurent's rule shows bad convergence at x_p, so the truncation rank has to be chosen very high in order to get the correct value $h(x_p)$.

A better convergence in this case is obtained by applying the inverse rule where the coefficients of $h(x)$ are calculated by

$$h_n^{(M)} = \sum_{m=-M}^{M} \left([\![f^{-1}]\!]_{nm}^{(M)} \right)^{-1} g_m \quad . \tag{2.52}$$

$[\![f^{-1}]\!]^{(M)}$ is a Toeplitz matrix of dimension 2M+1 which is formed by the Fourier coefficients of $f(x)$ with $[\![f^{-1}]\!]_{nm}^{(M)} = (f^{-1})_{n-m}$.

Most gratings have piecewise constant ϵ with discrete jumps between the constant sections. Therefore, the inverse rule has to be applied when substituting the Fourier series. This was proven mathematically by Li in 1996 [19]. By substituting the correct Fourier series into equation 2.49 and using a similar approach as in the TE case, a different eigenvalue problem is obtained [16, 17]:

$$[\![\epsilon^{-1}]\!]^{-1} \left(k^2 - [\![\gamma]\!] [\![\epsilon]\!]^{-1} [\![\gamma]\!] \right) \mathbf{B} = \alpha^2 \mathbf{B} \tag{2.53}$$

Like in the transverse electric case, the complete derivation of equation 2.53 requires very long algebraic calculations which goes beyond the scope of this thesis.

Applying the inverse rule to solve the differential equation for the TM mode improves the convergence of the eigenvalues significantly. Figure 2.3 shows the convergence of the smallest eigenvalue of equation 2.53 for a simple binary grating as a function of the truncation order. Using the inverse rule to calculate the Fourier coefficients leads to a much better convergence than Laurent's rule. With the inverse rule, the eigenvalue stays constant for a truncation rank larger than 30, whereas for the approach with Laurent's rule the value is still not stable for a truncation rank of 170.

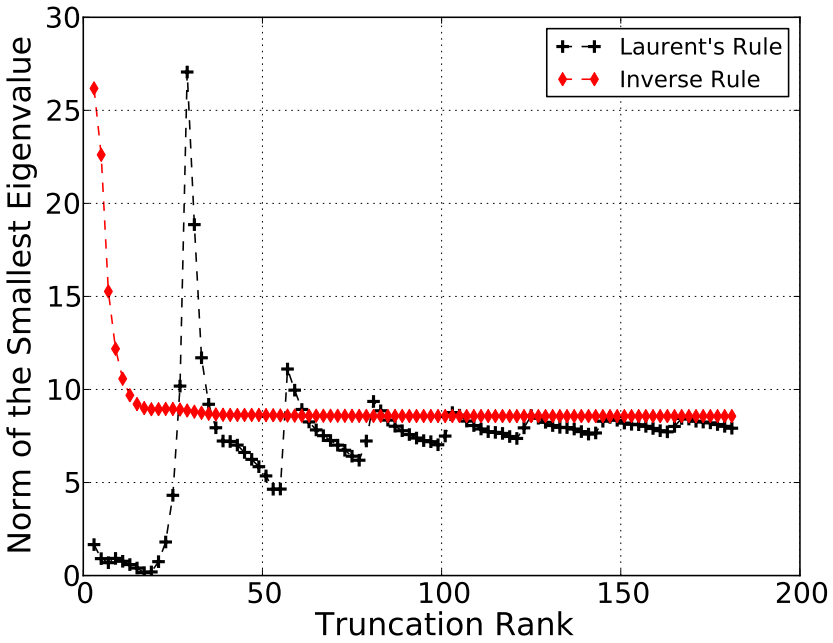

Figure 2.3: The absolute value of the smallest eigenvalue of a simple binary grating in the TM mode. The red line shows the convergence of the inverse rule, the black line shows the convergence of Laurent's rule

Calculating the field from the eigenvectors

The Bloch modes in each layer can be calculated from the eigenvectors and eigenvalues that have been determined by one of the above mentioned methods. As the eigenmatrices are a complex valued problem, the number of eigenvectors is always equal to the dimension of the matrix. The eigenvectors are denoted by $\mathbf{B_m}$ with the associated eigenvalue α_m^2. Here again, the positive α_m are used and the downwards travelling modes are denoted by $-\alpha_m$. To obtain the general solution of the field, a superposition of all Bloch modes is formed. Each mode can travel in positive and negative directions with an amplitude that has to be determined by the boundary conditions. The equation for both the electric field in TE polarisation and the magnetic field in TM polarisation is

$$U^{(n)}(x,z) = \sum_{m=1}^{2M+1} \left\{ A_m^{(n)} \exp(i\alpha_m^{(n)}(z-z_l)) + A_m'^{(n)} \exp(-i\alpha_m^{(n)}(z-z_h)) \right\} \times \sum_{p=-M}^{M} B_{m,p}^{(n)} \exp(i\gamma_p x) \quad (2.54)$$

where $A_m^{(n)}$ and $A_m'^{(n)}$ are the amplitudes of the up and down travelling waves in the n^{th} layer.

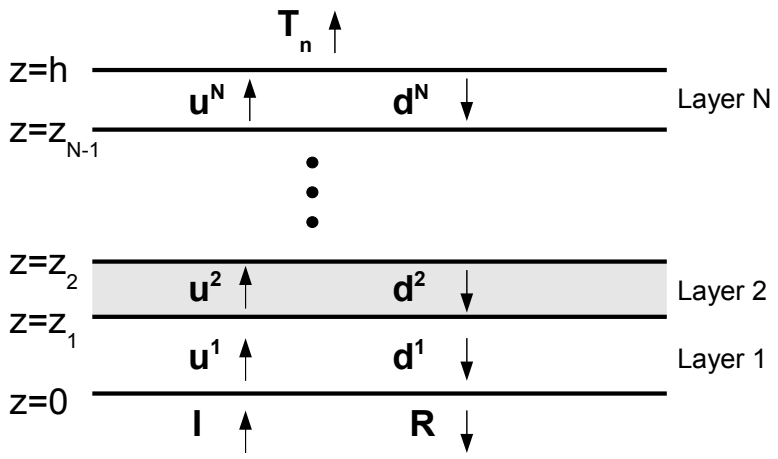

Figure 2.4: Schematic of the light propagation in the layered grating. All modes in each layer have upwards and downwards travelling amplitudes.

2.2 The Boundary Value Problem

After determining the Bloch modes in each layer, their amplitudes $A_m^{(n)}$ and $A_m^{\prime(n)}$ as well as the diffracted amplitudes R_p and T_p have to be determined. Each value depends on the incident light as well as the scattering properties of all layers. They are calculated by matching the electric and the magnetic fields at each boundary between two layers as well as between region 3 and the upper surface of the grating and between region 1 and the lower surface, respectively. Two different methods to calculate the transmission and reflection coefficients will be introduced in this section: The S-Matrix algorithm [20–24] and the T-Matrix algorithm [8, 9, 22, 25].

The T-Matrix algorithm is applied if the internal as well as the external fields are of interest. This involves a very large system of linear equations that has to be solved. The system of equations is formed by the boundary conditions at each layer interface and has the field coefficients as variables. Its solution vector contains all $A_m^{(n)}$, $A_m^{\prime(n)}$ as well as the reflection and transmission orders.

The approach of the S-Matrix algorithm is to calculate the boundary conditions by a series of matrix multiplications which are much smaller than the system of linear equations from the T-Matrix algorithm. It is therefore numerically faster, but only the reflected and transmitted fields are calculated. Both algorithms have been shown to be numerically equivalent [25] and therefore they give the same results.

2.2.1 T-Matrix Algorithm

The T-Matrix algorithm is more intuitive and easier to understand than the S-Matrix algorithm. The field coefficients of each layer are connected with the field coefficients of its neighbouring layers by the condition that the field at the interface must be the same for both layers. If the incident field is known, the system of equations can be

solved for all field coefficients. Each layer is described by $(2N+1)$ coefficients for the upwards travelling waves and $(2N+1)$ coefficients for the downwards travelling waves, respectively. The total number of unknowns in the system is $(L+1)(2N+1)$ where L is the number of layers and N is the truncation rank. To get a sufficient number of equations, both the electric and the magnetic field must be matched at the boundaries.

At the interface between region 1 and the first grating layer, the boundary conditions for the electric and the magnetic fields are:

$$U_r(x,0) + U_i(x,0) = U_1(x,0) \tag{2.55}$$

$$\frac{1}{\rho}\frac{\partial}{\partial z}\left[U_r(x,0) + U_i(x,0)\right] = \frac{1}{\sigma_1(x)}\frac{\partial U_1(x,0)}{\partial z} \tag{2.56}$$

where $\rho = \sigma_n(x) = 1$ for TE polarisation, and $\rho = n_1^2$ and $\sigma_n(x) = \epsilon_n(x)$ for TM polarisation.

The conditions applied to the boundary between the last layer and region 3 are:

$$U_L(x,h) = U_t(x,h) \tag{2.57}$$

$$\frac{1}{\sigma_L(x)}\frac{\partial U_L(x,h)}{\partial z} = \frac{1}{\tau}\frac{\partial U_t(x,h)}{\partial z} \tag{2.58}$$

where $U_t(x,h)$ is the transmitted field at $z = h$; $\tau = 1$ for TE polarisation and $\tau = \epsilon_3$ for TM polarisation.

Additional to these boundary conditions, the field also needs to be matched at each internal boundary between two adjacent layers. The boundary conditions at these boundaries are

$$U_n(x,z_n) = U_{n+1}(x,z_n) \tag{2.59}$$

$$\frac{1}{\sigma_n(x)}\frac{\partial U_n(x,z_n)}{\partial z} = \frac{1}{\sigma_{n+1}(x)}\frac{\partial U_{n+1}(x,z_n)}{\partial z} \tag{2.60}$$

Similar to the derivation of the eigenvalue equations, a set of equation is obtained from these equations by comparing the coefficients for each $\exp\{i\gamma x\}$. To simplify the notation of the boundary conditions it is helpful to define a function Ψ with

$$\Psi_p(x_p) = \begin{cases} x_p & \text{for TE polarisation} \\ \sum_{m=-N}^{N} \epsilon_{p-m} x_m & \text{for TM polarisation} \end{cases} \tag{2.61}$$

where ϵ are the Fourier coefficients of the permittivity in the associated layer and N is the truncation rank.

Interfaces to region 1 and 3

At the interface with region one, the half space from which the grating is illuminated, the superposition of the incident and reflected field must match the field of the first layer at $z = 0$:

$$I_p + R_p = \sum_{m=1}^{\infty} \left(A_m^{(1)} + A_m'^{(1)} \exp\left\{i\alpha_m^{(1)} z_1\right\}\right) B_{p,m}^{(1)} \tag{2.62}$$

$$\Psi_p^{(1)}(r_p(I_p - R_p)) = \rho \sum_{m=1}^{\infty} \alpha_m^{(1)} \left(A_m^{(1)} - A_m'^{(1)} \exp\left\{i\alpha_m^{(1)} z_1\right\}\right) B_{p,m}^{(1)} \quad . \tag{2.63}$$

At the interface to region 3, the field of layer L simply needs to be matched with the transmitted field:

$$T_p = \sum_{m=1}^{\infty} \left(A_m^{(L)} \exp(i\alpha_m^{(L)}(h - z_{N-1})) + A_m'^{(L)}\right) B_{p,m}^{(L)} \tag{2.64}$$

$$\Psi_p^{(L)}(t_p T_p) = \tau \sum_{m=1}^{\infty} \alpha_m^{(L)} \left(A_m^{(L)} \exp\left\{i\alpha_m^{(L)}(h - z_{N-1})\right\} - A_m'^{(L)}\right) B_{p,m}^{(L)} \quad . \tag{2.65}$$

Both sets of equations for region 1 and region 3 can be simplified by eliminating some variables directly. Equation 2.62 can be combined with equation 2.63 to eliminate the R_p coefficients. The same can be done with T_m in the other system. The reduction of variables results in a smaller matrix to be solved for the boundary conditions. The reflection and transmission coefficients can later be retrieved from the internal field of layer 1 and layer L.

Internal boundaries

At internal boundaries between layer n and layer $n+1$, the equations between adjacent layers are

$$\sum_{m=1}^{\infty} \left(A_m^{(n)} \exp(i\alpha_m^{(n)}(z_n - z_{n-1})) - A_m'^{(n)}\right) \Psi_p^{(n+1)}(B_{p,m}^{(n)}) = \sum_{m=1}^{\infty} \left(A_{m,n+1}^{(n+1)} + A_m'^{(n+1)} \exp(i\alpha_m^{(n+1)}(z_{n+1} - z_n))\right) B_{p,m}^{(n+1)} \tag{2.66}$$

and

$$\sum_{m=1}^{\infty} \alpha_m^{(n)} \left(A_m^{(n)} \exp(i\alpha_m^{(n)}(z_n - z_{n-1}) - A_m'^{(n)})\right) \Psi\left(B_{p,m}^{(n)}\right) = \sum_{m=1}^{\infty} \alpha_m^{(n+1)} \left(A_m^{(n+1)} - A_m'^{(n+1)} \exp(i\alpha_m^{(n+1)}(z_{n+1} - z_n))\right) \Psi\left(B_{p,m}^{(n+1)}\right) \tag{2.67}$$

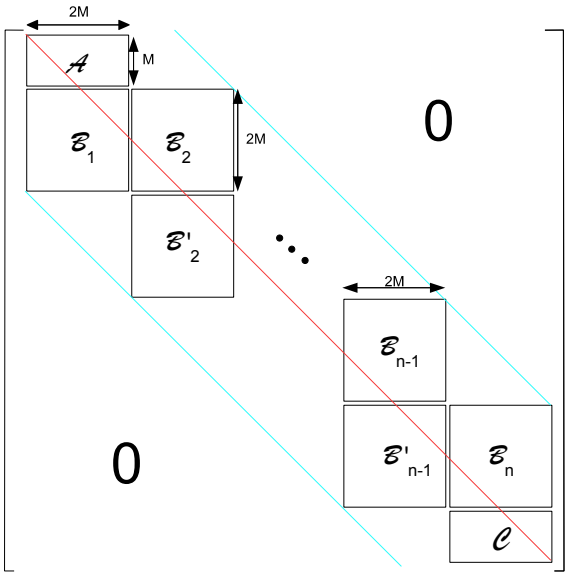

Figure 2.5: Schematic of the T-Matrix from which all field coefficients can be found. Each layer fills two blocks: $\mathcal{B}'_n$ for the upper boundary and $\mathcal{B}_n$ for the lower boundary. Fields $\mathcal{A}$ and $\mathcal{C}$ are the simplified boundary condition of the upper and the lower grating surface respectively. All matrix elements outside this band are zero.

Equations 2.62 - 2.67 form a system of linear equations for all parameters $A_m^{(n)}$, $A'^{(n)}$, T_m and R_m. In the implementation, used for the simulations in this thesis, the T_m and R_m coefficient are eliminated, which leads to a linear system of equations of the form as shown in figure 2.5. Blocks $\mathcal{A}$ and $\mathcal{C}$ contain the reduced equations extracted from equations 2.62 and 2.63, and from 2.64 and 2.65 respectively. Each layer of the grating fills two blocks $\mathcal{B}_l$ for the boundary at $z = z_l$ and $\mathcal{B}'_l$ of the boundary at $z = z_{l+1}$. These blocks are formed by equations 2.66 and 2.67 where the primed block contains the right-hand side and the unprimed block contains the left-hand side of the equations.

The resulting matrix is very sparsely filled with elements only around the diagonal (see figure 2.5). The ratio between elements equal to zero and elements not equal to zero increases with the number of layers in the grating.

Figure 2.6 shows the calculation time using a banded matrix solver and a general solver as a function of the number of layers. For a high number of layers the banded matrix solver can be as much as 5 times faster as the general solver.

2.2.2 S-Matrix Algorithm

The S-Matrix algorithm starts with the same equations as the T-Matrix algorithm, but differs in the way how the boundary conditions of the different layers are connected. There are several implementations and optimisations of the S-Matrix algorithm. In 1990, Pai and Awada [26] were the first to combine the Fourier modal method with the scattering matrix approach. It was developed further by Li [22, 23, 27] and others.

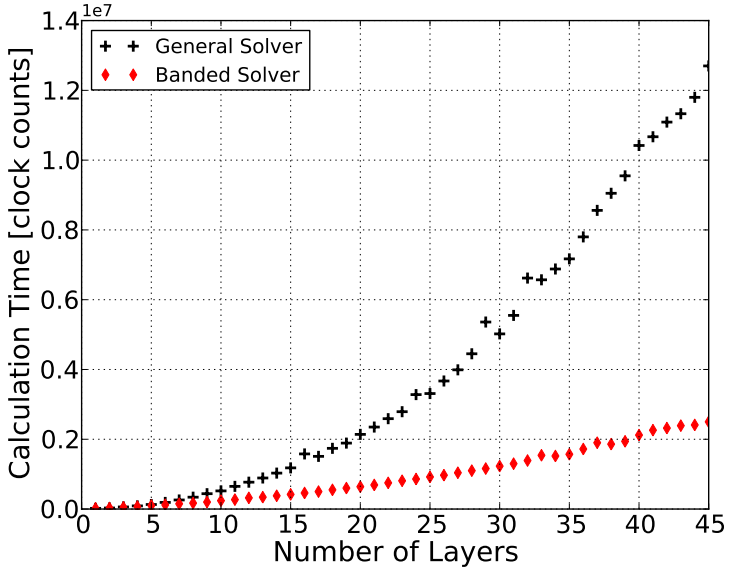

Figure 2.6: The calculation time for a fixed truncation rank $N = 30$ as a function of the number of layers. The black crosses show the calculation time for the general approach, the red diamonds show the result for the banded matrix solver.

In this section, the outline of the variant by Li [23] is introduced.

The boundary conditions between layer n and $n+1$ are written in a matrix form:

$$\begin{bmatrix} W_{11}^{(n+1)} & W_{12}^{(n+1)} \\ W_{21}^{(n+1)} & W_{22}^{(n+1)} \end{bmatrix} \begin{pmatrix} u^{(n+1)} \\ d^{(n+1)} \end{pmatrix} = \begin{bmatrix} W_{11}^{(n)} & W_{12}^{(n)} \\ W_{21}^{(n)} & W_{22}^{(n)} \end{bmatrix} \begin{bmatrix} \Phi_+^{(p)} & 0 \\ 0 & \Phi_-^{(n)} \end{bmatrix} \begin{pmatrix} u^{(n)} \\ d^{(n)} \end{pmatrix} \tag{2.68}$$

where $u^{(n)}$ and $d^{(n)}$ are column vectors containing the amplitudes of the upwards and downwards travelling modes respectively. The block matrices $W^{(n)}$ and $W^{(n+1)}$ are formed by the eigenvectors of the eigenvalue problem. In the TE mode (TM mode) W_{11} and W_{12} are formed by creating a matrix with the eigenvectors of the electric field (magnetic field) as columns. W_{21} and W_{22} are formed in the same way by using the eigenvectors of the magnetic field (electric field). Using the symmetries of the W matrix it can be written more easily in the form

$$W = \begin{bmatrix} W_1 & W_1 \\ W_2 & -W_2 \end{bmatrix} \quad . \tag{2.69}$$

$\Phi^{(n)}$ is the propagation matrix to transfer the field from the lower boundary to the upper one. Φ_+ and Φ_- are diagonal matrices with the propagation terms $\exp(i\gamma_m^{(n)} h_n)$ for the $(m,m)^{th}$ element for the upwards travelling modes and $\exp(-i\gamma_m^{(n)} h_n)$ for the downwards travelling modes respectively.

The global S matrix which connects layer n with region 1 is defined as

$$\begin{pmatrix} u^{(n)} \\ d^{(0)} \end{pmatrix} = S^{(n-1)} \begin{pmatrix} u^{(0)} \\ d^{(n)} \end{pmatrix} = \begin{bmatrix} T_{uu}^{(n-1)} & R_{ud}^{(n-1)} \\ R_{du}^{(n-1)} & T_{dd}^{(n-1)} \end{bmatrix} \begin{pmatrix} u^{(0)} \\ d^{(n)} \end{pmatrix} \quad , \tag{2.70}$$

where the sub-matrix $T_{dd}^{(n-1)}$ connects the transmitted light with the incident field from region 1 and $R_{du}^{(n-1)}$ connects the incident with the reflected field respectively. The matrices $T_{uu}^{(n-1)}$ and $R_{ud}^{(n-1)}$ are defined accordingly to the incident light from region 3.

In the case that considered in this thesis, where the grating is only illuminated from one side, $\mathbf{d}^{(n)}$ is zero, so $T_{uu}^{(n-1)}$ and $R_{du}^{(n-1)}$ will not have to be calculated. To find the S matrix for the whole grating, equation 2.68 is rearranged to get a matrix which connects $(u^{(n+1)}, d^{(n)})$ with $(u^{(n)}, d^{(n+1)})$. A multiple application of this method leads to a recursive formula for S_{L-1} which connects $(u^{(L)}, d^{(0)})$ with $(u^{(0)}, d^{(L)})$.

Li introduced a very efficient solution for the iteration by using the symmetry of the W matrices [23]. The recursion formula for $T_{dd}^{(n-1)}$ and $R_{du}^{(n-1)}$ become

$$R_{ud}^{(n)} = 1 - 2G^{(n)}\tau^{(n)} \tag{2.71}$$

$$T_{dd}^{(n)} = 2\widetilde{T}_{dd}^{(n-1)}\tau^{(n)} \quad , \tag{2.72}$$

where

$$\widetilde{T}_{dd}^{(n-1)} = T_{dd}^{(n-1)} \left(\Phi_{-}^{(n)}\right)^{-1} \tag{2.73a}$$

$$\widetilde{R}_{ud}^{(n-1)} = \Phi_{+}^{(n)} R_{ud}^{(n-1)} \left(\Phi_{-}(n)\right) \tag{2.73b}$$

$$\tau^{(n)} = \left(F^{(n)} + G^{(n)}\right)^{-1} \tag{2.73c}$$

$$F^{(n)} = Q_1^{(n)} \left(1 + \widetilde{R}_{ud}^{(n-1)}\right) \tag{2.73d}$$

$$G^{(n)} = Q_2^{(n)} \left(1 - \widetilde{R}_{ud}^{(n-1)}\right) \tag{2.73e}$$

$$Q_l^{(n)} = \left(W_l^{(n-1)}\right)^{-1} W_l^{(n)} \quad , \qquad l = 1, 2 \quad . \tag{2.73f}$$

The iteration is started with $T^{(-1)}$ set to the identity matrix and $R^{(-1)} = 0$

The comparison of the calculation time of both algorithms with increasing number of layers in figure 2.7 shows that the S-Matrix algorithm in this implementation is about 1.8 times faster than the T-Matrix algorithm. The increased speed can be explained by the difference in the size of the matrices. Many operations on small matrices are faster than one operation on a very large matrix. Thus, for applications where only the reflected and transmitted field is of interest, the S-Matrix algorithm

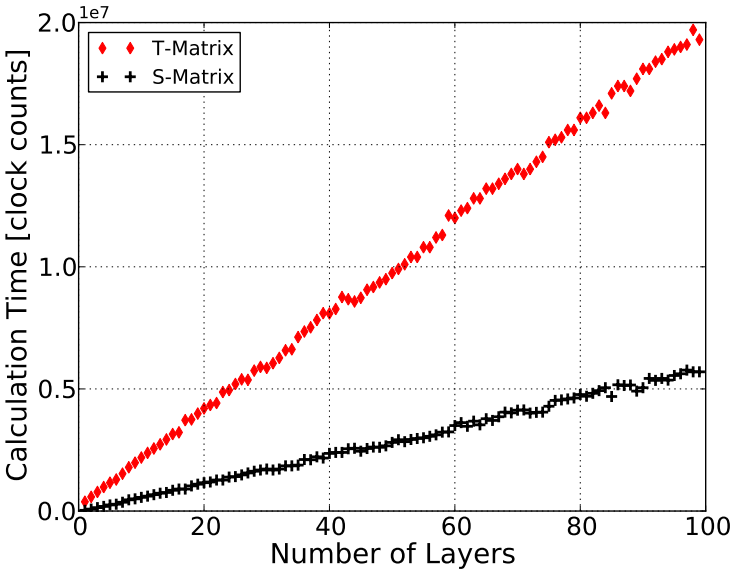

Figure 2.7: The calculation time to solve a grating with the S-Matrix algorithm (black crosses) and the T-Matrix algorithm (red diamonds). The truncation order is fixed at 15. The S-Matrix algorithm is about 1.8 times faster than the T-Matrix algorithm

is the better choice. If the internal field is of interest, the T-Matrix approach needs to be taken.

2.3 Fourier Modal Method for Crossed Gratings

The Fourier modal method for crossed gratings is numerically much more demanding than for lamellar gratings. In the eigenmode calculations the permittivity and fields need to be expanded to a two dimensional Fourier series which means that the number of wave functions is squared compared to the one dimensional Fourier modal method with the same spatial resolution. Also the separation of the polarisations is not possible any more. Depending on the features of the elements the components of x and y polarised light can be transformed into each other [28]. The idea of the three dimensional FMM is the same as for the two dimensional FMM. However, most of the simplifications used in the one dimensional FMM cannot be applied here. The explicit derivation of the equations were developed over the past 15 years and require very long calculations. This chapter gives an overview of the differential equations and how to solve them. Detailed explanations can be found in the references and go beyond the scope of this thesis.

The two dimensional Fourier modal method was firstly introduced independently by Bräuer and Bryngdahl in 1993 [29] and by Noponen and Turunen in 1994 [30]. In 1997, Lalanne published an improved formulation [31] by implementing the conclusions about the Fourier factorisation from the one dimensional FMM in TM polarisation.

With the improved method to calculate the Fourier coefficients the convergence of the method could be improved significantly. Li [32] also reformulated the FMM using the improved convergence and generalised it to skewed coordinate systems. The FMM was later generalised for materials with arbitrary permittivity and permeability tensors [32, 33].

Due to the high computational costs many efforts were made to improve the convergence of the calculation of the Bloch modes by using non-Cartesian coordinate systems and by exploiting symmetries of the grating. The convergence of the Fourier modal method was improved by Granet and Plumey with a parametric formulation of the Fourier modal method [34]. They introduced a coordinate transform that maps non-uniformly spaced points along transverse directions in the physical domain to uniformly spaced points in the transformed domain. With a suitable coordinate transform the sampling rate around transition lines of the permittivity can be increased. This is however only applicable for gratings with one or very few transition lines. Vallius and Honkanen generalised this method to multilevel profiles [35]. This method was applied successfully for gratings with only few step transitions, large gratings with many transitions however are difficult to be implemented (T. Vallius, pers. comm).

Problems with simple grating geometries can sometimes be analysed better by using a different decomposition of the fields than the Fourier transformation. Popov et al. [36] formulated the FMM on basis of an expansion to a Fourier-Bessel basis for problems with a cylindrical geometry. A more general approach was taken by Schuster et al. [37] who introduced a normal vector method in which a vector field is defined for each application.

A group theoretic approach to the FMM for various symmetries was developed by Bai and Li [38–43]. The convergence of the FMM is improved by exploiting the symmetry of the grating which induces a symmetric field. With this approach the convergence can be improved significantly. The solution of a grating with fourfold symmetry for example converges four times faster when exploiting symmetries.

In this chapter only non magnetic isotropic materials are considered. The implementation is based on the paper by Li [32] using a rectangular coordinate system.

2.3.1 Statement of the Problem

Consider a rectangular dielectric crossed grating with a finite period d_x in x-direction and d_y in y-direction respectively as shown in figure 2.8. It consists of N layers with variable thickness. The total thickness of the grating is h, the thickness of the individual layers is h_n where the index n denotes the number of the layer. Each layer can have an arbitrary, but periodic refractive index distribution which fulfills $\epsilon(x, y) = \epsilon(x + d_x, y + d_y)$ and has to be discretised in a rectangular grid with piece-

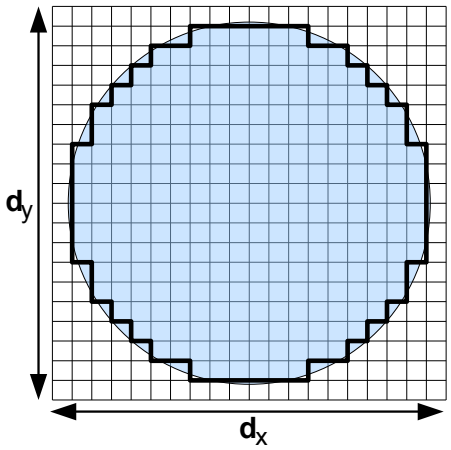

Figure 2.8: Arbitrary permittivity distributions have to be discretised to a rectangular grid before calculating the Fourier coefficients used in the FMM. In this case the discretisation method is to include all squares that are filled more than 50% by the circular structure.

wise constant permittivity. In z-direction the permittivity of the layers is constant.

The discretisation in the xy-plane as shown in figure 2.8 is necessary for the Fourier decomposition of the permittivity. For the calculation of the Fourier components, an integral over the permittivity is calculated which has to be done numerically. A finer grid causes a negligible increase of the computation time because it will only affect the values of the Fourier components. All calculations after that will be unchanged.

The grating separates two half spaces R_1 and R_3 which have a constant permittivity ϵ_1 and ϵ_3 respectively (see Fig. 2.9). From half space R_1 the grating is illuminated by a plane wave with angles of incidence θ in respect to the z-axis and φ in respect to the x-axis. The field in x and y polarisation is represented by the vectors E_x and E_y which are formed by the Fourier coefficients of the incident field.

The wave vector of incident field $\mathbf{k}^{(1)} = (\alpha_0, \beta_0, \gamma_{00})$ is formed with

$$\mathbf{k} = \alpha_0 \hat{\mathbf{x}} + \beta_0 \hat{\mathbf{y}} - \gamma_{00}^{(1)} \hat{\mathbf{z}} \quad , \tag{2.74}$$

where $\alpha_0 = k^{(1)} \sin\theta \cos\varphi$, $\beta_0 = k^{(1)} \sin\theta \sin\varphi$, $\gamma_{00}^{(1)} = k^{(1)} cos\theta$ are the components of the incident wave vector in region 1 which is denoted by the upper index. $k^{(1)} = 2\pi\sqrt{\epsilon^{(1)}\mu}\lambda^{-1}$ is the length of the incident wave vector where λ is the vacuum wave length.

The origin of the Cartesian coordinate system is the lower right corner of the unit cell.

2.3.2 Definitions

Before introducing the FMM for crossed gratings, a few notations need to be defined. These definitions will be helpful for a compact formulation of the three dimensional

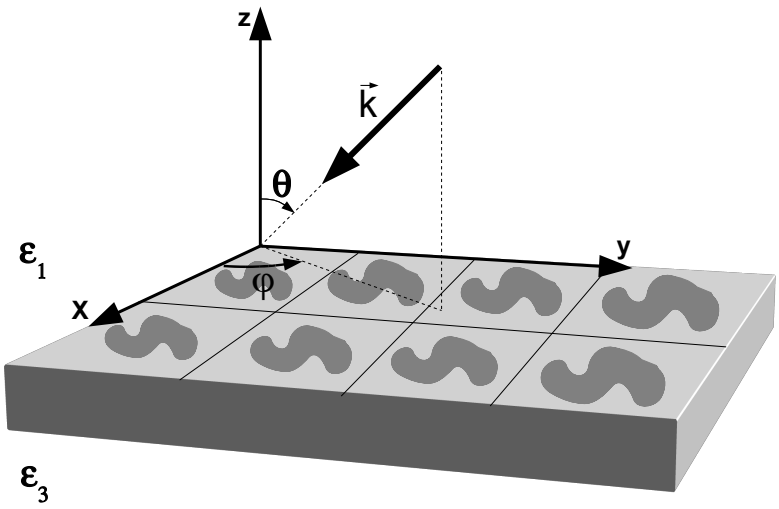

Figure 2.9: The crossed grating is illuminated from region 1 by a plane wave. The incident light vector is defined by the angles φ and θ. The permittivity is periodic along the x and y axes, with period d_x and d_y respectively. In region 1 and region 3 the permittivity is constant.

Fourier modal method.

The Fourier series of a two dimensional function is formed by a sum of complex exponential terms $\exp\left\{-i2\pi(mxd_x^{-1} + nyd_y^{-1})\right\}$ which form, as in the one dimensional case, a set of mutually orthogonal functions. The truncation of the Fourier orders is slightly more complicated than in the one dimensional case because the summation goes over two independent parameters a and b. Several truncation schemes have been suggested including square ($|m| < N_{max}$, $|n| < N_{max}$), rectangular ($|m| < A_{max}$, $|n| < B_{max}$) and circular truncation ($m^2 + n^2 < N_{max}^2$) schemes. The difference of the result for the schemes is only very little [44] therefore a square truncation is used here, which appears to be the most stable variant for many problems. In this approach the indices of both coordinates go from $-N$ to $+N$, so the number of waves to calculate with is $(2N+1)^2$.

The amplitude of each component of the Fourier series is defined by two indices n and m for the two coordinates. They can be written as a vector in row major order:

$$V_{n\cdot N+m} = A_{n,m} \quad . \tag{2.75}$$

In order to implement the inverse of the permittivity in Maxwell's equations, three different expansions have to be calculated in order to cope with the discontinuities correctly. The two-dimensional Fourier coefficients of $\epsilon(x, y)$ are given by

$$\epsilon_{mn} = \frac{1}{d_x d_y} \int_0^{d_y} \int_0^{d_x} \epsilon(x, y) \exp\left[-i2\pi(mxd_x^{-1} + nyd_y^{-1})\right] \mathrm{dx}\,\mathrm{dy} \quad . \tag{2.76}$$

For the permittivity, a Toeplitz matrix is defined analogous to the ϵ matrices in

equations 2.47 and 2.53 for the one dimensional FMM. In the two dimensional case the matrix is formed from the Fourier coefficients of a two dimensional function $\epsilon(x, y)$ by

$$[\![\epsilon]\!]_{mn,jl} = [\![\epsilon]\!]_{(m\cdot N+n),(j\cdot N+l)} = \epsilon_{m-j,n-l} \tag{2.77}$$

The matrices $\lceil\lfloor\cdot\rfloor\rceil$ and $\lfloor\lceil\cdot\rceil\rfloor$ are calculated in a two stage process. Firstly, the notations $\lceil\cdot\rceil$ and $\lfloor\cdot\rfloor$ are defined as

$$\lceil 1/\epsilon\rceil_{mn} = \frac{1}{d_x}\int_0^{d_x} \epsilon(x,y)^{-1} \exp\left[-i2\pi(m-n)xd_x^{-1}\right] \mathrm{dx} \tag{2.78}$$

$$\lfloor 1/\epsilon\rfloor_{mn} = \frac{1}{d_y}\int_0^{d_y} \epsilon(x,y)^{-1} \exp\left[-i2\pi(m-n)yd_y^{-1}\right] \mathrm{dy} \tag{2.79}$$

Secondly, by mutually nesting these two equations, $\lceil\lfloor\epsilon\rfloor\rceil$ and $\lfloor\lceil\epsilon\rceil\rfloor$ are calculated by:

$$\begin{aligned}\lfloor\lceil\epsilon\rceil\rfloor_{mn,jl} &= \lfloor\left\{\lceil 1/\epsilon\rceil^{-1}\right\}_{mj}\rfloor_{nl} \\ &= \frac{1}{d_y}\int_0^{d_y} \left\{\lceil 1/\epsilon\rceil^{-1}\right\}_{mj}(y) \cdot \exp\left[-i2\pi(n-l)yd_y^{-1}\right] \mathrm{dy}\end{aligned} \tag{2.80}$$

and

$$\begin{aligned}\lceil\lfloor\epsilon\rfloor\rceil_{mn,jl} &= \lceil\left\{\lfloor 1/\epsilon\rfloor^{-1}\right\}_{nl}\rceil_{mj} \\ &= \frac{1}{d_x}\int_0^{d_x} \left\{\lceil 1/\epsilon\rceil^{-1}\right\}_{nl}(x) \cdot \exp\left[-i2\pi(m-j)xd_x^{-1}\right] \mathrm{dx}\end{aligned} \tag{2.81}$$

If the permittivity has a distribution that cannot be described by an analytical function, then $\lfloor\lceil\epsilon\rceil\rfloor$ and $\lceil\lfloor\epsilon\rfloor\rceil$ can only be calculated for a profile which is discretised in the xy-plane as shown in figure 2.8. In the first step $\lceil\cdot\rceil$ and $\lfloor\cdot\rfloor$ have to be calculated which are still a function of y and x respectively. Here the discretisation comes into use. In this case the functions only take a finite number of values: the number of segments in y for $\lceil\cdot\rceil$ and the number of segments in x for $\lfloor\cdot\rfloor$. With these values being calculated, equations 2.80 and 2.81 can be calculated. All integrals for the ϵ matrices are solved numerically by summing up over the sub-integrals of areas with constant permittivity.

2.3.3 Eigenvalue equation for crossed gratings with rectangular lattice vectors

Fields in Region 1 and 3

In the half-spaces R_1 and R_3 the refractive index is constant. Each electromagnetic plane wave with the right period, which is given by the grating's size, can propagate.

In R_1, the half-space from which the grating is illuminated by a plane wave, the field is a superposition of the incident and the reflected waves. The plane wave representation of $E^{(1)}$ is

$$E_\sigma^{(1)}(r) = I_\sigma \exp\left[i(\alpha_0 x + \beta_0 y - \gamma_{00}^{(1)} z)\right] + \sum_{m,n=-\infty}^{\infty} R_{\sigma mn} \exp\left[i(\alpha_m x + \beta_n y - \gamma_{mn}^{(1)} z)\right], \qquad (z < 0). \quad (2.82)$$

I_σ is the incident field amplitude, $R_{\sigma mn}$ are the reflection coefficients from the grating and σ denotes the polarisation which can either be x or y.

In region 3, only the light that is transmitted through the grating needs to be accounted for:

$$E_\sigma^{(3)}(r) = \sum_{m,n=-\infty}^{\infty} T_{\sigma mn} \exp\left[i(\alpha_m x + \beta_n y - \gamma_{mn}^{(3)} z)\right], \qquad (z > h). \quad (2.83)$$

$T_{\sigma mn}$ are the field amplitudes of the transmitted light. The spatial frequencies in the Fourier factorisation are

$$\alpha_m = \alpha_0 + 2\pi m d_x^{-1} \quad (2.84)$$

$$\beta_n = \beta_0 + 2\pi n d_y^{-1} \quad (2.85)$$

$$\gamma_{mn}^{(1,3)} = \pm\sqrt{(k^{(1,3)})^2 - \alpha_m^2 - \beta_n^2} \quad . \quad (2.86)$$

The sign of $\gamma_{mn}^{(1,3)}$ is chosen so that

$$\Re(\gamma_{mn}^{(1,3)}) + \Im(\gamma_{mn}^{(1,3)}) > 0 \quad (2.87)$$

where $\Re$ is the real part and $\Im$ is the imaginary part of γ. It can be shown that there are always an equal number for upwards and downwards travelling modes [27]. Analogue to the one dimensional FMM, these will be written as positive or negative γ in the calculations.

Field inside the Grating Region

Inside the grating, the modes of the electromagnetic field are more complicated than in free space. The two dimensional Bloch modes have to be found by solving Maxwell's equations in each layer. They describe the coupling between the electric and magnetic fields with the curl equations:

$$\nabla \times \mathbf{E}(\mathbf{r}) = \mathbf{i}\omega\mu_\mathbf{0}\mathbf{H}(\mathbf{r}) \quad (2.88)$$

$$\nabla \times \mathbf{H}(\mathbf{r}) = -\mathbf{i}\omega\epsilon\mathbf{E}(\mathbf{r}) \quad . \quad (2.89)$$

These six equations (three vector components for each equation) describe the system completely and adequately. They can be reduced to four equations by eliminating the z component of both the electric and the magnetic fields with

$$E_z = -(i\omega\epsilon)^{-1}(\partial_x H_y - \partial_y H_x) \tag{2.90}$$
$$H_z = (i\omega\mu_0)^{-1}(\partial_x E_y - \partial_y E_x) \quad . \tag{2.91}$$

Substituting equations 2.90 and 2.91 into the remaining four equations leads to the final coupled set of differential equations [30] that have to be solved:

$$\partial_z E_x = i\omega\mu_o H_y - \partial_x \left[(i\omega\epsilon)^{-1}(\partial_x H_y - \partial_y H_x)\right] \tag{2.92}$$
$$\partial_z E_y = -i\omega\mu_0 H_x - \partial_y \left[(i\omega\epsilon)^{-1}(\partial_x H_y - \partial_y H_x)\right] \tag{2.93}$$
$$\partial_z H_x = -i\omega\epsilon E_y + (i\omega\mu_0)^{-1}\partial_x(\partial_x E_y - \partial_y E_x) \tag{2.94}$$
$$\partial_z H_y = i\omega\mu_0 E_x + (i\omega\mu_0)^{-1}\partial_y(\partial_x E_y - \partial_y E_x) \tag{2.95}$$

In a similar way as in the one dimensional FMM, an eigenvalue equation can be obtained by substituting the Fourier expansions of the Fields and the permittivity into 2.3.3a-d. The eigenvalue equation is written as

$$(FG - \mu k_0^2 \gamma^2)\begin{pmatrix} E_x \\ E_y \end{pmatrix} = 0 \tag{2.96}$$

where the F and the G matrix are defined as

$$F = \begin{bmatrix} \alpha[\![\epsilon]\!]^{-1}\beta & \mu k_0^2 - \alpha[\![\epsilon]\!]^{-1}\alpha \\ \beta[\![\epsilon]\!]^{-1}\beta - \mu k_0^2 & -\beta[\![\epsilon]\!]^{-1}\alpha \end{bmatrix} \tag{2.97}$$

$$G = \begin{bmatrix} -\alpha\beta & \alpha^2 - \mu k_0^2 \lceil\lfloor\epsilon\rfloor\rceil \\ \mu k_0^2 \lfloor\lceil\epsilon\rceil\rfloor - \beta^2 & \alpha\beta \end{bmatrix} \quad . \tag{2.98}$$

α and β are diagonal matrices containing the spatial frequencies of the basis functions. The diagonal elements are calculated by $\alpha_{mN+n} = \alpha_{m,n}$ and $\beta_{mN+n} = \beta_{m,n}$.

The four sub-matrices of the product FG can be simplified to

$$(FG)_{11} = -\mu k_0^2 \alpha[\![\epsilon]\!]^{-1}\alpha\lfloor\lceil\epsilon\rceil\rfloor - \mu k_0^2\beta^2 + \mu^2 k_0^4 \lfloor\lceil\epsilon\rceil\rfloor \tag{2.99}$$
$$(FG)_{12} = -\mu k_0^2 \alpha[\![\epsilon]\!]^{-1}\beta\lceil\lfloor\epsilon\rfloor\rceil + \mu k_0^2\alpha\beta \tag{2.100}$$
$$(FG)_{21} = -\mu k_0^2 \beta[\![\epsilon]\!]^{-1}\alpha\lfloor\lceil\epsilon\rceil\rfloor + \mu k_0^2\alpha\beta \tag{2.101}$$
$$(FG)_{22} = -\mu k_0^2 \beta[\![\epsilon]\!]^{-1}\beta\lceil\lfloor\epsilon\rfloor\rceil - \mu k_0^2\alpha^2 + \mu^2 k_0^4 \lceil\lfloor\epsilon\rfloor\rceil \tag{2.102}$$

The eigenvectors of equation 2.96 are the electric field Bloch modes of the respective layer. To get the magnetic part of the eigenvectors each eigenvector of the electric

field is transformed by

$$\begin{pmatrix} H_x \\ H_y \end{pmatrix} = \frac{1}{\mu k_0 \gamma} G \begin{pmatrix} E_x \\ E_y \end{pmatrix} \tag{2.103}$$

Homogeneous layers

In homogeneous layers, the method described above cannot be used because the inversion of matrices, when calculating the boundary conditions, results in singularities. However, in this case Maxwell's equations can be solved easily because the eigenvalue equation becomes diagonal. Here, only the $(0,0)$ coefficient of the Fourier expansion of the permittivity is not equal zero. The Fourier coefficient matrices in equation 2.77 reduce therefore to multiples of the identity matrix:

$$[\![\epsilon]\!] = \lceil \lfloor \epsilon \rfloor \rceil = \lfloor \lceil \epsilon \rceil \rfloor = \epsilon \cdot \mathrm{id} \tag{2.104}$$

The F and G matrix are then

$$F = \begin{bmatrix} \alpha\beta\epsilon^{-1} & \mu k_0^2 - \alpha^2\epsilon^{-1} \\ \beta^2\epsilon^{-1} - \mu k_0^2 & -\alpha\beta\epsilon^{-1} \end{bmatrix} \tag{2.105}$$

and

$$G = \begin{bmatrix} -\alpha\beta & \alpha^2 - \mu k_0^2 \epsilon \\ \mu k_0^2 \epsilon - \beta^2 & \alpha\beta \end{bmatrix} = -\epsilon F \quad . \tag{2.106}$$

The product FG is taking very easy form:

$$FG = \mu k_0^2 \begin{bmatrix} -\alpha^2 - \beta^2 + \mu k_0^2 \epsilon & 0 \\ 0 & -\alpha^2 - \beta^2 + \mu k_0^2 \epsilon \end{bmatrix} \quad . \tag{2.107}$$

The eigenvectors for the electric field of this diagonal matrix are the unit vectors $\hat{e}_i$ with the eigenvalues

$$\gamma_i^2 = \mu k_0^2 (-\alpha_i^2 - \beta_i^2 + \mu k_0^2 \epsilon) \tag{2.108}$$

The columns of the G matrix divided by $\mu k_0 \gamma$ become the eigenvectors of the magnetic field.

2.3.4 Boundary conditions

After finding the eigenmodes for each layer, the boundary conditions of the interfaces between adjacent layers have to be applied in order to get the field amplitude of each mode. Both methods that were introduced for the boundary conditions of the one dimensional FMM can be used with the two dimensional FMM in an analogue way. However, due to the very high number of variables, the T-Matrix approach is not practical because the computational costs even exceed the capabilities of today's high

performance computers.

In the implementation that is used for the simulations in this thesis, the S matrix algorithm is used. By writing the field coefficients of the electric and the magnetic fields in a single column vector as defined in equation 2.75, the algorithm can be used in exactly the same way as in the one dimensional FMM. To get the conditions between region one and layer 1 as well as between region 3 and layer L, the half spaces are treated as homogeneous layers to find the eigenmodes and eigenvectors of the electric and magnetic field.

The W matrices in equation 2.68 are formed by the eigenvectors of the electric and magnetic field. The W_1 matrix contains the eigenvectors of the electric field as obtained by equation 2.96, W_2 is formed in the same way by the magnetic part of the eigenvectors obtained from equation 2.103. From the eigenvalues, the propagation matrix can be calculated by

$$\Phi = \begin{bmatrix} \exp\{i\gamma_q z\} & 0 \\ 0 & \exp\{-i\gamma_q z\} \end{bmatrix} \tag{2.109}$$

where γ_q is the eigenvalue belonging to the q^{th} eigenvector.

Chapter 3

Field Stitching for Crossed Gratings

3.1 Introduction

The transition from lamellar gratings to crossed gratings and other three dimensional structures with sub wavelength feature sizes increases the demands both in computational time and memory significantly. The matrix for the same spatial resolution as in the one dimensional FMM has $(2N^2)^2$ elements compared to N^2 elements in the one dimensional case. Gratings with very small features compared to the period require a high number of Fourier orders to resolve each feature accurately. However, these calculations easily exceed the capabilities of even modern computers. 14 GB memory are just sufficient to solve gratings for a truncation order of ± 28. The calculation of eigenvalue problems has a cubic dependency of the computation time to the number of unknowns, therefore it can take up to several days to compute a crossed grating with the necessary accuracy. Due to the limited computational power, the algorithms need to be improved by considering symmetries and other simplifications or approximations.

Many efforts have been undertaken to improve the convergence of the FMM in order to get reliable results with a lower number of Fourier orders. Some of the methods, such as using symmetries or different basis functions for the decomposition of the fields, were summarised in chapter 2.3. These methods however, are not feasible for very large gratings with many small features and no symmetric properties.

To calculate the field propagation of an element large in size with many very small features, a high number of Fourier orders is required to get an accurate representation of the field as well as for the refractive index in the grating. The computational cost increases dramatically with the number of Fourier orders. With standard FMM approach the highest spatial frequency that can be resolved with these equations is $N_{\text{trunc}} \cdot 2\pi d_{x/y}^{-1}$. The higher the truncation order N_{trunc} the better the resolution. The truncation order is however limited by the available memory of the computer.

To deal with the issue of very large gratings, an approach is developed in this chap-

ter to break the one large problem into several smaller ones. This method differs from all other methods that improve the convergence of the FMM, because the implementation of the eigenmode calculations is not changed. It is a generalisation of the one dimensional field stitching method for lamellar gratings [45–47]. The large grating is split into several overlapping sub-gratings which can be solved separately by using the standard FMM or any of its other implementations. From the results of the sub-gratings, the global transmission and reflection coefficients can be calculated. The overlap of the sub-gratings ensures that no error is introduced at the edges of each small grating because only the central part of the field will be taken into account.

Due to the third power dependency of the calculation time this approach can reduce the calculation time considerably. The second advantage of this approach is that each of these sub-gratings can be solved separately one after the other which also reduces the memory requirements. If for example, four sub-gratings with side lengths half as long as a large grating are calculated, the spatial resolution of the calculations doubled in x and y. This consideration is the underlying idea of the field stitching algorithm introduced in this chapter.

In section 3.2 the equations that connect the sub-gratings with the whole structure are derived. The incident field for the sub-gratings as well as the transmitted and reflected field for the main grating are calculated.

In section 3.3 it is shown how rotation symmetries and mirror symmetries can be exploited to speed up the simulations. Sub-gratings that can be transformed into each other by a reflection or rotation only need to be solved once.

Numerical evidence of this method is given in section 3.4, by analysing a diffractive optical element consisting of 32×32 pixels. Furthermore, the convergence properties of the algorithms when using symmetries are discussed. This is done by analysing the elliptical microwave lens from chapter 5. The question of the required overlap of the sub-gratings is discussed qualitatively.

3.2 2d Field Stitching Method

3.2.1 Statement of the Problem

Consider a non magnetic crossed grating with an arbitrary distribution of the permittivity in the xy-plane $\epsilon(x, y)$. The grating can consist of several layers with $\epsilon(z)$ being constant in each of the layers. Its size d_x and d_y is large compared to the features within the grating and its thickness h. As in the Fourier modal method, the grating divides two homogeneous semi-infinite half spaces R_1 ($z < 0$) and R_2 ($z > h$) with refractive index n_1 and n_2 respectively. The electromagnetic field in R_1 and R_2 can be decomposed as a series of plane waves. Inside the grating the field is expressed by a superposition of Bloch modes which are found with the FMM. To connect the field

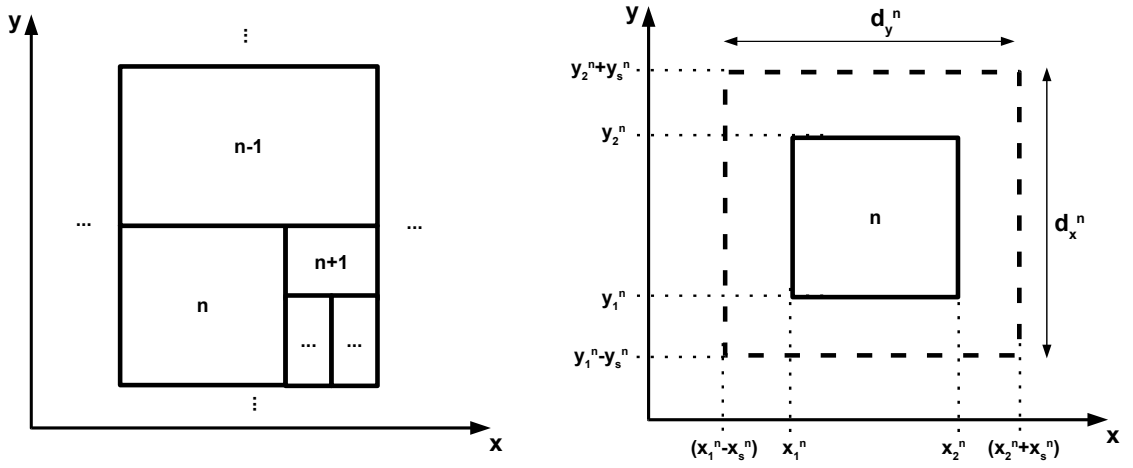

(a) (b)

Figure 3.1: (a): The large grating is split into several sub-gratings. The sub-gratings do not have to be in a regular grid but must fill the grating seamlessly. (b): Each sub-grating is increased by a frame to make it overlapping with its neighbours. For the calculations of the global field, only the core of each sub-grating is taken into account

of R_1 with R_2, a scattering matrix $\mathbf{S}$ of the grating is calculated. A monochromatic linearly polarised light from R_1 with vacuum wavelength λ and an incident angle θ to the z-axis and ϕ to the x-axis illuminates the grating.

If the grating does not scatter light strongly into the xy-plane, only areas in the immediate neighbourhood influence the field at each point in the grating. When it is possible to estimate the area that influences the transmitted field at a certain point it is enough to use only this part of the grating to calculate the field at this point. The sub-gratings must overlap to a certain extend so that the field at their edges is calculated correctly. The necessary size of the overlap depends on how strong light is scattered and on the grating thickness. This method gives the most accurate results for thin gratings and low refractive index contrasts.

3.2.2 Derivation of the transmission and reflection modes

The field stitching algorithm starts by dividing a grating into N adjacent rectangular regions that fill out the grating completely without gaps as shown in figure 3.1a. Each of the regions is extended in x and y direction to ensure that all areas of the grating that influence the field at the edges are included (Fig. 3.1b). The sub-gratings are now overlapping with their neighbours. Sub-gratings at the edge of the grating are extended on the edge side by values dependent on the structure of the large grating. In the case of a periodic grating the subgratings are extended with the index structure of the grating. If the grating will be used as a single non periodic element, the subgratings are continued by setting the refractive index constant to the index of the

surrounding material. For the calculation of the transmission and reflection orders of the whole grating only the central part of the field of each sub-grating will be taken into account.

To simplify the calculations, each sub-grating has a coordinate system attached to it with the origin in its lower left corner. The transformation from the global coordinate system to the coordinate system of the sub-gratings is denoted by the translation vector $\mathbf{r}^n$. The origin of the coordinate system of sub-grating n is

$$\mathbf{r}^n = (x_1^n - x_s^n, y_1^n - y_s^n, 0) \tag{3.1}$$

where (x_n, y_n) is the lower left corner of the non overlapping part of the grating, x_s^n and y_s^n are the overlap in x and y direction respectively. The size of sub-grating n is

$$d_x^n = (x_2^n + x_s^n) - (x_1^n - x_s^n) \tag{3.2}$$

$$d_y^n = (y_2^n + y_s^n) - (y_1^n - y_s^n) \tag{3.3}$$

where x_2^n and y_2^n is the upper limit of the non overlapping area. The coordinates of each vector and dimension are illustrated in figure 3.1b.

The spatial frequencies in the computational cell are

$$\begin{aligned} \mathbf{k}_{pq} &= (\alpha_p, \beta_q) \\ &= (\alpha_0 + 2\pi p d_x^{-1}, \beta_0 + 2\pi q d_y^{-1}) \end{aligned} \tag{3.4}$$

for the large grating and

$$\mathbf{k}_{pq}^n = (\alpha_0 + 2\pi p (d_x^n)^{-1}, \beta_0 + 2\pi q (d_y^n)^{-1}) \tag{3.5}$$

for the sub-gratings. To achieve higher resolution in areas where the grating has finer features the size of the sub-gratings can be chosen smaller than in areas with coarser features. As a general rule of thumb one can say that $\left(\mathbf{k}_{pq}^n\right)_{max}$ needs to be higher than the spatial frequency of the smallest features.

The transform of the electric and magnetic field between the coordinate systems is

$$U_n(\mathbf{r}) = U(\mathbf{r} + \mathbf{r}_n) \tag{3.6}$$

where $\mathbf{r}$ defines the position within the sub-region, U_n is the electric or magnetic field representation in respect to the sub-area and U is the field representation in respect to the whole element.

The field in the nth subregion can be expressed as a Fourier expansion for the sub-region as well as for the whole grating which both have to give the same result. Equation 3.6 is used to calculate the incident modes of each sub-region. By putting

the Fourier expansion of the incident field into 3.6 relation between the big grating and the sub-grating is obtained:

$$\sum_{pq} I_{pq}^{n} \exp\left(i\mathbf{k}_{pq}^{n}\mathbf{r}\right) = \sum_{st} I_{st} \exp\left(i\mathbf{k}_{st} \cdot (\mathbf{r} + \mathbf{r}_{n})\right) \quad . \tag{3.7}$$

It has the form of a discrete Fourier transform with the Fourier coefficients I_{pq}^{n} that can be calculated by

$$I_{pq}^{n} = (d_x^n d_y^n)^{-1} \sum_{st} I_{st} \exp\left(i\mathbf{k}_{st}\mathbf{r}^{n}\right) \int_0^{d_x^n} \int_0^{d_y^n} \exp\left(i(\mathbf{k}_{st} - \mathbf{k}_{pq}^{n})\mathbf{r}\right) \mathrm{dxdy} \quad . \tag{3.8}$$

The reflection and transmission orders can be calculated as a combination of the sub-regions in a similar way by using the reverse translation relation between the coordinate systems:

$$U(\mathbf{r}) = U_n(\mathbf{r} - \mathbf{r}_n) \qquad \begin{cases} x_1^n < x < x_2^n \\ y_1^n < y < y_2^n \end{cases} \quad . \tag{3.9}$$

For this calculation it is important to choose the correct sub-region which contains $\mathbf{r}$.

When substituting the Fourier expansion of the reflected and transmitted field into equation 3.9, the transmission and reflection modes can be identified as coefficients of a discrete Fourier transform which are calculated by

$$\sum_{pq} T_{pq} \exp\left(i\mathbf{k}_{pq}\mathbf{r}\right) = \sum_{st} T_{st}^{n} \exp\left(i\mathbf{k}_{st}^{n}(\mathbf{r} - \mathbf{r}^{n})\right) \tag{3.10}$$

and

$$\sum_{pq} (R_{pq} + I_{pq}) \exp\left(i\mathbf{k}_{pq}\mathbf{r}\right) = \sum_{st} (R_{st}^{n} + I_{st}^{n}) \exp\left(i\mathbf{k}_{st}^{n}(\mathbf{r} - \mathbf{r}^{n})\right) \tag{3.11}$$

The coefficients T_{pq} can be calculated in the same manner as the I_{pq}^{n} in equation 3.8:

$$T_{st} = (d_x d_y)^{-1} \sum_{pq} T_{pq}^{n} \exp\left(i\mathbf{k}_{pq}^{n}\mathbf{r}^{n}\right) \int_0^{d_x} \int_0^{d_y} \exp\left(i(\mathbf{k}_{pq}^{n} - \mathbf{k}_{st})\mathbf{r}\right) \mathrm{dx\,dy} \tag{3.12}$$

In equation 3.12 the parameters of the correct sub-grating have to be chosen according to the x and y coordinates in the integral. Thus, the integral has to be broken up into a sum of N integrals - one for each sub-grating - to get the coefficients of the correct sub-grating for each point of the structure:

$$T_{st} = (d_x d_y)^{-1} \sum_{n} \sum_{pq} T_{pq}^{n} \exp\left(i\mathbf{k}_{pq}^{n}\mathbf{r}^{n}\right) \int_{x_1^n}^{x_2^n} \int_{y_1^n}^{y_2^n} \exp\left(i(\mathbf{k}_{pq}^{n} - \mathbf{k}_{st})\mathbf{r}\right) \mathrm{dx\,dy} \quad . \tag{3.13}$$

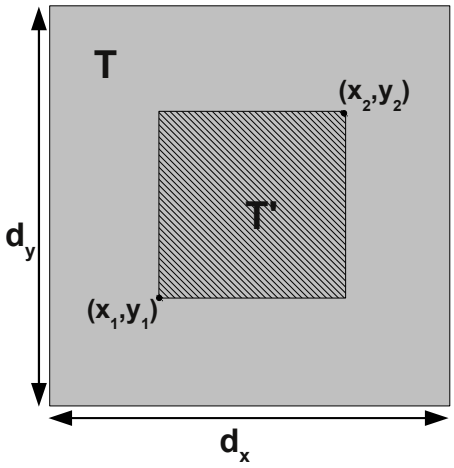

Figure 3.2: Scheme of the padding analogous to the embedding scheme for lamellar gratings. The new transmission orders are calculated for the new grating with period d_x and d_y with the transmitted field of the grating in the centre, surrounded by an area where the field amplitude is zero

The R_{st} coefficients are obtained in the same way. Here, the equation includes also the incident field orders:

$$(R_{st} + I_{st}) = (d_x d_y)^{-1} \sum_n \sum_{pq} (R^n_{pq} + I^n_{pq}) \exp\left(i\mathbf{k}^n_{pq}\mathbf{r}_n\right) \times \int_{x_1^n}^{x_2^n} \int_{y_1^n}^{y_2^n} \exp\left(i(\mathbf{k}^n_{pq} - \mathbf{k}_{st})\mathbf{r}\right) \mathrm{dx}\,\mathrm{dy} \ . \quad (3.14)$$

In most cases it is not necessary to use an irregular grid of sub-gratings. A regular grid of $n \times m$ rectangles with the same overlap p_x and p_y for all subgratings usually gives good results. This choice also simplifies the search of the ideal parameters for the number of sub-gratings and for the overlap. In the implementation in a program the grating can then easily be split up automatically, the user only needs to specify the number of rows, columns and the overlap.

3.2.3 Special case: Small modulated area in black surrounding

In order to calculate the far-field of of an isolated element, the periodic effects of the transmitted field have to be reduced. This can be done by embedding the structure in a large non-emitting padding so that light of diffracted orders reach the boundary farther away from the element.

A grating with transmission coefficients T'_m is placed in the center of a dark area as displayed in figure 3.2. The transmission coefficients T_m of the new computational cell have to be calculated from T'_m. By choosing an appropriate size of the padding, it is possible to remove the interference effects for the region of interest. The new

Fourier orders for the larger area can be calculated using the above introduced field stitching method with:

$$T_{st} = (d_x d_y)^{-1} \sum_{pq} T'_{pq} \exp\left(i\mathbf{k}'_{pq}\mathbf{r}'\right) \int_{x_1}^{x_2} \int_{y_1}^{y_2} \exp\left(i(\mathbf{k}'_{pq} - \mathbf{k}_{st})\mathbf{r}\right) \mathrm{dx}\,\mathrm{dy} \quad . \tag{3.15}$$

d_x and d_y are the dimensions of the larger area with spatial vectors $\mathbf{k}_{pq}$, and the respective primed variables refer to the small coordinate system of the element. The coordinates of the lower left and upper right corner of the element are (x_1, y_1) and (x_2, y_2) respectively. In the same manner as shown in chapter 4.4 for lamellar gratings, the transmitted field shows now reduced interference .

If the field has to be calculated for many planes it is more efficient to use the angular spectrum of plane wave (ASPW) algorithm [48] which is a different method based on the same mathematical principles. To use this algorithm, the complex field of the plane at $z = 0$ needs to be calculated and placed in the center of a matrix with zero field or a field of constant phase and amplitude in case of a transparent substrate. To propagate the field, the Fourier transform is calculated, then multiplied with a propagation term and then transformed back. Due to the availability of highly optimised fast Fourier transform algorithms, the ASPW algorithm can be more efficient than the embedding method introduced here. When using the ASPW algorithm always the whole plane is calculated, if only one or a few points in each plane are of interest the embedding method will be faster.

3.3 Exploiting Symmetries of the Structure for the Field Stitching Algorithm

Many numerical algorithms can be simplified and improved if symmetries of the problem to be solved are exploited. In the field stitching algorithm, the computation time can be reduced by a factor of two if the grating to be analysed has a two fold symmetry or even by a factor of four in case of a four fold symmetry, respectively. Most common symmetries in gratings and other phase structures are mirror symmetry, rotational symmetry and translational symmetry. If the grating is divided so that some sub-gratings can be transformed into other sub-gratings by a simple rotation, reflection or translation, their scattering matrices can also be transformed into each other. In this section, the computation of the transmission coefficients from mirror and rotational symmetric sub-gratings is discussed. The translational symmetric case is not covered because the scattering matrix will be identical to the original. The only restriction to the incident wave is that the symmetry considerations can only be applied if the grating is illuminated in normal incidence. The same restriction is valid for the group

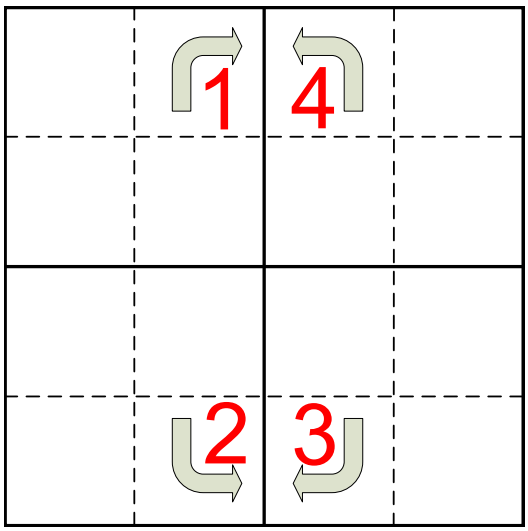

(a) A grating with mirror symmetric sub-gratings along the x and the y axis

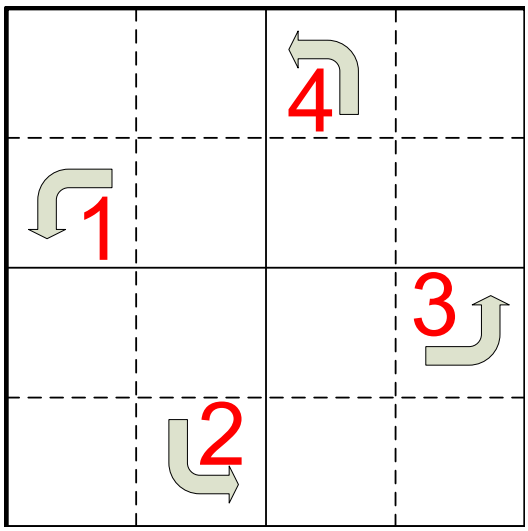

(b) A grating with rotational symmetric sub-gratings

Figure 3.3: Sub-gratings that can be transformed into each each other by rotation or reflection only need to be solved once. The transmission coefficients and reflection coefficients for all partners can be calculated by simple permutations of the elements of the scattering matrix.

theoretic approach from Bai and Li.

If the structure to be investigated shows mirror symmetry (along one or two axes) or rotational symmetry (C_2 or C_4) each group of symmetric sub-gratings only needs to be solved once. The transmission coefficients of the symmetric partners can be calculated with simple coordinate transformations. The field is written generally as $U^{(n)}(x, y)$ with the corresponding Fourier coefficients $X_{pq}^{(n)}$. U can be substituted with the reflected, transmitted and incident field. For the ease of reading, $\mathbf{k}_{pq}$, and d_x and d_y are defined as the parameters of the sub-gratings in quadrant 1. For the following calculations the grating is assumed to be illuminated from R_1 with an incident angle of $\theta = 0$.

The calculation of the transmitted and reflected fields involves several coordinate transforms of the vectors containing the Fourier coefficients of the electric field. Firstly, a derivation and notation for the required transforms are developed which are then used in the formulas of the field stitching equations. The field vectors containing the Fourier coefficients are transformed in a way that the calculated field is mirrored or rotated by multiples of 90°. When using the FMM with a square truncation scheme and truncation order M, the Field vectors have $2N^2$ elements, N^2 for x-polarisation and N^2 for y-polarisation with $N = 2M+1$. The elements of the vector are defined by 3 indices:

$$X_{\sigma mn} = X_{\sigma N^2 + mN + n} \tag{3.16}$$

where σ is 0 for x-polarisation and 1 for y-polarisation respectively. The indices m

and n go from 0 to N denoting the coefficients from $-M$ to $+M$.

If the grating has fourfold mirror symmetry (Fig. 3.3a), the transformation of the field in region 1 to regions 2, 3 and 4 are:

$$U^{(2)}(x,y) = U^{(1)}(x,-y) \tag{3.17}$$
$$U^{(3)}(x,y) = U^{(1)}(-x,-y) \tag{3.18}$$
$$U^{(4)}(x,y) = U^{(1)}(-x,y) \quad . \tag{3.19}$$

For SO4 rotational symmetry (Fig. 3.3b) the coordinate transforms are:

$$U^{(2)}(x,y) = U^{(1)}(y,-x) \tag{3.20}$$
$$U^{(3)}(x,y) = U^{(1)}(-x,-y) \tag{3.21}$$
$$U^{(4)}(x,y) = U^{(1)}(-y,x) \tag{3.22}$$

To get an equation for the relation between the coefficients, the field vectors of the the original and the symmetric sub-grating are substituted into equations 3.17 to 3.22

With the incident angle of the light being normal to the grating surface, i.e. $\theta = 0$ the spatial frequencies of the field equations can be simplified. In this case α_0 and β_0 are zero and hence $\alpha_m = -\alpha_{-m}$ and $\beta_m = -\beta_{-m}$. The field in region 2 of figure 3.3a is calculated from the field in region 1 with

$$\begin{aligned} U^{(2)}(x,y) &= \frac{1}{d_x d_y} \sum_{pq} X^{(2)}_{pq} \exp\left(i(\alpha_p x + \beta_q y)\right) \\ &= \frac{1}{d_x d_y} \sum_{pq} X^{(1)}_{pq} \exp\left(i(\alpha_p x + \beta_q (-y))\right) \\ &= \frac{1}{d_x d_y} \sum_{pq} X^{(1)}_{p,-q} \exp\left(i(\alpha_p x + \beta_q y)\right) \quad , \end{aligned} \tag{3.23}$$

which leads to the relation

$$\sum_{pq} (X^{(2)}_{pq} - X^{(1)}_{p,-q}) \exp\left(i\mathbf{k}_{pq}\mathbf{r}\right) = 0 \quad . \tag{3.24}$$

The exponential functions in equation 3.24 form a set of orthogonal functions so the coefficients of each $\exp(i\mathbf{kr})$ must add up to 0 which results in a simple equation for $X^{(2)}_{p,q}$:

$$X^{(2)}_{p,q} = X^{(1)}_{-p,q} \quad . \tag{3.25}$$

Regions 3 and 4 are solved the same way:

$$X^{(3)}_{pq} = X^{(1)}_{-p,-q} \tag{3.26}$$
$$X^{(4)}_{pq} = X^{(1)}_{-p,q} \quad . \tag{3.27}$$

In the case of rotational symmetry the coordinates are swapped, therefore the indices p and q also need to be exchanged:

$$X^{(2)}_{pq} = X^{(1)}_{q,-p} \tag{3.28}$$
$$X^{(3)}_{pq} = X^{(1)}_{-p,-q} \tag{3.29}$$
$$X^{(4)}_{pq} = X^{(1)}_{-q,p} \tag{3.30}$$

A coordinate transform $\mathcal{C}$ is defined that swaps the elements in the field vectors according to equations 3.25-3.30:

$$\mathcal{C}_{b,a}(X_{\sigma,m,n}) = X_{\sigma,n,m} \tag{3.31}$$
$$\mathcal{C}_{a,-b}(X_{\sigma,m,n}) = X_{\sigma,m,-n} \tag{3.32}$$

$\mathcal{C}_{-a,b}$, $\mathcal{C}_{-a,-b}$ and $\mathcal{C}_{-b,-a}$ are defined likewise. $\mathcal{C}_{a,b}$ is the identity.

3.3.1 Calculation of the transmission orders of symmetric sub-gratings

In this section it is shown how to calculate the transmitted field vector for sub-gratings with a symmetric partner. The calculations for the reflected field are identical, to get the equations the T is substituted by R.

Coordinate transforms

Generally, the incident light has a certain spatial distribution of amplitude and phase which means each sub-grating has a different incident light vector calculated with equation 3.8. The transmitted field of symmetric gratings differ from each other and cannot be transformed into each other by only one coordinate transform. However, it is possible to make use of the similarity of the scattering matrix. By mapping the incident field of a rotated or mirrored structure onto the original, the transmitted field of the symmetric partner can be calculated which then has to be mapped back to the correct orientation. This process consists of three steps:

Firstly, the incident field of the sub-grating to solve needs to be transformed to the coordinate system of the already solved sub-grating. The incident field is transformed by

$$\mathbf{I}' = \mathcal{C}^{\mathbf{n}\mapsto\mathbf{1}}(\mathbf{I}^{(\mathbf{n})}) \tag{3.33}$$

Secondly, the transmission coefficients are calculated by multiplying the transformed incident field vector $\mathbf{I}'$ with the scattering matrix $\mathbf{S}$ of the sub-grating in region 1:

$$\mathbf{T}' = \mathbf{S} \cdot \mathbf{I}' \tag{3.34}$$

In the last step the transmission field vector T' is transformed back to the orientation of the symmetric grating with the same transform as in step 1.

$$\mathbf{T^{(n)}} = \mathcal{C}^{\mathbf{1 \mapsto n}}(\mathbf{T}') \tag{3.35}$$

Combining all steps into one concise equation gives

$$\mathbf{T^{(n)}} = \mathcal{C}^{\mathbf{1 \mapsto n}}(\mathbf{S^{(1)}} \cdot \mathcal{C}^{\mathbf{n \mapsto 1}}(\mathbf{I^{(n)}})) \tag{3.36}$$

This way of calculating the transmission orders is much faster and more efficient than solving the scattering matrix for each sub-grating separately. The two coordinate transforms are simple permutations of a vector of size $2N_{trunc}^2$ and the matrix-vector multiplication is also computationally inexpensive. As each of the coordinate transforms can be written as a matrix-vector multiplication it would also be possible to transform the scattering matrix by multiplying it with the transform matrix from the front and back and then calculate the product of the new matrix with the incident field vector. However, this approach is numerically identical and hence gives no advantage.

3.3.2 Plane wave incident field

In most cases, the incident wave on the structure can be assumed to be a plane wave. In this case the intensity and phase of the incident wave is constant and all sub-gratings have the same incident field which is invariant to rotations and reflections. The transmission field vectors for all symmetric partners are the same, only the elements need to be swapped according to the scheme described above. The field vector of the transmitted field in regions 2 to 4 is obtained by applying the appropriate transform $\mathcal{C}$ to the T vectors of region 1.

$$T^{(n)} = \mathcal{C}^{1 \mapsto n}(T^{(1)}) \tag{3.37}$$

3.4 Numerical performance

The underlying principle of the Field stitching method is to increase the spatial resolution of the discrete Fourier transform not by increasing the number of Fourier orders but by decreasing the period of the computational cell. If, for example, a grating of

size $d_x \times d_y$ is solved using a truncation order N, the maximum spatial frequency in x is $\alpha_{max} = 2\pi N/d_x$. If however, the grating is split into $a \times a$ sub-gratings and each grating is solved individually with a truncation order N, the maximum spatial frequency in x is

$$\alpha'_{max} = N/(d_x/a) = a\alpha_{max} \tag{3.38}$$

This means for the same spatial resolution the matrices used in the calculation of the scattering matrix are much smaller. The increase of the spatial resolution is directly proportional to the decrease of the size of the sub-gratings. An effective truncation order N_{eff} is defined that corresponds to the according truncation order of the standard FMM approach which gives the same spatial resolution. For a grating that is split in $a \times a$ regular parts, the effective truncation order is

$$N_{eff} = aN \tag{3.39}$$

For a square truncation scheme with truncation rank N, the S-Matrix has a size of $(2N^2)^2$. The maximum memory requirements are therefore reduced by a factor of up to $1/M^4$ where M is the number of sub-gratings used to analyse the grating. This equation is valid for the case when the sub-gratings form a regular grid without overlapping each other. In case of an non-regular splitting of the large grating or a non-negligible overlap, the memory requirements are increased. Figure 3.4 shows the required memory of the S-Matrix in the ideal case. Each element of the matrix has a complex value with double precision, which uses 16 byte of memory. In the case of a 2×2 splitting, the size of the S-Matrix is reduced by a factor of 16 and for the 4×4 splitting by a factor of 256 compared to the standard FMM solution.

Based on the theory presented above, a computer program was built to test the numerical performance of the field stitching algorithm. The diffractive phase grating in figure 3.5 was solved with the field stitching method in various configurations. It is designed to create an array of 10×10 spots with identical intensities in the far field. As a reference, the whole structure was also solved with the standard FMM. For the field stitching method, the grating was split up into a regular grid of 2×2 and 4×4 sub-gratings. The grating parameters are $n_1 = n_2 = 1$, $\theta = \phi = 0°$, $h = 2\lambda$ and $d_1 = d_2 = 32\lambda$. Each pixel in the grating is quadratic with side length λ.

Figure 3.6a shows the convergence of three transmission orders as a function of the effective truncation order. For the FMM calculations a quadratic truncation scheme was used analysing the 10×10 beamsplitter. Due to the small pixel size, the $(0, 0)$ order has some intensity. The other two transmission orders, which are translated into spots in the far field have, as expected from the design, nearly the same values for a high enough truncation rank.

With the field stitching method, the convergence of the transmission orders can be

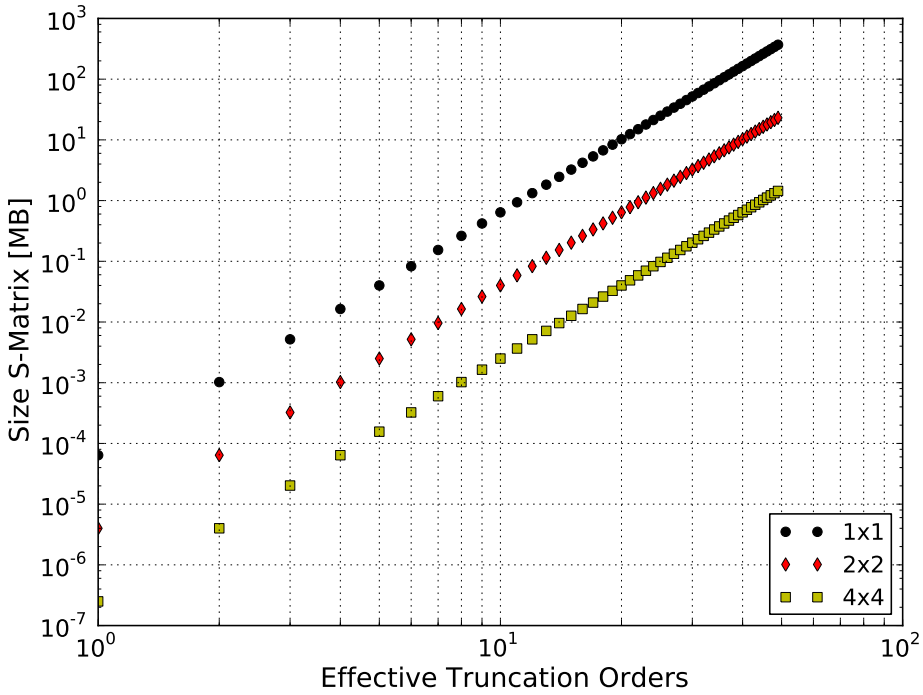

Figure 3.4: The size of the S-Matrix as a function of the effective truncation order. The 16 scattering matrices in the 4×4 can be solved in series and need much less memory at a time

improved a lot, which means a much larger grating could be solved without increasing the memory requirement because each sub-grating is solved sequentially. This diagram also provides evidence to the use of an effective truncation order. The lines using 2 by 2 sub-gratings as well as 4 by 4 sub-gratings match nearly exactly the line for the standard FMM approach.

For some structures, such as the elliptical microwave lens that is discussed in chapter 5, the transmission coefficients calculated with the FMM converge only very slowly. This structure consists of 50×50 pixels with feature sizes of around $\lambda/5$. Figure 3.6b shows the convergence of the absolute value of the $(0, 0)$ order using the field stitching algorithm with two fold mirror symmetry for 2×2, 4×4 and 6×6 sub-gratings. Here, the characteristics of the curves for the three cases start very differently. It would be impossible to analyse this structure with the normal FMM. The more the grating is split up, the more the curve seems to smooth out, the extreme oscillations get suppressed. However, even in the case where the lens is split up in 6 rows and 6 columns, the value is still not quite stable for an effective truncation rank of over 120. The thickness of this structure is 10 cm (=3.3λ) and has a size of 30 cm×30 cm. In the simulations, the overlap was chosen to be 3 cm on all four sides. Dividing the lens with side length 30 cm into 6×6 sub-gratings with 3 cm overlap means that the sub-grating size is 11 cm. Splitting the lens into even more sub-gratings would give only a small decrease of the size. A 10×10 grid reduces the side length by just 2 cm to 9 cm. A combination of the field stitching algorithm with one of the above mentioned

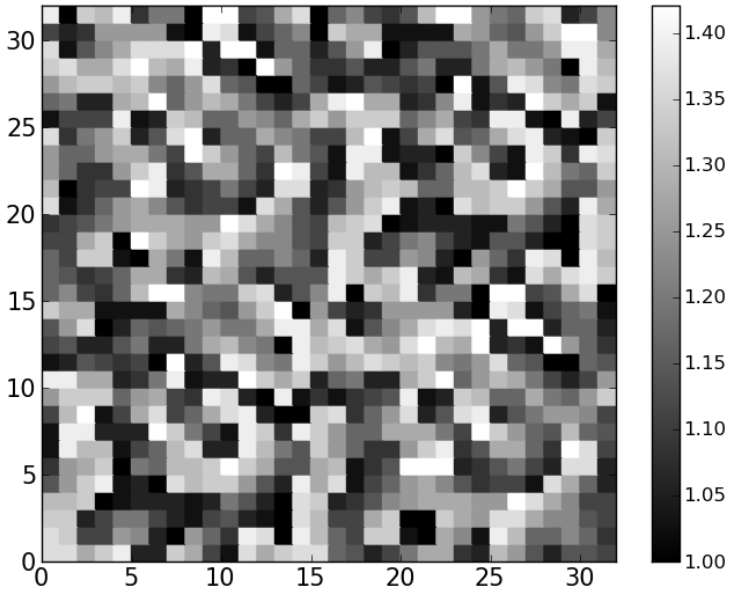

Figure 3.5: Diffractive phase grating designed as 10x10 beam splitter. The grating consists of 32x32 pixels and has 8 refractive index levels

optimisations of the FMM could possibly improve the performance further.

Calculation time

The calculation of the eigenvectors and eigenvalues takes the most time in the FMM algorithm. It increases proportional to the third power of the number of unknowns [39]. The number of unknowns is equal to twice the square of the truncation rank, therefore the calculation time is expected to be in the order of $\mathcal{O}(N_{\text{trunc}}^6)$. Depending on the optimization and parallelisation of the algorithm this dependency can be improved slightly.

The easiest case to compare the time saved by the field stitching algorithm is a square grating split up into a×a subgratings. Figure 3.7 shows a plot of the calculation time for solving the grating in figure 3.5 as a function of the effective truncation rank. It shows the curve for the standard FMM algorithm (black circles) which has the highest computation time, and for the field stitching algorithm when splitting the structure into 2×2 subgratings (red diamonds) and 4×4 subgratings (yellow squares), respectively. The calculations were performed using a computer with two Intel Xeon 3000 double core processors with a clock speed of 3GHz. The computation time difference between the standard approach and the 4×4 field stitching approach is more than two orders of magnitude.

In a double log plot the slope of the line gives the exponent of the dependency if the curve has the form $y = x^n$. In this case the exponents for the three cases are

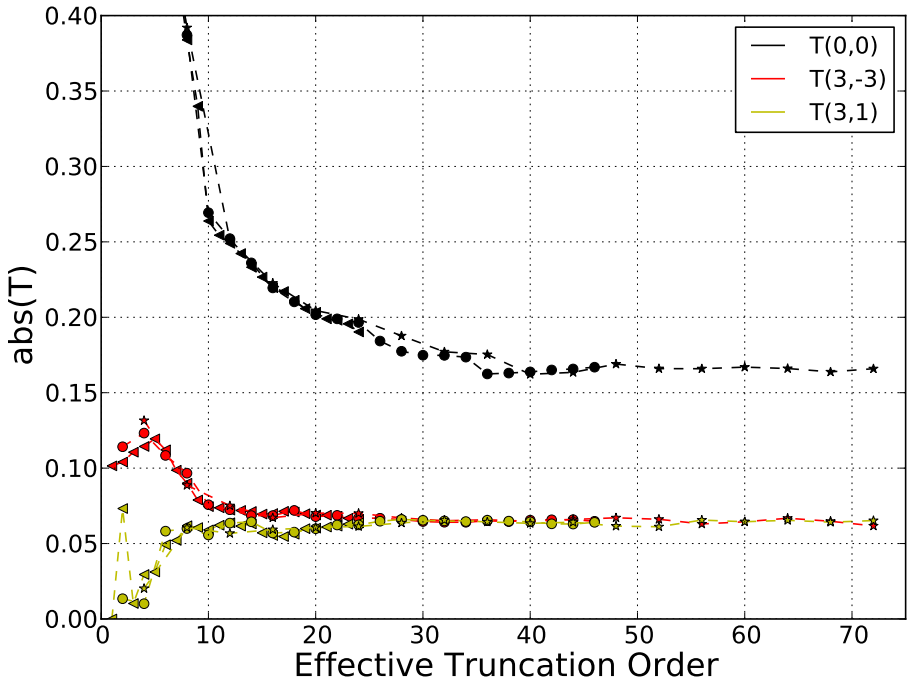

(a) The convergence of the absolute value of the $(0, 0)$ transmission order (black), the $(3, -3)$ transmission order (red) and the $(3, 1)$ transmission order (yellow), respectively. The triangles show the trend for the undivided structure, the circles for a 2×2 division and the stars for a 4×4 division

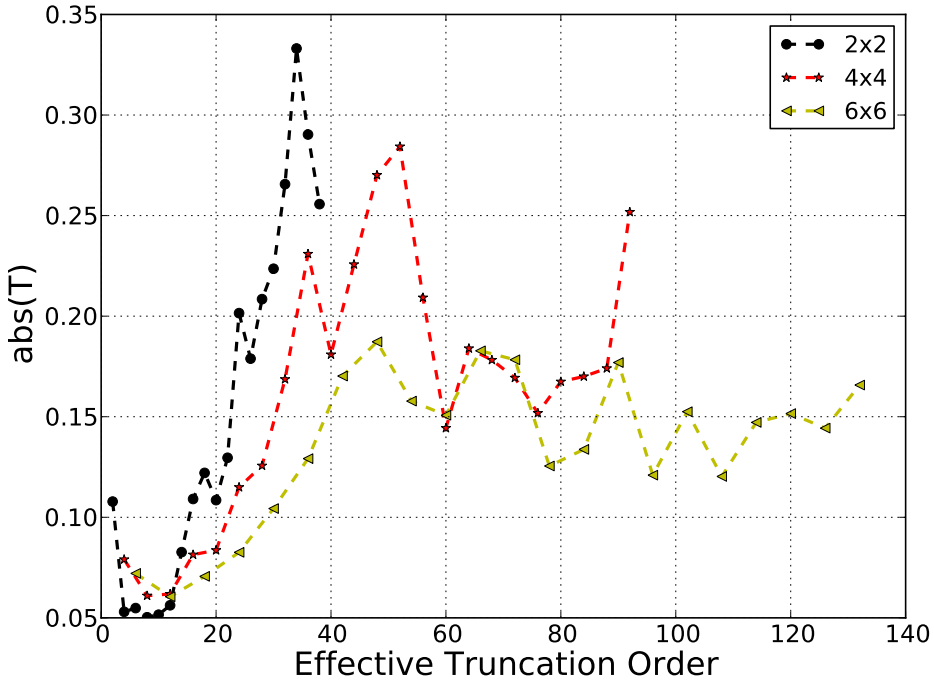

(b) The convergence of the $(0, 0)$ transmission order for 2×2 (black line), 4×4 (red line) and 6×6 (yellow line) sub-gratings. The analysed structure is the elliptical microwave lens shown in figure 5.9a

Figure 3.6: The convergence properties of the transmission coefficients for two different gratings

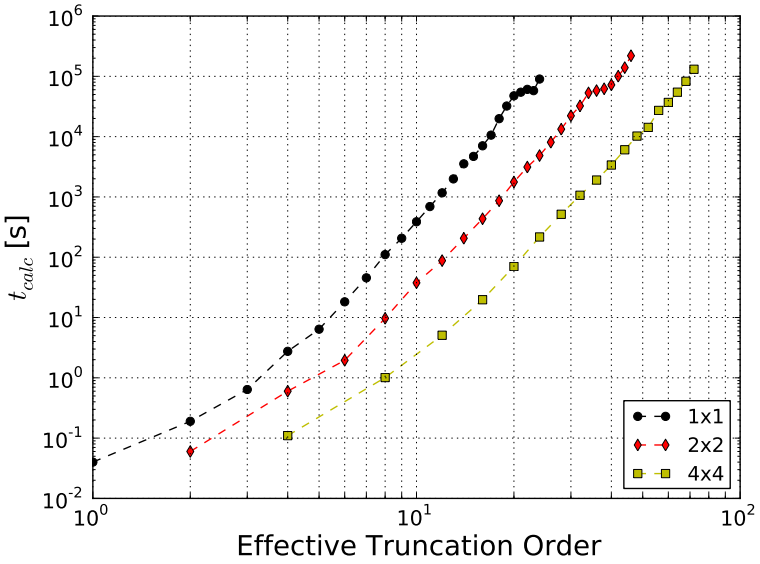

Figure 3.7: The calculation time as a function of the effective truncation order. The black circles show the trend for the undivided structure, the red diamonds and yellow squares show the trend for a 2×2 division and 4×4 division respectively

found with a least squares fitting algorithm:

$$\begin{aligned} n(1 \times 1) &= 6.26 \pm 0.021 \\ n(2 \times 2) &= 5.71 \pm 0.011 \\ n(4 \times 4) &= 5.07 \pm 0.018 \end{aligned} \tag{3.40}$$

For the standard FMM approach the N^6 dependency is nearly satisfied. As the complete time to solve the grating is measured, it is not surprising that the exponent is slightly higher as it includes several other operations. Additionally to solving the eigenmatrices, the scattering matrix also needs to be calculated. Interestingly the exponent becomes smaller the more the grating is split. The reason for this might be the reduced computational cost for the calculation of the scattering matrix which is also included in the time measurements. The numerical package used in the program is the TBCI library [49] which has a C++ implementation of the LAPACK libraries [50] and also uses some parallel optimisations.

These examples show, that the Field stitching method for crossed gratings reduces the memory requirements as well as the calculation time. If a grating shows symmetries, the calculation time is reduced by a further factor of 2 for two fold symmetries and by a factor of 4 for four fold symmetries respectively because not all sub-gratings would have to be solved.

Chapter 4

Nanostructured gradient index materials

The field of micro-optical beam shapers has developed dramatically in the past decade. Telecommunication, integrated optics and a wide field of other optical applications require ever more compact and complicated devices for their operation. The development of more and more compact devices demands constantly new technologies to fabricate the required micro-optical parts cheaply and in large numbers. The Diffractive Optics Group at Heriot-Watt University has a long history in the fabrication of micro-optical devices such as diffractive optical elements and microlenses. The new technology described here, differs strongly from any other technique that has been developed so far for the fabrication of microlenses. Not only can the new method be used for gradient index materials but it is also planned to use it for the fabrication of diffractive optical elements and tailored form birefringent structures.

Firstly, an overview of the developments and different approaches of nanostructured effective medium structures is outlined.

Secondly, an introduction on gradient index materials including their conventional fabrication and the theoretical treatment of GRIN lenses is provided.

In the third section it is shown how to combine the effective medium theory with gradient index optics and how to design a binary nano-structure with properties of a GRIN microlens.

The new technology, that was developed at Heriot-Watt University and combines the field of nanostructured effective medium devices with gradient index materials is introduced in the fourth section. It is based on the fibre draw method for all-glass photonic crystal fibres (PCF). These nanostructured gradient index materials have discrete refractive index variations on a length scale much shorter than the wavelength of the light. Therefore they can be described with electromagnetic mixing formulas [51] which are usually referred to as effective medium theory (EMT).

The last two sections cover the design of one dimensional and two dimensional structures that can be fabricated with this technology. For the 2D NSGRIN lenses, the EMT is used with a simulated annealing algorithm to find the ideal material

pattern whereas in the 1D case the simulated annealing algorithm is used with a slightly modified FMM algorithm.

4.1 Introduction

4.1.1 Nanostructured optical Elements

The field of subwavelength structured surfaces and materials already emerged in the 1980s. It covers the research on elements with a discrete structure that has a period smaller than half the wavelength of the incident light. Depending on the shape and distribution of the inclusions, these gratings act like a homogeneous medium which can be birefringent or isotropic. Diffraction effects do not occur due to the small feature size.

Yariv and Yeh reported in 1977 for the first time that gratings with subwavelength period behave like a homogeneous birefringent material [52]. It was not until six years later for researchers to come up with a method to fabricate these structures. Flanders showed in 1983 experimental results on gratings with periods of 240 nm, fabricated by using x-ray lithography and reactive ion etching [53]. In the same year Enger and Case fabricated subwavelength gratings on the surface of a quartz substrate by reactive ion etching [54]. They were, however not able to show the form birefringence and anti reflection behaviour of the gratings experimentally.

Stork at al. showed experimentally in 1991 that a subwavelength grating with a graded duty cycle acts like a natural gradient index material or a micro-prism [55]. The experiment was performed on water waves. Farn suggested in 1992 the possibility of fabricating a gradient index material by writing or etching a subwavelength grating with gradually increasing linewidth [56]. He also showed in this paper that a blazed grating with periods larger than the wavelength of the incident light could be designed by this method. Each blazed part of the grating consists of a subwavelength grating with linearly increasing linewidth. In 1993, Bräuer and Bryngdahl published a detailed theoretical analysis of the effective medium theory using the zeroth order and second order approximation of subwavelength gratings [29]. Campell and Kostuk compared rigorous calculations of sinusoidally modulated volume holograms using the rigorous coupled wave technique with results from the effective medium theory [57]. They showed that for grating periods smaller than $\lambda/8$ both theories give nearly identical results. Gratings with periods in this regime are therefore described very precisely by the EMT.

The EMT was later generalised to crossed gratings with circular or square pillar structures. Grann et al. showed in 1994, that the effective index of square structures can be obtained by calculating the average index of the unit cell using the fill factors for the different materials [58]. The validity of the approximation was verified by

comparing the EMT results with simulations from the rigorous coupled wave analysis. In 1998, Kikuta et al. confirmed the EMT for various grating symmetries such as rectangular and triangular features [59]. A very good overview on the EMT is given by Sihvola in his book on electromagnetic mixing formulas [51].

These early results inspired the development of various different structures and elements. One very interesting field is the development of polarisation sensitive diffractive optical elements (DOE). The development of such structures started only in the past decade. Pajewaki et al. suggested in 2001 a highly efficient binary diffractive element acting as a polarizing beam splitter [60]. In 2002 Yu et al. [61] fabricated a polarisation-multiplexed diffractive optical element by combining different nanostructured areas as pixels of a larger DOE. Each pixel of the diffractive element consists of either a form birefringent subwavelength grating or a pillar structure with a certain effective refractive index. By designing two polarisation insensitive nano gratings with the effective index of the ordinary and extraordinary axis of the birefringent grating, they could design the phase profiles for TE polarised light and TM polarised light independently to give two completely different images. The element was fabricated by electron beam writing and tested experimentally with a HeNe laser ($\lambda = 633\,\mathrm{nm}$). Mirotznik et al. [62] generalised this approach in 2004 by combining nanogratings with various different rectangular patterns. This approach allows the design of multiple step polarisation sensitive diffractive elements. The grating was fabricated by electron beam lithography and tested with a wavelength $\lambda = 10.6\,\mu\mathrm{m}$. Levy et al. [63, 64] used the approach of only using birefringent nano-gratings and orienting them in each pixel of the DOE by a certain angle.

As electron-beam writing is a very expensive technology, these gratings are not suitable for mass production. Moreover, the fabrication of these polarisation sensitive gratings for optical wavelengths is very challenging. To my knowledge only one group managed to fabricate polarisation-multiplexed diffractive elements for optical wavelengths.

Another field that caught the interest of many researchers is the possibility to fabricate microlenses by using a nanostructured grating. It was firstly shown by Chen and Craighead in 1996 [65] that a microlens can be fabricated from a binary micro pillar structure. This lens however could not achieve a high efficiency. Mait et al. [66, 67] introduced the fabrication of binary subwavelength diffractive lenses. The lens structure has the form of a blazed Fresnel type lens with each section being realised by a subwavelength grating with a variable duty cycle. In 2000 [68] a lens with feature sizes of 60 nm was fabricated and tested with red light. The experimental results show good agreement with simulations. Feng et al. showed in 2008 with theoretical calculations, that this method is suitable for creating lenses with a very long depth of focus [69, 70]. By varying the distribution of the pitches the depth of focus could be

increased without increasing the width of the focal spot or increasing the sidelobes.

A similar approach was taken by Lalanne et al. [71]. They use nanometre sized pillars of various sizes. Depending on the distribution and diameter of the pillars, the structure acts as a homogeneous medium with a blazed refractive index. To get a wider range of the refractive index they later combined pillar structures with holey structures where the fill factor of the material is higher [72]. For the analysis of such gratings they developed a hybrid method combining fully vectorial and scalar theories [73].

By precisely tailoring the distribution and size of micro holes in a waveguide it is possible to make mode transformers in silicon waveguides that have a very high efficiency [74, 75]. The advantage of this method is that a smooth transition of the refractive index can be realised in only one etching step.

All the fabrication methods described above depend on etching or electron beam writing. Therefore the thickness that can be achieved is very limited. Another issue of the very small features where electron beam writing has to be used is that the structures can only be fabricated one by one in series which results in very high costs per element which makes them unsuitable for mass production.

With the fabrication technology, described in this chapter, such structures can be fabricated in high volumes. Instead of glass-air structures, all-glass structures will be made which makes them more robust and stable, with the trade off that the refractive index contrast is lower.

4.1.2 Effective medium theory

In a material which is a finely dispersed mixture, the permittivity can be described as an effective quantity by averaging over volumes or areas that are large compared to the inhomogeneities and in the order of the wavelength of the incident light or smaller. The averaged permittivity is denoted by ϵ_{eff}, the effective permittivity. If inhomogeneities of the mixture also have variations on a macroscopic scale, the effective permittivity becomes a spatial distribution $\epsilon_{eff}(x, y, z)$.

$\bar{\mathbf{E}}$ and $\bar{\mathbf{D}}$ are defined as the averaged field and induction inside the material mix. Then, by definition of ϵ_{eff} [76] the relation between $\bar{D}$ and $\bar{E}$ is

$$\bar{\mathbf{D}} = \epsilon_{\mathbf{eff}} \bar{\mathbf{E}} \quad . \tag{4.1}$$

The local field can be written as the averaged field plus a perturbation $\mathbf{E} = \bar{\mathbf{E}} + \delta\mathbf{E}$ and the permittivity as $\epsilon = \bar{\epsilon} + \delta\epsilon$ with

$$\bar{\epsilon} = V^{-1} \int_V \epsilon \mathrm{dV} \quad . \tag{4.2}$$

The mean induction is calculated by

$$\bar{\mathbf{D}} = \overline{(\bar{\epsilon} + \delta\epsilon)(\bar{\mathbf{E}} + \delta\mathbf{E})} = \bar{\epsilon}\bar{\mathbf{E}} + \delta\epsilon\overline{\delta\mathbf{E}} \quad . \tag{4.3}$$

In the zero order approximation equation 4.1 leads to the equation for the effective permittivity

$$\epsilon_{eff} = \bar{\epsilon} \quad . \tag{4.4}$$

To get the second order approximation of the permittivity, the first order correction term from equation 4.3 has to be included. The effective permittivity then becomes

$$\epsilon_{eff} = \bar{\epsilon} - \frac{\overline{(\delta\epsilon)^2}}{3\bar{\epsilon}} \quad . \tag{4.5}$$

If the mixture consists of discrete regions of two materials and the fill factor of the material is known, according to reference [51], equation 4.5 can be written explicitly as

$$\epsilon_{eff} = \bar{\epsilon} - f(\epsilon_1 - \epsilon_2)\frac{\epsilon_1 - <\epsilon>}{3 <\epsilon>} \tag{4.6}$$

where ϵ_1 and ϵ_2 are the permittivities of the two materials, $<\epsilon> = \epsilon_2 + f(\epsilon_1 - \epsilon_2)$ and f is the fill factor of ϵ_1.

Equation 4.5 implies, that in structures that have a small refractive index variation with a very high spatial frequency the propagating light is only affected by an average of the permittivity. For certain configurations, the light will 'see' a smooth refractive index which can be treated like a GRIN medium even though the actual structure is discrete on a very small scale. Dependent on the length scale on which the composition of the mixture varies, the area or volume used to calculate the average permittivity $\bar{\epsilon}$, is in the order of one to three wavelengths. For structures with a binary index profile and low index contrast, the effective index profile can be calculated by

$$\epsilon_{eff}(\mathbf{r}) = \overline{\epsilon(\mathbf{r})} = f(U_r)\epsilon_1 + (1 - f(U_r))\epsilon_2. \tag{4.7}$$

ϵ_1 and ϵ_2 are the permittivities of the two materials and $f(U_r)$ is the fill factor of ϵ_1 in a certain neighbourhood U_r around point $\mathbf{r}$. In most cases the neighbourhood is chosen to be circular. For the structures that are considered later, the maximum index contrast is 1.7/1.5 which results in $(\delta\epsilon)^2$ having values in the order of $10^{-4}\epsilon_{eff}$ and therefore $\epsilon_{eff} = \bar{\epsilon}$ is assumed for further calculations.

A strict upper limit for the accuracy of this approximation cannot be made as it depends on several factors such as the pattern and the index contrast of the materials. As mentioned in the introduction, it was shown that this approximation is accurate in most cases for pixel sizes of about $\lambda/8$ and smaller [57]. Experimental results of a lens, fabricated on the basis of this theory, shows focusing for feature sizes of the

inclusions $\lambda/5$, however the diffraction losses are much higher than in an ideal lens and the peak intensity of the focus lower. In this case a rigorous treatment such as the FMM or the FDTD method [77] has to be applied to calculate the field propagation accurately.

If the distribution of the inclusions is not statistical or their shape is non-spherical, the above derived equations cannot be applied. In this case the effective permittivity can show sensitivity to the polarisation of the light. Derivations of the mixing formulas in various configurations can be found in reference [51].

4.1.3 Gradient index optics

The effect of light following a curved path in a graded index material was firstly mentioned by James C. Maxwell in 1850 [78, 79], but it took another 100 years to be investigated experimentally and explored systematically. The field of gradient index optics has emerged in the second half of the twentieth century. It describes the optical effects of materials with a gradually varying permittivity [79–81] which causes light to propagate along a curved path according to the refractive index distribution. GRIN materials are most commonly used for lenses [82–85] and waveguides [86].

The effects of gradient index optics can be experienced in the day to day life when hot and cold air is mixing. This becomes obvious in the effect of flickering when hot air rises from heaters or candles. The density of hot air is lower than the density as cold air and therefore the refractive index is decreased. Another very impressive effect are mirages that appear in hot desserts or - more familiarly - make roads appear to be wet on a hot summer day (see figure 4.1). The air close to the hot road is heated up to higher temperatures and creates a layer in which light rays that are emitted from objects near the street follow a curved path and are bent up. To the observer these rays appear as if the distant object is reflected on the street.

Conventional fabrication technologies are methods such as the diffusion based thermal ion exchange method [87–89] or the reflow sol-gel technology [84, 90]. These methods allow only very limited control over the refractive index profile which can be slightly improved with approaches such as the field-assisted ion exchange [91]. However, owing to the principle of these fabrication techniques, only very simple index variations can be achieved. The maximum index contrast Δn is typically less than 0.1 [86, 92].

Standard lenses cause focusing through refraction on their surfaces. The material is homogeneous and isotropic so light propagates along straight lines inside and outside the lens as displayed in figure 4.2a. In an ideal lens, all rays parallel to the optical axis are refracted according to Snell's law so that they have the same intercept with the optical axis which is the focal point.

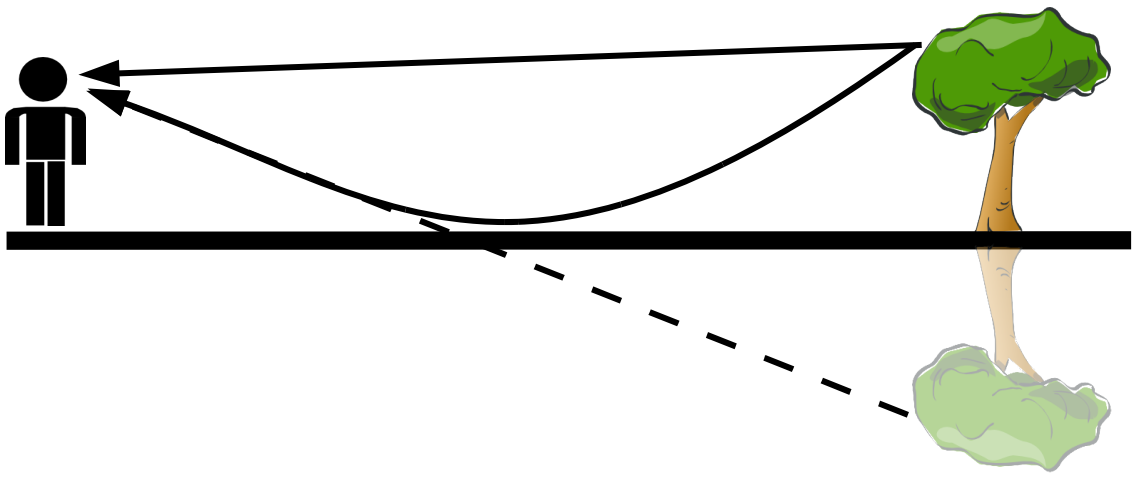

Figure 4.1: The mirage effect on hot streets. Due to the curved path of the light, the distant object appears to be mirrored on the street.

Gradient index lenses achieve focusing in a different way. They generally have flat surfaces but the index distribution is not homogeneous. Having flat surfaces on both facets is particularly important for optical interconnects in telecommunications because it can be incorporated much easier in compact systems. In special applications the surface of GRIN lenses can also be shaped to suppress aberrations.

The analytical solution for a perfect GRIN lens, where light rays follow a sinusoidal path, is the hyperbolic secant function [80]:

$$\begin{aligned} n(r) = n_{max}\,\mathrm{sech}(ar) &= \frac{2\exp(x)}{1+\exp(2x)} \\ &\approx n_{max}\left[1 - \frac{(ar)^2}{2} + \frac{5(ar)^4}{24} - \mathcal{O}(r^6)\right] \quad . \end{aligned} \tag{4.8}$$

In most applications, the refractive index profile of a radial GRIN lens [85] is defined by the second order approximation of the sech function:

$$n(r) = n_{max}\left(1 - \frac{(ar)^2}{2}\right) \tag{4.9}$$

where n_{max} is the maximum refractive index at the center of the lens, r is the distance to the centre and a is a constant. Due to the spatially varying refractive index, the phase velocity of the light depends on the position inside the lens. Therefore a plane wavefront entering the lens is getting deformed to a spherical wave which is focused at a distance f away from the back surface of the lens. In the picture of ray optics, this means that light rays describe a curved path inside the GRIN lens.

For thin GRIN lenses with $f \gg R$ where R is the lens radius, the refractive index

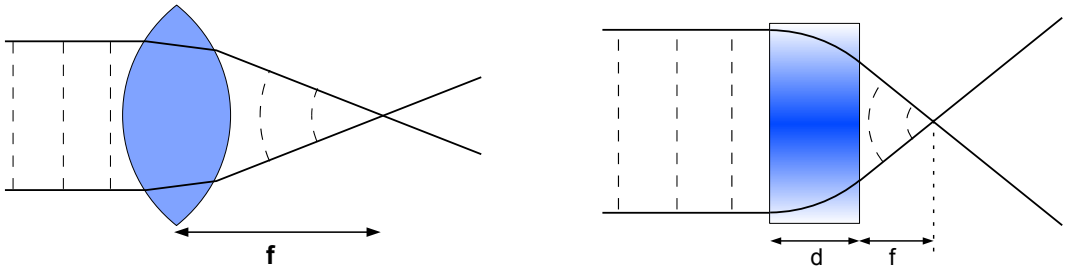

(a) Standard lens (b) GRIN lens

Figure 4.2: The focusing of a collimated beam by a standard lens and a GRIN lens. In the standard lens the light always follows a straight line, the focusing is due to refraction on the lens surface. Inside the GRIN lens the light is bend towards the optical axis which causes the focusing effect.

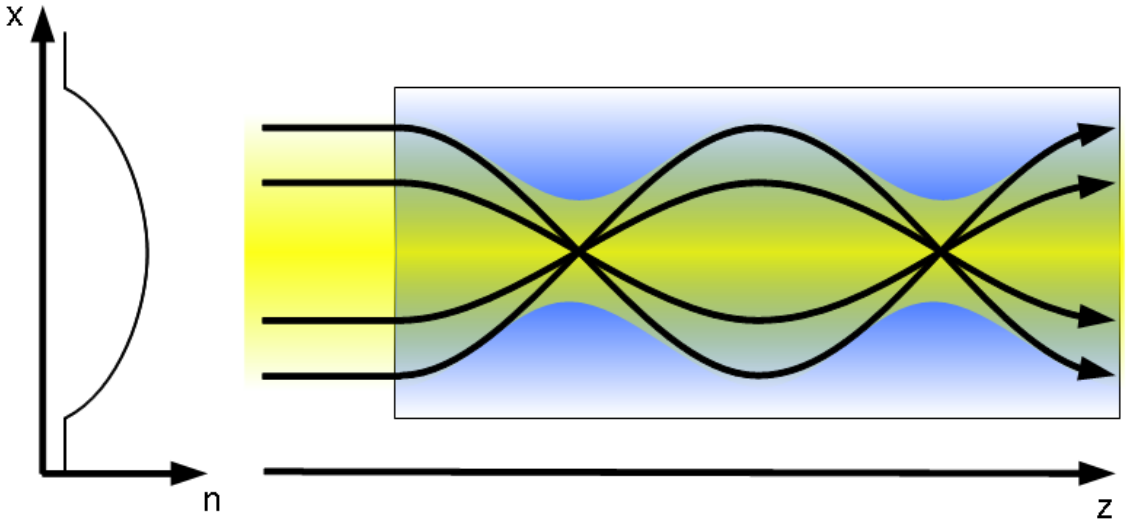

Figure 4.3: Light propagation in GRIN media with a parabolic refractive index profile (left). Light beams that are incident parallel to the optical axis follow a sinusoidal path. For lenses in the paraxial domain, this causes the field to be focused and defocused periodically.

distribution can be written as a function of the lens parameters [85]:

$$n(r) = n_{max} - \frac{r^2}{2fd} \tag{4.10}$$

where d is the thickness of the lens and f the focal length.

The propagation of light in very long GRIN rod lenses shows interesting behaviour. Owing to the parabolic index profile of the rod lens, a collimated beam incident upon the lens is focused and defocused periodically inside the GRIN lens as shown in figure 4.3. The light rays describe a sinusoidal path with a period that only depends on the refractive index profile.

Such gradient index lenses are often specified by their pitch length which is the length after which rays completed one period of the sinusoidal path. The lens in

figure 4.3 has a pitch of 1.0. The pitch length of the GRIN lens is then given as

$$p = \frac{2\pi}{a} \tag{4.11}$$

and the expected working distance f of a gradient index lens is calculated by [93]

$$f = (n_0 a \tan(aL))^{-1}, \tag{4.12}$$

where L is the length of the lens , n_0 is the refractive index at the centre of the lens and a is the parameter as defined in (4.9).

The error of the focal length is calculated with

$$\Delta f = \left[\left(\frac{1}{n_0^2 a \tan(aL)} \right)^2 (\Delta n_0)^2 + \left(\frac{1}{\tan(aL) n_0 a^2} + \frac{L}{\sin^2(aL) n_0 a} \right)^2 (\Delta a)^2 \right]^{1/2} \tag{4.13}$$

and

$$\Delta a = \left[\frac{n_R}{2R^2 n_0^4 (1 - \frac{n_R}{n_0})} (\Delta n_0^2) + \frac{1}{2n_0^2 R^2 (1 - \frac{n_R}{n_0})} (\Delta n_R)^2 \right]^{1/2}, \tag{4.14}$$

where n_R is the refractive index of the lens at $r = R$.

In elliptical lenses, the refractive index profile is described by two parabolas for the two main axes. The equation for a spherical gradient index lens [85] can be generalised to an elliptical equation:

$$n(x, y) = n_{max}(1 - \frac{(ax)^2}{2} - \frac{(by)^2}{2}). \tag{4.15}$$

These gradient index lenses have differing pitch lengths for the x and y axis which are calculated with $p_x = 2\pi a^{-1}$ and $p_y = 2\pi b^{-1}$.

Elliptical microlenses are particularly interesting for the collimation of edge emitting lasers. Due to the rectangular light emitting area, these lasers create an elliptical beam with a different divergence along the two main axes. Focusing an elliptical beam with a standard lens results in a self imaging effect where the focus is not circular but elongated dependent on the surface area of the laser diode. Traditional ways of solving this problem are the use of two cylindrical lenses to collimate one axis at a time or elliptically shaped microlenses. Two cylindrical lenses, however, are very difficult to align properly and most fabrication technologies for elliptical lenses such as ion beam writing are not suitable for mass production. An elliptical GRIN lens, which has NAs that match the characteristics of a laser diode, has the big advantage of a flat surface which makes it particularly easy to attach and align. These lenses can be fabricated in high volume, using the fabrication technology described in the following section.

4.2 Fabrication of NSGRIN lenses

In this section, the new fabrication technology for nanostructured gradient index elements is introduced. This method is very closely related to the fabrication of photonic crystal fibres which have been around for over ten years. Optical fibres are most commonly fabricated by scaling down a macroscopic glass rod to a diameter of a few tens of µm which is done with a fibre draw tower. The fabrication of photonic crystal fibres by stacking rods and tubes to a pattern, where the hollow tubes will create the necessary air holes for the photonic crystal structure, [94] has been developed rapidly in the past decade. These stacked preforms are often assembled inside a tube and then drawn to a diameter of a few hundred micrometres so that the holes have a diameter similar to the wavelength. Other techniques are, decreasing the hole sizes so that the structure has properties of an effective medium with a lower refractive index which causes guiding by total internal reflection.

All solid micro-structured optical fibres were fabricated for the first time in 2003 [95]. Instead of using rods and tubes, the structure is assembled from solid rod of two different types of glass. The used glasses are usually silica based and achieve the index contrast by different doping agents. This method can potentially increase the design freedom, the refractive index contrast can be tailored by adjusting the doping level and it also reduces inner stress and deformation compared to holey elements. The drawback of this approach is however, that the refractive index contrast and thus the photonic bandgaps are smaller. This poses no problem for the nanostructured devices introduced here because high refractive index contrasts are not necessary to fabricate a nanostructured GRIN element.

An important restriction to the choice of glasses is that they have to be thermally matched. This means, that both glasses need to have the same viscosity at the same working temperature. Glass is an amorphous solid and has therefore no defined melting point. While heating, the viscosity of the glass decreases by a certain characteristics which is unique for each glass composition. Two glasses can only be combined in the stack-and-draw method, if the viscosity curves intercept each other near their working temperature. A second restriction is the thermal expansion coefficient. The glasses need to have very similar thermal expansion characteristics, otherwise internal stress will be induced during the cooling which could cause deformation or even damage to the structure. Only very few combinations have been reported to be compatible for all solid PCFs [95–97]. A combination with a relatively high refractive index contrast could be found which has already been applied successfully for the fabrication of a spherical microlens which is covered in more detail in chapter 6.1. The two types of glass used in this case are F2, a commercial glass available from Schott AG, and NC21, a silica based glass fabricated in the Institute of Technical Materials and Electricity (ITME) at Warsaw University. A second pair of glasses was used for

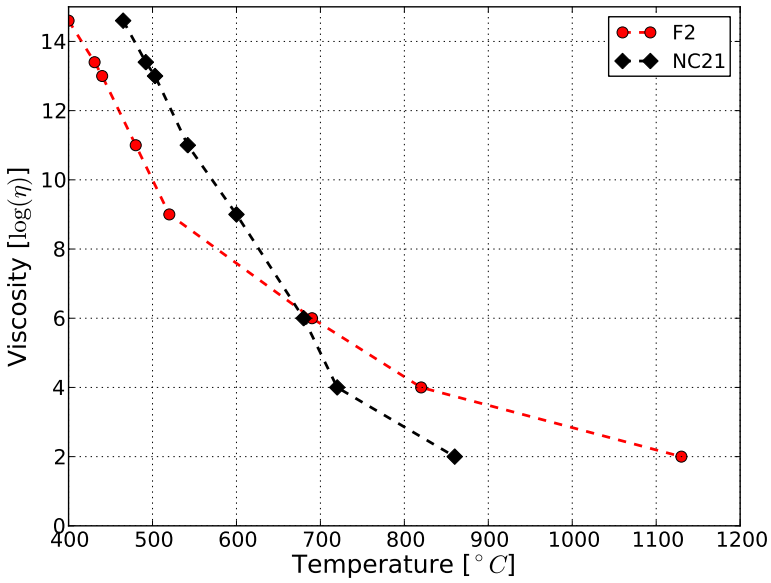

Figure 4.4: The viscosity curves of F2 (black) and NC21 (red). The combined structures can only be drawn if the viscosity of the two glass types is very similar. During the drawing process a furnace temperature around 670°C is chosen.

the fabrication of an elliptical microlens (chapter 6.2). In this case NC21 and NC25 were combined in the pattern of the preform. Both glasses were fabricated at ITME. Details and parameters of the NC glasses can be found in the publication by Lorenc et al. [97].

Figure 4.4 shows the viscosity characteristics of F2 and NC21 as a function of the temperature which intercept at $T \approx 670°C$. The viscosity at this temperature is high enough for the glasses to be drawn together. Similar graphs can be compiled for other possible glass pairs.

The main differences in the fabrication of NSGRIN lenses compared to PCFs are the number of rods, that are used for the creation of the pattern, and the final diameter of the structure. For PCFs typically a few tens of rods are used, whereas for NSGRIN elements up to several thousand rods can be needed to form a required pattern. Furthermore, these elements are not used as guiding structures such as fibres and waveguides but as very thin phase modulators. Rather than drawing photonic crystal fibres with feature size typically in the order of 1 µm non-guiding structures with a much larger diameter and feature sizes of 200 nm and less are fabricated. These structures are cut to discs of a few hundred µm thickness for use as optical GRIN elements like lenses and beam correctors.

The fabrication process consists of several intermediate steps. It starts with the assembly of the preform which is then scaled down with the fibre draw tower to a diameter of 2-3 mm. In the first assembly the refractive index distribution of the single elements are determined which cannot be changed later on apart from the diameter. From this rod a new intermediate preform is assembled which is again drawn with

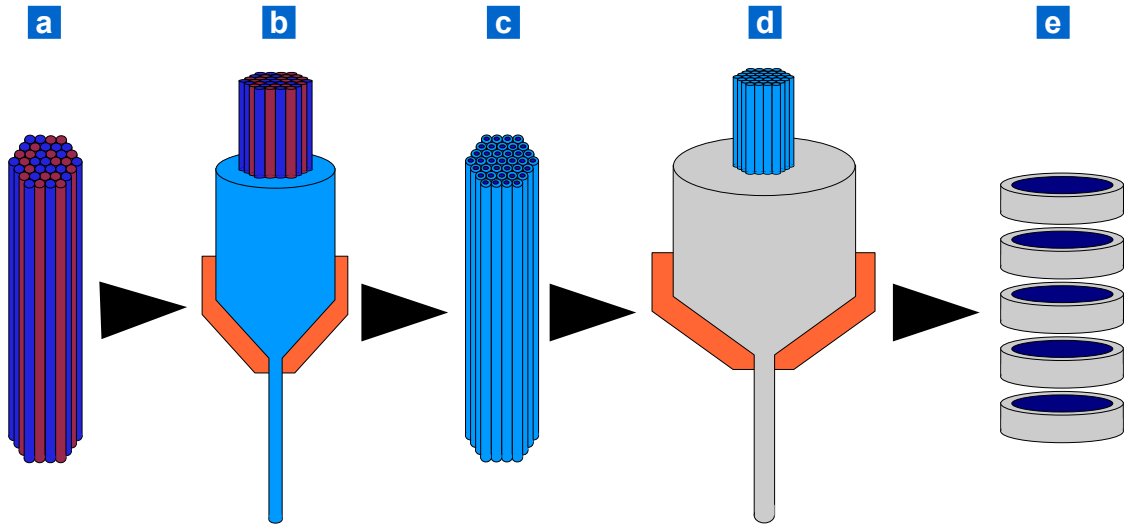

Figure 4.5: The fabrication of NSGRIN lenses which consists of at least 5 steps: The assembly of the preform (a), the first down scaling with the fibre draw tower (b), assembly of an intermediate preform (c), second down scaling step (d), and dicing and polishing to the correct thickness (e). Steps (c) and (d) can be repeated several times.

the fibre draw tower to reduce the size of the lens even further. If required the rods of the intermediate preform can be arranged to an array. This step can be repeated until the correct lens diameter has been achieved. In the final step the obtained rod is diced to thin disks which are then polished to the required thickness and smoothness.

4.2.1 Assembly of the Preform

The fabrication of a nano structured optical element starts with the assembly of a macroscopic glass preform with the same structure as it is required in the final optical element, although much larger in scale. These patterns can consist of a few hundreds up to a few thousand glass rods with final diameter of $\lambda/5$ or smaller for designs in the effective medium domain (Fig. 4.5a). The largest preform that has been fabricated so far is an elliptical microlens in a hexagonal preform consisting of 100 rods in diameter. The assembly of the preform is a very critical and labour intensive task. In this first step, the pattern which will form the nanostructured GRIN element is assembled from two types of rods with a diameter of 0.8 mm-1.0 mm. The scaled down preform will have to be stacked again in an intermediate preform, the best shape of the preform is therefore a regular hexagon or a square. Rods with these shapes can, unlike circular rods, be stacked into an array without leaving air gaps. This is important because any gaps would cause the structure to deform in the next drawing step.

The preform is assembled with the help of a stacking holder (Fig. 4.6a) which keeps the rods in place before they are fused together by melting the preform on one end

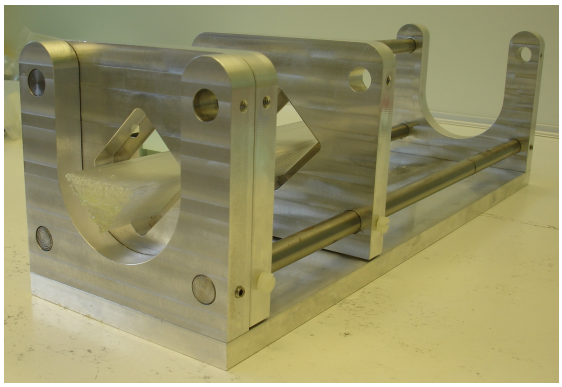

(a) The device in which the preform is stacked. In this case the rods are kept in place in a square shaped frame.

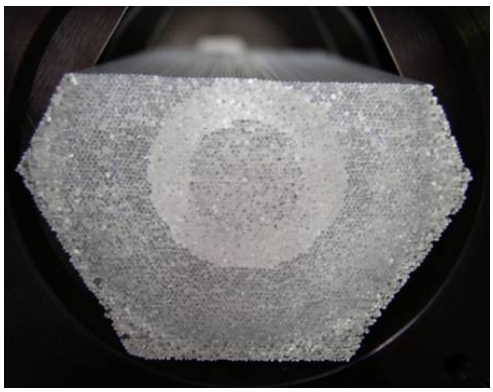

(b) Front view of a preform that is stacked line by line in a hexagonal holder

Figure 4.6: The preforms have to be stacked by hand with the help of a preform holder which can have different shapes

or by using some adhesive. Figure 4.6b shows the front view of a preform for a nanostructured GRIN lens. This hexagonal preform was stacked layer by layer up to about three quarters of the total height. Each rod is placed individually according to a certain pattern. The design algorithms to find the required pattern will be explained in detail in the next section. The stacking of the first preform is usually performed by hand. At a later stage it is planned to use a robot to do this standard pick-and-place routine [98].

At present, only two different types of glass are included in the structures, although the use of further materials is possible, in order to create multi level elements. Another option to get rods with a variety of refractive index values is to create intermediate rods in an earlier drawing process. These rods are assembled from from two different types of glass rods. By varying the density ratio of the two materials it is possible to fabricate meta-rods which have a constant effective index that can take any value between the indices of the two glasses. These so fabricated rods have all the same physical properties if the two mixed glasses are compatible to each other.

4.2.2 Drawing of the Preform

In the next step (Fig. 4.5b), the preform is processed to generate an intermediate preform of about 2 mm diameter by using the fibre draw tower shown in figure 4.7. A fibre draw tower consists of several components which can differ in size and complexity dependent on the requirements. The underlying principle is however always the same. The preform is mounted in a preform holder, which can be moved up and down by a motor. When the preform is inside the furnace, it is heated up in a small area to temperatures higher than the softening point. Due to the lower viscosity in this area, the glass drops down which causes the diameter of the structure to shrink. If the

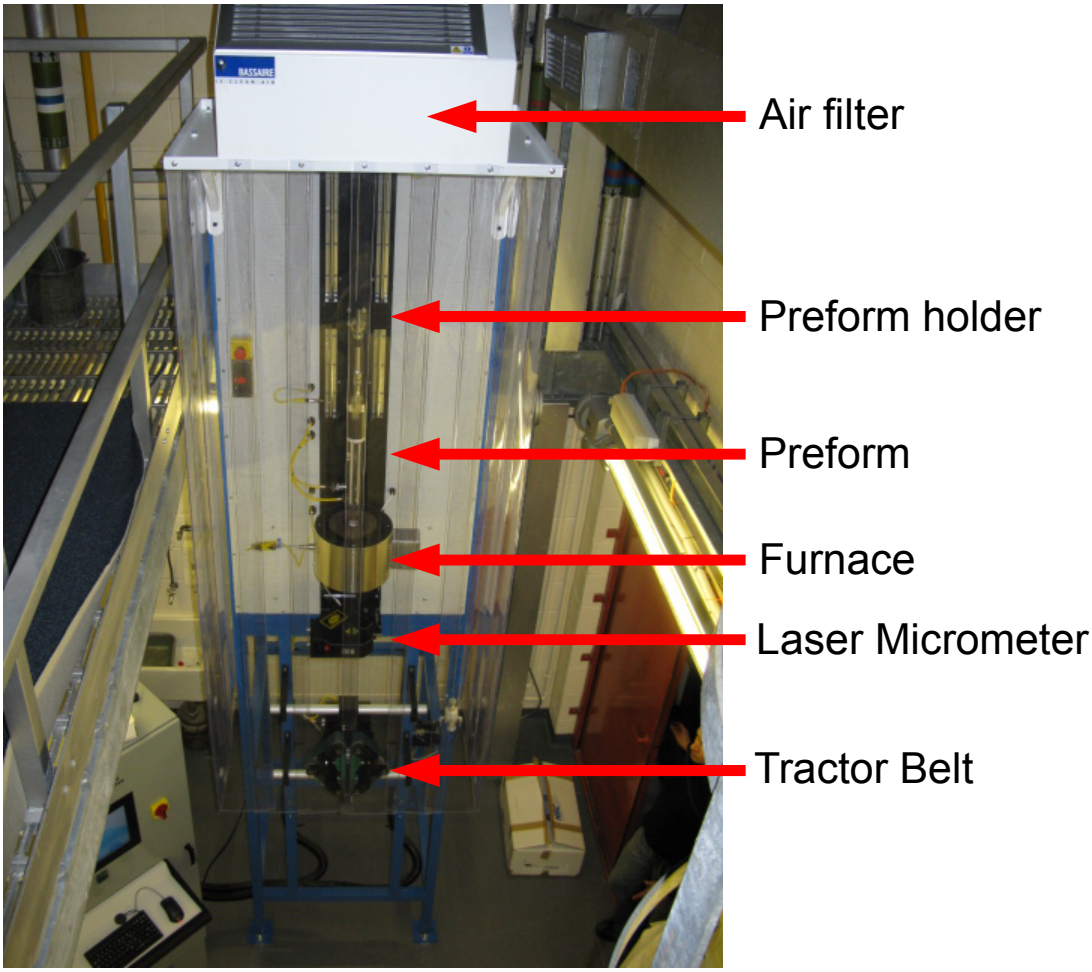

Figure 4.7: Photo of the fibre draw tower at Heriot-Watt University. The air filter creates a small overpressure inside the PVC curtain to prevent dust to enter the system. The preform holder with which the preform is lowered into the furnace is driven by a stepping motor. Inside the furnace, the temperature is monitored with a temperature sensor. The fibres or thin rods are pulled down by the tractor belts by a certain rate. The diameter of the scaled down structure is monitored by a laser micrometer.

temperature is not too high, the internal structure will remain the same and only the dimensions of each feature are scaled down. The thinner rod below the furnace is pulled down with the tractor belts at a constant speed. The diameter of the resulting rod can be controlled by varying the feed speed of the preform or the draw speed of the tractor belts. From the diameter of the preform and the target diameter of the downscaled structure the feed speed to draw speed ratio can be calculated:

$$\frac{v_{draw}}{v_{feed}} = \frac{d^2_{preform}}{d^2_{final}} \quad . \tag{4.16}$$

Equation 4.16 is derived from the fact that the same volume per time has to be fed from the top as is drawn out of the furnace. A very high draw speed requires higher temperatures in the furnace in order to melt the glass quickly enough. A too high

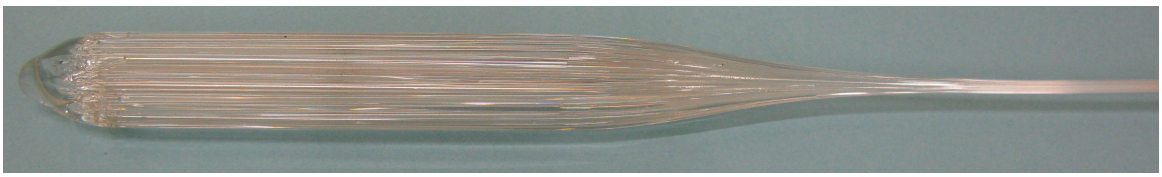

Figure 4.8: The preform after drawing as much as possible. Around 10-15 cm are lost because the preform holder cannot be lowered into the furnace. The area where the glass is molten and extruded is nicely visible as the cone shaped part between the large and the small diameter

temperature, however, causes the structure to distort, therefore there is an upper limit of the draw and feed speed. For structured preforms, the temperature inside the furnace should be chosen as low as possible, because the internal structure becomes more stable and viscose with decreasing temperatures.

During the draw process, the furnace temperature and the new diameter are constantly measured by a thermometer and a laser micrometer, respectively. These parameters can be used in a PID feedback loop [99], which is controlled by a computer and adjusts the draw and feed speed dynamically to give optimum results. It was however found that for drawing such large diameter rods, manual control of the parameters is superior to using PID controls.

Figure 4.8 shows a piece of a test preform which has been drawn in the fibre draw tower at Heriot-Watt University. The preform is assembled from Pyrex rods only, to investigate the influence of temperature and draw speed on the result. On the very left hand side the rods are fused together by melting them. Another often used method is to fix the structure with a heat resistant adhesive. This should only be applied at the upper end which won't be molten in order to prevent contamination of the glass structure. In the middle of the structure is the area where the preform is scaled down inside the furnace. In order to achieve the least possible distortion the conical transition area, where the preform is scaled down, should be as long as possible. The resulting rods with a final diameter of typically between one and three millimetres are cut to a length of around 30-50 cm. If the length of the preform is too short, so that most of the structure would go to waste it is possible to place it in a longer tube in order to scale down the whole preform.

4.2.3 Assembly and Drawing of the Intermediate Preform

One drawing step generally does not achieve enough demagnification to get an effective medium structure. Therefore the intermediate rods obtained in the previous step have to be stacked and drawn again to get the required feature sizes (Fig. 4.5c). If a microlens array with very high fill factor is to be fabricated, the new preform is stacked only from the hexagonal structured rods from the previous drawing step. If a single lens or an array with a certain distance between the lenses is required, the

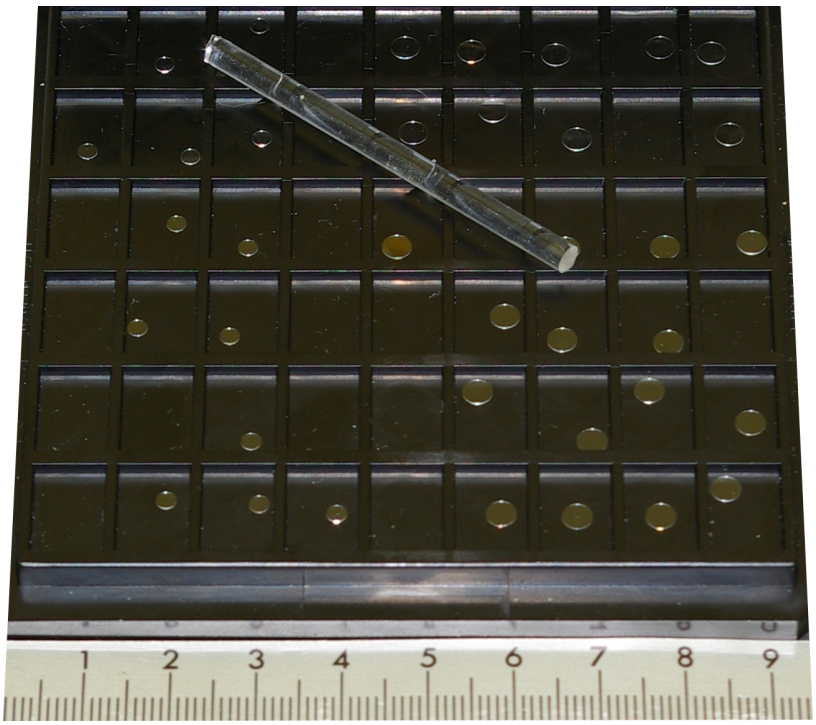

Figure 4.9: The final product of the stack-and-draw process. The short rod contains the NSGRIN structure through the whole length. The diced and polished lenses are placed in the individual sections of the box. The final structure has been drawn to various diameters, on the left hand side some smaller structures and on the right hand side lenses with a larger diameter

spacing is filled with glass rods of one of the two components. In the case of lenses, the filling rods are generally chosen to be the lower index glass, in order to avoid an index step at the edge of the lens structure. One dimensional or two dimensional microlens arrays could be used for example for the collimation of diode laser arrays or to couple light into multiple waveguides.

This new intermediate preform is again scaled down with the fibre draw tower in the same manner as the original preform (Fig. 4.5d). If a twofold downscaling still does not give small enough features and lens diameter, this fabrication step can be repeated by creating another preform from the obtained rods.

For microscopic pictures of this fabrication step please refer to figures 6.1, 6.5 and 6.9 in chapter 6 where a spherical and an elliptical microlens are characterised theoretically and experimentally.

4.2.4 Dicing and Polishing of the Finished Elements

After the final drawing step, the NSGRIN structures have the required diameter and distance between the elements. The structure extends through the whole length of the rod. Depending on the length of the intermediate preform, several metres of the GRIN structure can be obtained. If the drawing takes place in a well controlled environment

and with constant fabrication parameters, the cross sections at any point in the rod are identical. The required thickness of the NSGRIN lenses can be calculated from equation 4.12 and is typically in the order of a few hundred micrometres.

The possible feature sizes of elements fabricated with this method range from an upper end of a few micrometers down to nanometres, although for features sizes below 10 nm, diffusion effects would be expected to soften the transitions between areas with different refractive indices. This effect does not pose a problem for NSGRIN elements because the effective refractive index distribution does not change if materials are mixed as is calculated by averaging the refractive index over the neighbourhood of each point.

The rods resulting from the final drawing step are then cut to discs of around 500 µm thickness using a circular glass saw (Fig. 4.5e). Each cut causes a material loss of 400 µm due to the thickness of the blade. The obtained disks are then polished in bulk on one side by using grinding disks of various roughness to achieve a 1 µm polish. On the other side, the lenses are then polished down to the required thickness of typically around 100-200 µm. With this approach, the yield of a one metre rod are 1000 identical microlenses. This ratio could be improved by using a thinner blade and by cutting the discs to a thickness only slightly more than the final lens.

4.3 Design of Nanostructured Gradient Index Elements

This section covers the algorithm to design nanostructured gradient index elements for the fibre draw method described above. By using the effective medium theory, it is possible to design optical elements with a discrete pixelated refractive index profile on a length scale of $\lambda/5$ or smaller, with the characteristic of a gradient index material on a macroscopic scale. This approach gives a great design freedom because it is not restricted by limitations of the traditional fabrication methods of GRIN materials. Firstly, the simulated annealing algorithm is introduced which is then applied to design effective index structures.

4.3.1 The Simulated Annealing Algorithm

The simulated annealing algorithm was introduced independently by Kirkpatrick and Cerny in the 1980s [100, 101]. It is a probabilistic algorithm to search for the global maximum or minimum of a function, determined by a large set of parameters. The term 'annealing' comes from metallurgy where, in order to minimise the number of defects in the crystal structure, metals are treated with controlled heating and cooling. When heated, some atoms that might be in a defect state can get enough thermal

energy to swap into an energetically better lattice position.

In numerics, a system is considered, that can be described by a very large set of parameters which can not be treated analytically. The aim of the simulated annealing algorithm is to find the parameter combination that gives a global minimum of the defined function. In a system with several thousand parameters it would take extremely long to try all possible combinations to find the best solution.

The simulated annealing algorithm is an iterative algorithm which uses a directed search to find the minimum of such problems. It belongs to the family of Monte Carlo Methods [102]. The difference to completely random algorithms is that in each iteration step the current solution is replaced by a nearby solution by changing one parameter. After the changes, the new configuration is compared to the previous one. The new configuration is accepted or declined by a certain schedule defined later in this section. To measure the performance of a parameter set, a function has to be defined which compares the result of the current configuration with the desired yield. This function C is called the cost function or merit function. In metallurgy the cost function would be the inner energy as a function of the position of all atoms in the metal. The cost function for mathematical problems is often defined as the difference of the desired yield to the current result.

Figure 4.10 shows an example of how the dependency of the cost function to one parameter might look like. The real cost function is very high dimensional which cannot be displayed graphically. Even in this very simplified sketch it is obvious that the algorithm would be very likely to be trapped in one of the local minima if only changes are accepted that decrease the cost function. The blue spot in the diagram represents one possible parameter configuration. As in each iteration step the state is changed to a neighbouring state, a few changes that decrease the performance have to be accepted in order to overcome 'potential wells' that lie between the local and the global minimum.

This is where the annealing comes in. Analogue to the thermal energy in metals, which gives the atoms some flexibility in their movements, a numerical schedule is defined, that allows bad changes to be accepted with a certain probability. A virtual temperature constant is introduced which decreases to zero over the iteration process. The decision, if a change of the parameters is accepted, is determined by the following equation:

$$\text{choose } p = \text{rand} \in [0,1] \Rightarrow \begin{cases} \text{accept, if} & \exp\{-\Delta C/T\} > p \\ \text{decline, if} & \exp\{-\Delta C/T\} \leq p \end{cases} . \tag{4.17}$$

Equation 4.17 implies that changes that improve the performance are always accepted because ΔC will be negative and p is smaller or equal to 1. In the early stage of the iteration, where T is high, most changes are accepted. After each step the

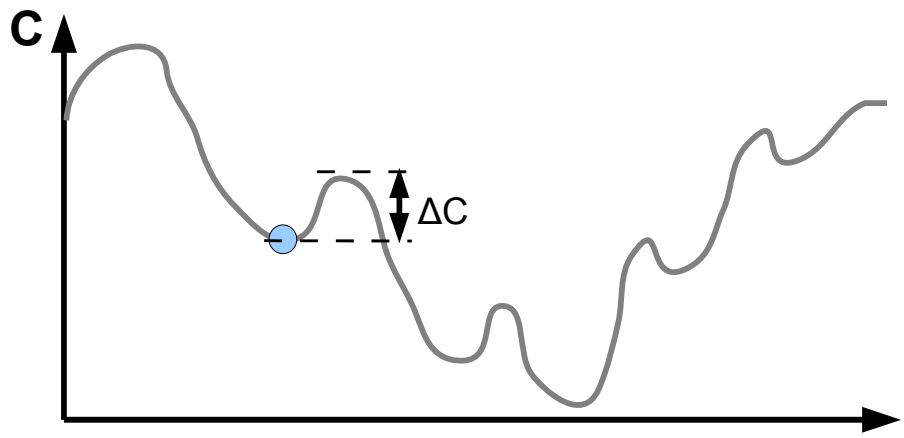

Figure 4.10: An example of a cost function. This diagram displays only a dependency of one parameter. Usually the cost function depends on several hundreds or even thousands of parameters. The blue circle represents one possible state. To get to the global minimum, a few changes which increase the cost function have to be accepted to overcome the potential hill.

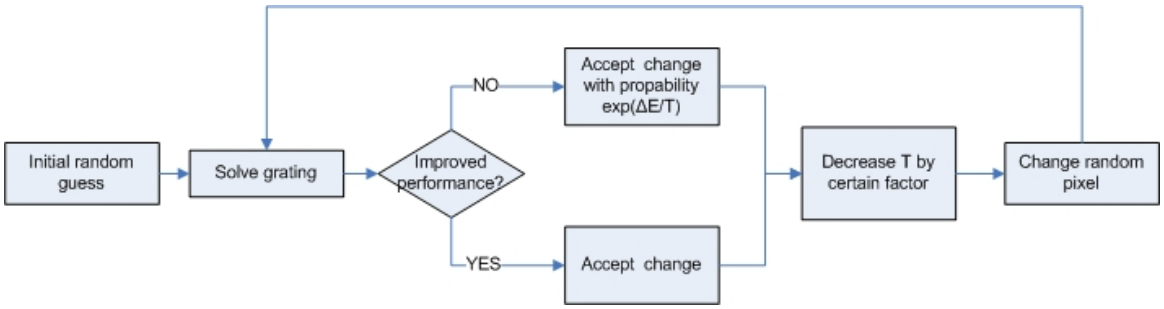

Figure 4.11: Flowchart of the simulated annealing algorithm.

T constant is decreased slightly. The smaller T becomes, the fewer bad changes are accepted which can be interpreted by a rough search in the beginning and a fine tuning of the result in the end of the algorithm. This scheme increases the probability in most cases, that the global minimum of the cost function is found. T is usually decreased exponentially, but the schedule has to be adjusted for each problem individually. Figure 4.11 shows a flow chart of the basic simulated annealing algorithm. The iteration is either repeated for a fixed number of cycles or until a certain value of the cost function is reached.

There are many variants and optimisations to this basic algorithm. A good overview can be found in the book by Salomon et al. [102]. One variant that is used later, is the direct binary search. In the direct binary search, the T parameter is set to zero from the first iteration step. Therefore, only changes that improve the performance are accepted. This method can be much faster for problems where the cost function has a relatively smooth profile and there are no local minima. It can lead to a very fast convergence of the algorithm when designing NSGRIN lenses.

4.3.2 Design of NSGRIN lenses

The simulated annealing algorithm is the ideal method to design nanostructured GRIN lenses, fabricated with the method described in section 4.2. The refractive index of each single rod is a free parameter that affects the effective refractive index profile. To design such structures, an array is defined where each element contains the refractive index of one rod. The effective index profile is obtained by calculating the effective index for each point in the array.

Before starting the design algorithm, the desired index distribution is defined depending on the application. The refractive index can take any value between the two refractive indices n_1 and n_2 ($n_1 < n_2$). In contrast to conventional GRIN elements, there are no constraints on the refractive index profile. The distribution can be asymmetric and also non-monotonous because the fabrication does not depend on diffusion. The cost function is defined as the standard deviation of the effective index distribution calculated with equation 4.7:

$$C = \frac{1}{P}\left(\sum_{p=1}^{P}(n_{eff}(p) - n(p))^2\right)^{1/2} \quad . \tag{4.18}$$

$n_{eff}(p) = \sqrt{\epsilon_{eff}}$ is the effective index at point p, $n(p)$ is the desired index value and P is the total number of pixels in the structure.

In each iteration step, the refractive index of one random pixel is changed and the value of the cost function is compared to the previous one. With the right cooling factor and radius for the neighbourhood, the effective index distribution will take a shape very similar to the desired profile. The averaging radius needs to be large enough to contain enough pixels, in order to get a smooth scale but small enough to only use parts of the grating that effect the effective index at this point.

The convergence of the simulated annealing algorithm depends strongly on the cooling schedule and the initial guess for the material distribution. Three different methods to get the initial pattern are investigated:

1. The design starts with all pixels assigned to the same refractive index of one of the possible indices

2. The design starts with a random distribution of all possible indices

3. The design starts with a distribution of the possible indices by assigning each pixel with a certain probability to one of the materials. The probability to assign the higher refractive index is

$$p = \frac{n(r) - n_1}{n_2 - n_1} \quad . \tag{4.19}$$

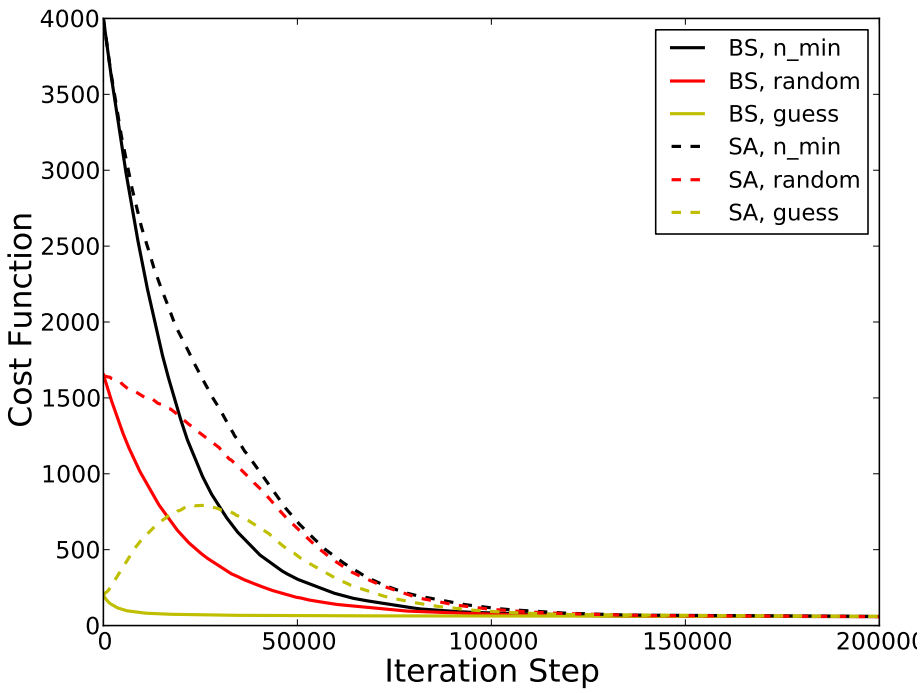

Figure 4.12: The convergence of the design algorithm for different starting points using simulated annealing (SA) and direct binary search (BS). The simulated annealing was performed with $T_{start} = 1.5$ and and exponential cooling schedule applied every 500 steps ($c_{cool} = 0.97$). The initialisation method was to set all pixels to the lower index value (black), set each pixel randomly to one of the two values (red) and to assign the value of each pixel with the probabilistic method (yellow)

Figure 4.12 shows the convergence of the simulated annealing (SA) and the direct binary search (BS) in combination with all three methods for the initial index distribution. The comparison of the convergence of the cost function for simulated annealing and direct binary search with different starting configurations shows, that the algorithm converges in any case to the same value which seems to be a characteristic value for this system. Direct binary search in combination with a best guess initial distribution is the best and quickest choice in this case as there is no danger of getting stuck in a local minimum of the cost function.

Figure 4.13 shows the result of an example of the design algorithm. The target index profile, as shown in figure 4.13e, is calculated by $n(x, y) = 1.6 + 0.1 \sin(x) \sin(y)$. The structure consists of 200×200 pixels where each pixel can take one of the two possible indices $n_1 = 1.5$ and $n_2 = 1.7$. The effective index is calculated by averaging over a circular area around each pixel with a radius of 8 pixels. At the edges of the structure, only pixels inside the array are included in the effective index calculations, no assumption is made on the surrounding. Figure 4.13c shows the effective index profile of the initial guess (Fig. 4.13a) obtained with the best guess method as described above. The initial guess is already very similar to the target and the final structure (Fig. 4.13b) has an effective index profile that is nearly indistinguishable

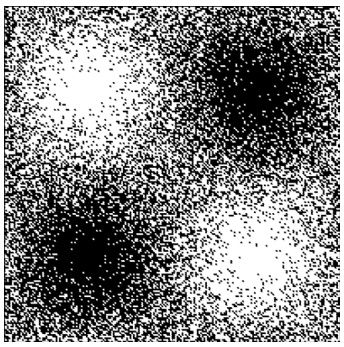

(a) Initial pattern for the design algorithm, obtained with the probabilistic approach

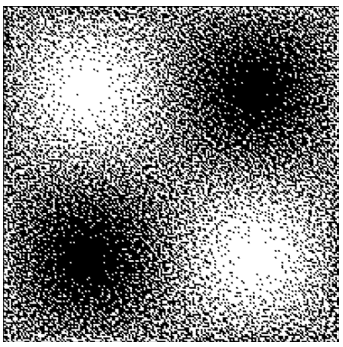

(b) Final result of the design algorithm

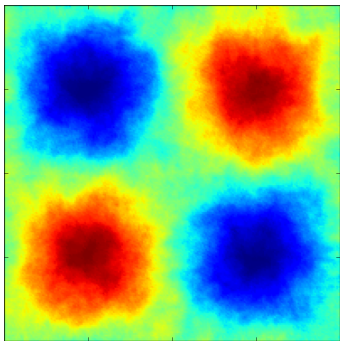

(c) Effective index profile of the initial pattern

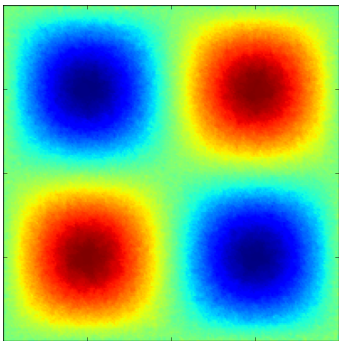

(d) Effective index profile of the final pattern

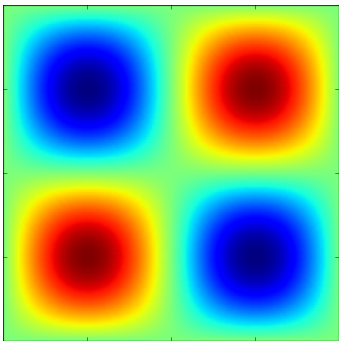

(e) Target profile of the refractive index

Figure 4.13: Start pattern (a) and final index distribution (b) of the simulated annealing algorithm. Using the best guess method already gives a pattern with an index distribution (c) very close to the target (e). The final refractive index profile (d) is nearly identical to the target.

from the target (Fig. 4.13d).

4.4 Design of non periodic multilayer lamellar phase gratings

Cylindrical lenses have the property to focus light along one axis only. Their main applications lie in the collimation of diode lasers [103, 104]. Various other applications include light coupling into planar waveguides [105], wavefront sensing [106] and stereoscopic displays [107]. Cylindrical microlenses are mostly fabricated by lithographic methods, moulding [107], direct laser writing [108] or with the sol-gel reflow technique [84].

In this section it is shown how the stack-and-draw technology can be used to fabricate cylindrical microlenses. Secondly, an algorithm, based on the Fourier modal

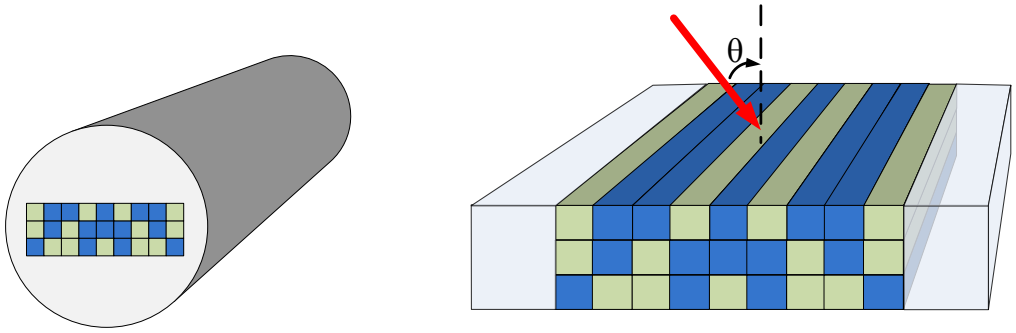

(a) (b)

Figure 4.14: Schematic view of the micro structured lamellar grating. After the drawing process the structure is completely embedded in the cladding (a) which is then removed from two sides to uncover the lamellar structure (b).

method to analyse non-periodic gratings subwavelength feature sizes, is introduced. Unlike gratings with feature sizes larger than the wavelength, which can be analysed with Fourier optics or the beam propagation method, gratings with features smaller than the wavelengths have to be solved rigorously. Such elements cannot be reverse engineered, the only way to find a structure with the desired properties is by iterative methods like simulated annealing or the generic algorithm [109]. To design the material distribution, the Fourier modal method is used in conjunction with a simulated annealing algorithm. Depending on the complexity of the problem, the iteration needs to be repeated up to several thousand times to get good results. Therefore it is crucial to evaluate the performance of a configuration as fast as possible in order to minimise the computation time for each iteration step.

For the design of a cylindrical microlens the simulated annealing algorithm is applied to optimise the electromagnetic field in the desired focal plane. In order to get the steady state field at some distance z behind the grating the FDTD method is not very fast, because the simulation has to be run long enough to overcome the transient oscillations. It is much faster to analyse such grating structures with the Fourier modal method. The FMM is based on discrete Fourier expansions which are periodic with a period equal to the size of the analysed grating. Due to this periodic nature of the FMM, the transmitted field represents the yield of an infinite array of the investigated structure which can be substantially different from a single isolated element. The transmitted field of each element interferes with its neighbours, creating a characteristic interference pattern.

To solve this problem, Hugonin and Lalanne introduced a perfectly matched layer to the computational cell of the FMM which breaks the periodic symmetry [110]. This involves a complex nonlinear coordinate transform to simulate an infinite layer with gradually increasing absorption. Using this method would require substantial changes in the FMM implementation because all equations need to be transformed to

this new coordinate system.

A different approach is, to include the surrounding area of the lens and embed the non periodic grating into an area of the substrate material which can be absorbing or transparent. The increase of the computational space would diminish the interference. This however increases the computational cost because many more Fourier orders are needed to achieve the same spatial resolution compared to solving the grating alone.

In this chapter an alternative method is introduced for which the computational space is increased only for the transmitted light and the grating is solved with the standard FMM. This method is used in conjunction with the simulated annealing algorithm to design a diffraction limited cylindrical lens.

The introduced structures are intended to be fabricated with the earlier introduced stack-and-draw technique. In contrast to the spherical microlenses, the structures here will be illuminated perpendicular to the rods, giving a very long lamellar structure which can consist of only a few and up to a hundred layers. The preform is assembled in a rectangular format which is then scaled down to the appropriate size using the fibre draw tower. The obtained rod is polished from the sides to lay open the structure along the front and back surface of the grating. A schematic sketch of such a lamellar element is displayed in figure 4.14. The element is embedded in a cylindrical or hexagonal preform and can be used after removing the excess material that covers the structure. Depending on the fabrication steps these gratings can be assembled as arrays or as single isolated elements.

To give experimental evidence of the analysis method, a cylindrical diffraction limited lens is designed and characterised in the microwave regime.

4.4.1 Use of the field stitching method to calculate the external field of non periodic gratings

The FMM is based on a discrete Fourier transform of the grating structure and the electromagnetic field. It is therefore well suited for periodic gratings and diffractive optical elements but cannot be used directly for the calculation of the far field of non-periodic structures. The transmitted field has the same periodicity as the grating if the standard implementation of the FMM is used. This can lead to strong interferences which are induced by the periodicity of the discrete Fourier transform as shown in figure 4.15a. For thin elements, where the periodic boundary conditions do not have a strong effect on the propagation inside the structure, there is a way to avoid the effect of the periodicity on the transmitted field without having to introduce a perfectly matched layer. With the field stitching method [45, 47] it is possible to increase the period for the calculation of the transmitted light by embedding the structure in a larger area which does not emit any light. This results in a suppression of the numerically induced cross talk as displayed in figure 4.15b. The idea of this method

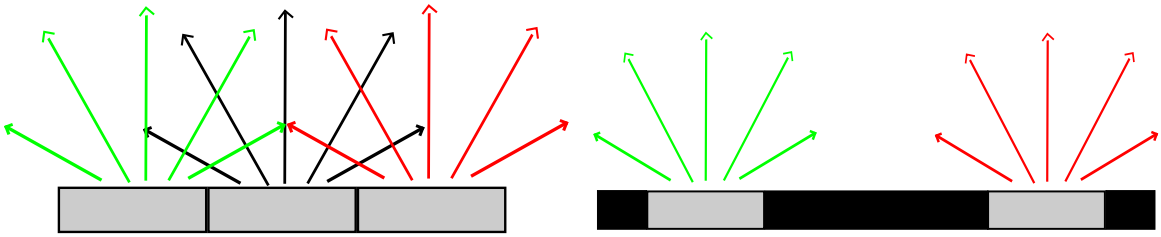

(a) Without padding (b) With padding

Figure 4.15: Sketch of the two different cases. (a): Without padding nearby neighbours interfere strongly with each other. (b): If a spacer is added into the periodicity, the cross talk can be reduced strongly (b).

is to calculate new transmission coefficients by assuming that the region outside the grating completely absorbs all light and all transmission coefficients are zero.

The transmitted field is written as a Fourier expansion with period p in x direction and light propagating in z direction:

$$U_T(x,z) = \sum_m T_m \exp[i(\alpha_m x - t_m z)] \tag{4.20}$$

U stands for the electric field in TE polarisation and for the magnetic field in TM polarisation. T_m, α_m, t_m are obtained from the FMM where T_m are the transmission coefficients, $\alpha_m/2\pi$ and $t_m/2\pi$ are the spatial frequencies of the field in x and in z direction respectively. The field is periodic in x with the size of the analysed element.

The field stitching method was introduced to analyse large gratings with very small feature sizes by splitting the grating into several sub-regions. These regions are then solved separately and the transmission coefficients of the overall grating are calculated as a combination of all sub-regions. The new transmission coefficients T' for the spatial frequencies γ' and larger period p' can be calculated with [45]

$$T'_m = d^{-1} \sum_{n=1}^{N} \sum_{p=-P}^{P} T_p^n \exp\left[-i\gamma'_p(x_n - x_s)\right] \int_{x_n}^{x_{n+1}} \exp\left[i(\gamma'_p - \gamma_m)x\right] \mathrm{dx} \tag{4.21}$$

where x_n is the position of the nth sub area, x_s is the overlap of two adjacent areas and T_p^n are the transmission coefficients of the n^{th} sub-region.

By adding a dark area to either side of the computational space of the transmitted light it is possible to calculate the transmitted field in the non-periodic case. This arrangement can be interpreted as one large element consistent of three areas as shown in figure 4.16. The two outer parts have all transmission coefficients equal to zero and the central element can be solved with the FMM. Substituting this into equation 4.21 gives the equation for the transmission coefficients of an isolated element when the

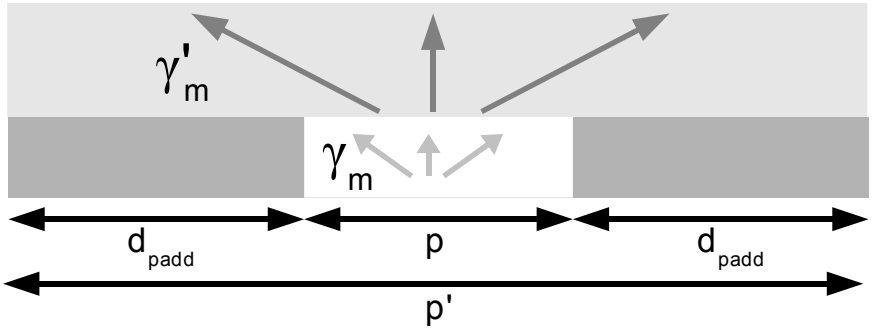

Figure 4.16: The element is embedded in an absorbing padding with dimension d_{padd} on either side. The transmission coefficients γ'_n of the new computational cell with period p' are calculated from the grating's coefficients γ_m with period p

padding size d_{padd} is sufficiently large:

$$T'_m = \frac{1}{p'} \sum_p T_p \exp\left[-i\gamma'_p d_{padd}\right] \int_{d_{padd}}^{d_{padd}+p} \exp\left[i(\gamma'_p - \gamma_m)x\right] \mathrm{dx} \quad . \tag{4.22}$$

Propagating the light with the new transmission coefficients results in a strongly reduced interference effect. The number of Fourier orders for the embedded field needs to be larger than the number of orders that was used to solve the grating and increases proportional with the padding size. To avoid losing information of the field distribution it has to be ensured that the spatial frequency of the new truncation rank is at least as high as the highest frequency used in the FMM algorithm.

The necessary padding size depends on the diffraction properties of the analysed structure and on the distance of the region of interest to the element. For example, structures that diffract the light strongly into high orders require a larger padding than focusing elements.

Figure 4.17 shows a false colour map of the field in the xz-plane of a simple lens with a parabolic refractive index profile. The diagrams show the transmitted field calculated with equation 4.22 for a padding size d_{padd} of 0, 2, 4 and 6 times the grating size, respectively. In figure 4.17a, where the standard FMM was used to calculate the transmitted field, even though the field shows some focusing, strong interference patterns are visible. In figure 4.17b, the padding on either side of the grating is twice the grating size. In this case, the near field has a distribution as would be expected from a single lens and the interference effects in the focal area are also reduced. The larger the padding area, the more the interferences can be reduced. For $d_{padd} = 4$ (Fig. 4.17c), the field is only disturbed by a very weak modulation and for $d_{padd} = 6$ (Fig. 4.17d), the field in the calculated area represents a completely isolated lens.

To show how the field distribution of the lens converges to a stable profile, the field

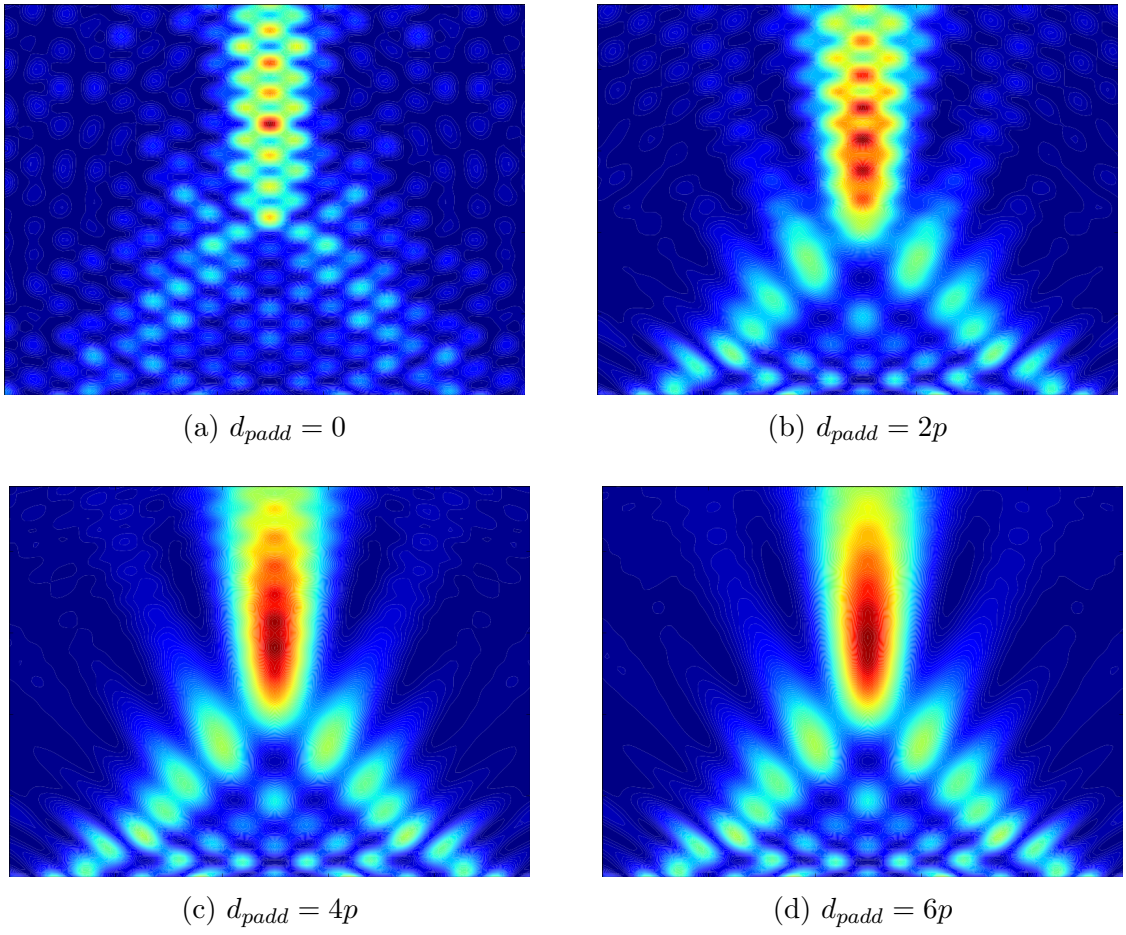

(a) $d_{padd} = 0$ (b) $d_{padd} = 2p$

(c) $d_{padd} = 4p$ (d) $d_{padd} = 6p$

Figure 4.17: (a) Transmitted field distribution for the periodic case with no added frame. The larger the padding size, the less is the influence of the periodicity. For a padding size of two times the grating size on either side, the interference pattern is still strong (b). It is only visible after the focus for a padding size four times the grating period (c) and completely suppressed a padding size of 6 times the period (d).

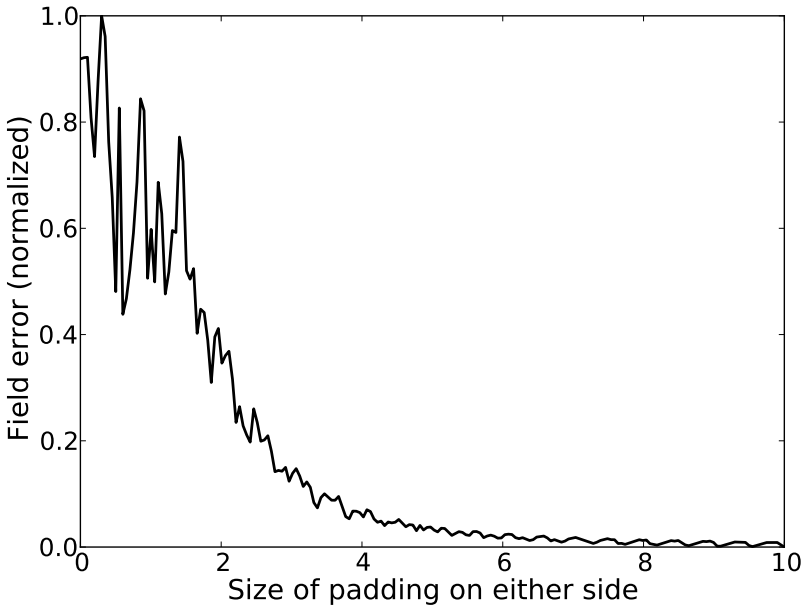

Figure 4.18: Error of the field in the focal plane as a function of the padding size

error in the focal plane is calculated as a function of d_{padd}. Figure 4.18 shows the normalised field error in the focal plane as a function of the padding size. The error is calculated as the standard deviation to the field, calculated with $d_{padd} = 10p$ on both sides of the structure:

$$\sigma_D = \left[\sum_{a=1}^{P} (F_a^{(D)} - F_a^{(10)})^2 \right]^{1/2} \tag{4.23}$$

where $F_a^{(D)}$ is the field with $d_{padd} = D \cdot p$ at point a in the focal plane. The field was calculated at 200 points in the focal plane and the step size for the padding is 0.1 times the lens period. For very small padding sizes, the error fluctuates strongly but decreases very fast to zero for $d_{padd} \geq 2$. These characteristics are obviously only valid for this particular lens, the convergence for other structures might be much slower or faster. The computational cost of increasing the padding is small compared to the analysis of the grating, so choosing a higher value for d_{padd} has only a small influence on the performance of the algorithm.

Even for focusing structures like the lens considered here, the periodic boundary conditions introduce a non negligible error. For the analysis of non-periodic elements it is therefore essential to consider this effect in order to get correct results in the external field distribution. The advantage of using the field stitching method is that it can be used with any method that uses Fourier factorization of the electromagnetic field, such as the Method of Moments [111] or the C-Method [10], without having to apply changes to the analysis of the element.

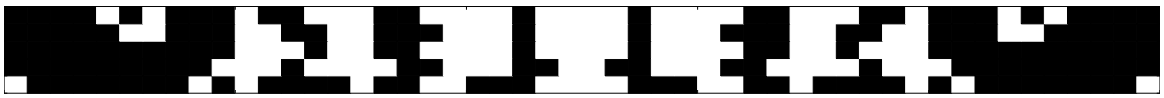

Figure 4.19: Structure of the microwave lens which was designed with the simulated annealing algorithm. The white parts represent perspex, black is air.

4.4.2 Design of a cylindrical lens using simulated annealing

The design of these lamellar structures is performed with the simulated annealing algorithm described in section 4.3.1. Due to the necessity of analysing the structures rigorously, an inverse design approach, as it is used in the scalar domain, is not available. The cost function gives an indication of the quality of the focusing effect by calculating how well the field in the focal plane matches the desired result.

For a cylindrical lens design the cost function is defined by

$$C = \alpha \cdot \left[\frac{\int_0^p I(x,f)dx - \int_{x \in F} I(x,f)dx}{\int_0^p I(x,f)dx} \right]^{\beta} + \gamma \cdot R \tag{4.24}$$

where $I(x,f)$ is the field intensity in the focal plane, F is the focal region, R is the total reflection efficiency, and α, β and γ are scalar constants. The cost function becomes zero in the ideal case when 100% of the light is transmitted and diffracted into the focal area.

The field is calculated using the stitching method introduced in section 4.4.1. In contrast to the design of the NSGRIN lenses introduced in the previous section, the cost function has many local minima. The T coefficient and the cooling schedule are therefore more important in order to avoid poor results of the design algorithm. The most successful schedule is a slow exponential cooling where T is decreased after several accepted changes. The ideal start value T_0 and the factor by which T is decreased are strongly dependent on the number of pixels and layers as well as the refractive index contrast of the materials. For an appropriate choice of the parameters and focal area, the algorithm leads to diffraction limited focusing. When taking the polarisation into account, it is possible to design lenses with two separated foci in the near field region, as Li and Webb demonstrated theoretically [112].

Figure 4.19 shows a result of the simulated annealing algorithm. It was designed for microwaves with $\lambda = 3\,\text{cm}$ and a focal length of 30 cm. The structure consists of 5 layers with 50 pixels each and has a mirror symmetric material distribution. Each pixel has a size of 5 by 5 millimetres and can take two different values of the refractive index: $n = 1$ or $n = 1.61$. For plane wave illumination, this lens achieves a diffraction limited spot size. The focal area F in equation 4.24 was chosen to be 6 cm.

The thickness of the structured lens compared to a normal gradient index lens with the same index contrast and focal length can be reduced by a factor of more than

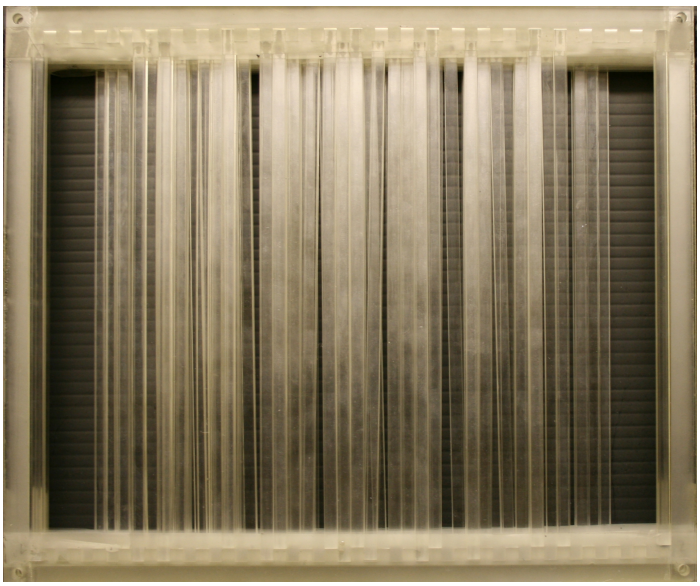

Figure 4.20: Front view of the assembled microwave lens. In each layer, the square rods are assembled in a frame which are then stacked to form the structure shown in figure 4.19.

two. Due to the scalability of Maxwell's equations, a structure with 0.17 µm feature size has the same effect for $\lambda = 1\,\mu m$ and 10 µm focal length.

4.4.3 Experimental verification of the simulated results

To provide experimental verification of the simulations from this chapter, the microwave lens was assembled and characterised. Perspex has a refractive index of $n \approx 1.6$ for a wavelength $\lambda = 30\,mm$ and is therefore well suited for the above designed structure. Each layer of the lens is assembled from square Perspex rods with side length $s = 5\,mm$, which are hold in place by a frame. Finally the five Perspex-air phase gratings are stacked and held together by screws in each corner. The length of the grating, which is assumed to be infinite in the simulations, is 20 cm. The measurements of the field cross section are taken in the middle of the structure where the effects of the edges and the screws are the smallest. To eliminate diffraction effects from the field outside the grating, the lens was surrounded by microwave absorbing material during the measurement. Figure 4.20 shows a photograph of the lens structure that was used in the experiments.

The experimental setup, shown in figure 4.21, is as follows: A vectorial network analyser (HP8510B) is used as source as well as detector of the microwave signal by using its two channels. The source signal is increased by an external amplifier and connected to a horn antenna. Between the VNA and the amplifier, a circulator has to be installed which absorbs any back reflections from the amplifier. The length of the horn antenna is 25 cm with an emitter surface of 8 cm×8 cm. It emits a spherical wave with a Gaussian intensity profile. To achieve an illumination similar to a plane

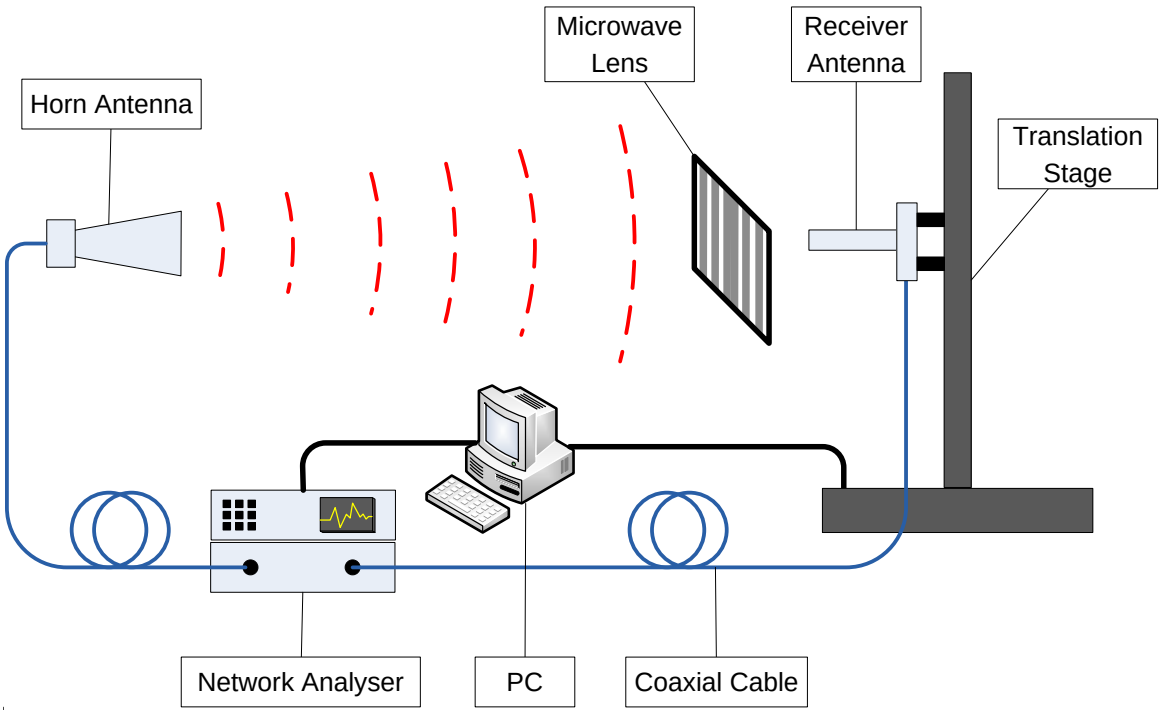

Figure 4.21: The experimental setup to characterise the lamellar microwave lens. The network analyser is used as source and detector, the signal is transmitted with coaxial cables to the horn antenna and from the receiver antenna. The translation stage can move freely in the plane parallel to the lens. The drive of the translation stage and the measurement signals are processed with a PC.

wave for which the lens was designed, the distance between lens and transmitter is chosen to be as large as possible (d≈2.5 m). The lens is placed 32 cm away from the detector which is aligned to the centre of the lens in order to minimize diffraction effects from the edge of the grating. The receiver antenna has a cross section of a standard rectangular X-band waveguide with side lengths of 2.3 cm × 1.0 cm. Any oscillations in the intensity profile that are smaller than this are not detectable. The lateral dimensions of the focus is in the order of 10 cm so the intensity changes are on a scale large enough to be measured properly with this method. With the VNA, both the amplitude and the phase of the field can be measured for each point of a predefined mesh grid. In the case of the cylindrical lens, a simple line cross section is measured with a step width of 5 mm. A fixed wavelength of $\lambda = 30$ mm is chosen for the experiment. To reduce the signal, induced by scattering at surrounding objects, the system is built inside a chamber with microwave absorbing walls. This ensures that the reflections from the surroundings are kept to a minimum.

Figure 4.22 shows the comparison of the experimental data with simulations obtained from the FMM. The central spot shows diffraction limited behaviour with the diffraction limit being marked by the black dotted line. The green dashed line shows the expected cross section of the field at the lens which is nearly identical to the diffraction limit. The experimental data however has higher sidelobes as expected

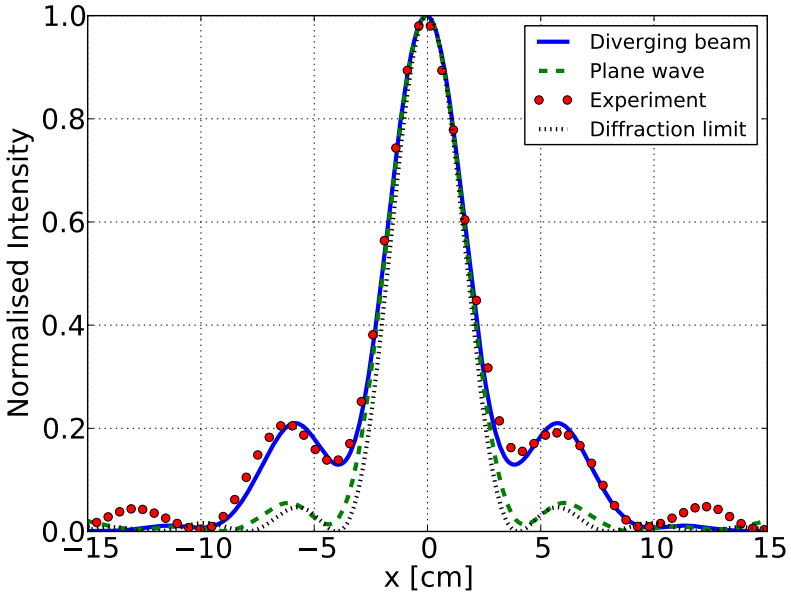

Figure 4.22: Comparison of the theoretical and experimental results from the lamellar microlens. The measured spot width is close to the diffraction limit (black dotted line). The first sidelobes are higher than expected for plane wave illumination (green line). When using a slightly curved incident wave in the calculations (blue line), the simulations show very good agreement with the experiment (red dots).

which is due to the incident beam, which has a slightly parabolic phase profile. By introducing a phase difference in the illuminating wave of $\Delta\phi = 0.18\lambda$ between the centre and the outer edge of the lens, the simulations can be matched to the measurements. With the available equipment it was unfortunately not possible to generate a perfectly plane wave. From the distance d between the lens and the horn antenna the expected path length difference can be calculated with the equation

$$\Delta s = (\sqrt{d^2 + (w/2)^2} - d) \tag{4.25}$$

where w is the full width of the lens. With the given values for the parameters the path length difference is about 0.1λ which is a bit lower than what was found in the simulations. Although the design was made to optimise focusing by only considering TE polarisation, TM polarised light is also focused, the polarisation sensitivity of this structure is very small.

Chapter 5

Characterisation of Structured Microwave Lenses

The fabrication and characterisation of microlenses as described in chapter 4.2 is very time consuming and expensive. The stacking of the preform alone can take a skilled person up to several days. The two to three drawing steps, and the dicing and polishing of the final lenses require many process steps in various laboratories.

To simplify and expedite the experimental verification of theoretical predictions, an easy and flexible way of testing new structures had to be found. Like in the design of lamellar gratings, the scalability of Maxwell's equations is used here. By building a scaled up model of the nanostructured NSGRIN lenses in the microwave regime, the same experimental setup as for the cylindrical lens can be used. Rather than assembling multi layer gratings, the two dimensional pattern is assembled by cylindrical rods in a transparent box where each rod represents one pixel of the pattern.

The material, used for the scaled up lenses, is Polytetrafluoroethylene (PTFE, also known as Teflon). PTFE is nearly transparent for centimetre waves and has a permittivity of $\epsilon = 2.05 \pm 0.05$. The value of the permittivity depends on temperature and also the way how it was fabricated. Literature values range from 2.016 to 2.1 [113–115], so $\epsilon = 2.05$ will be assumed in further calculations.

To achieve pixels with different refractive indices, the structure is assembled from solid PTFE rods and hollow tubes. The tube has a much lower material fill factor than a solid rod, therefore its effective refractive index is lower. Cylindrical rods naturally assemble in a close-packed pattern which has a hexagonal unit cell. In this hexagonal pattern the fill factor of the rods and tubes, from which the effective index

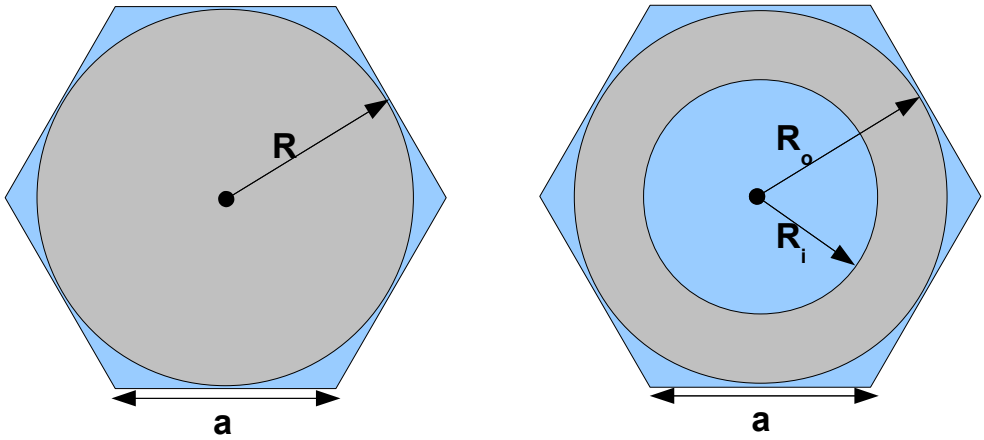

(a) The solid PTFE rod with effective index $n = 1.407$

(b) The hollow PTFE tube with effective index $n = 1.124$

Figure 5.1: The hexagonal unit cells that are used for the assembly of the lens. They have a radius $R = 3\,\text{mm}$ in diameter are either occupied by a solid rod (a) or a tube with inner radius $R_i = 2.5\,mm$ (b). This gives two different effective indices which are used for the design algorithm.

of the unit cells are obtained, is calculated by

$$f_{rod} = \frac{\pi}{2\sqrt{3}} \approx 0.907 \tag{5.1}$$

$$f_{tube} = \frac{\pi}{2\sqrt{3}} \left(1 - \frac{R_i^2}{R_o^2}\right). \tag{5.2}$$

Figure 5.1 shows the two hexagonal unit cells from which the structure is assembled. In order to achieve a refractive index contrast as high as possible, the wall thickness of the tube has to be small compared to the diameter. For the assembly of the lenses, rods with a diameter of 6 mm and tubes with an outer diameter R_o=6 mm and inner diameter R_i=5 mm are used. This results in a fill factor for the tubes of $f_{tube} = 0.277$. The effective refractive index is then calculated with the Maxwell-Garnett equation (see eq. 4.7) by using $\epsilon_{teflon} = 2.05$ and $\epsilon_{air} = 1$:

$$n_{rod} = 1.397 \qquad n_{tube} = 1.136. \tag{5.3}$$

In the design algorithm, these two values will be used as possible refractive indices for each pixel. The effective index profile is then calculated as an average over several pixels. No additional numerical error is introduced by this approach, because the permittivity is still calculated according to the exact material fill factor.

The lenses in this chapter are designed for a microwave source with $\lambda = 30\,\text{mm}$ ($\nu = 10\,\text{GHz}$), so the diameter of the rods is 0.2λ in this configuration. This ratio between feature size and wavelength is at the upper limit of the effective medium

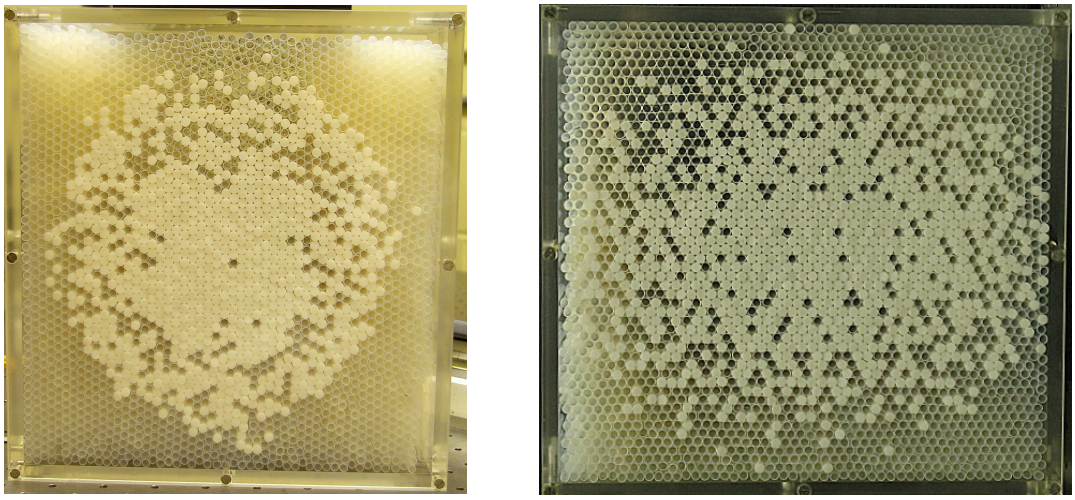

(a) Spherical lens (b) Elliptical Lens

Figure 5.2: The two lenses that have been assembled and characterised in the microwave regime at $\lambda = 3\,\text{cm}$. The side length of the pattern is $30\,\text{cm} \times 28\,\text{cm}$ and contains 50×54 rods and tubes in hexagonal packing.

approximation, smaller rods and tubes however are practically not feasible. Lalanne et al. showed that for one dimensional subwavelength gratings with a wavelength to period ratio of 5, the error is still in the range of a few percent [71]. Therefore, the results of the experiments are expected to be reasonably good but not perfect.

In order to include a sufficient number of pixels in the calculation of the effective index, the neighbourhood in equation 4.7 needs to be chosen relatively large. In the design algorithm, the average index is calculated from a circular neighbourhood with radius $R = 1.5\lambda$.

The 10 cm long rods and tubes are assembled to the required pattern, by stacking them in a perspex box with dimensions $30\,\text{cm} \times 30\,\text{cm} \times 10\,\text{cm}$. Due to the hexagonal packing, this frame contains a pattern with 50 rods in x and around 55 rods in y. The box needs to be filled completely to guarantee that the rods are kept on their place. After finishing the assembly, the perspex box is closed so it can be kept upright for the experiments.

For the experimental characterisation, two structures are designed: one spherical lens and one elliptical lens. The effective medium approach is used in the design algorithm to find the best pattern for the target index profile. To simulate the exact performance of the final design, the FDTD method is used.

Figure 5.2 shows photos of the two different lenses. The white areas are the solid rods and the darker areas are assembled from tubes. The wall thickness of the perspex box is 1 cm which has not been taken into account in the simulations.

The experimental setup is nearly identical to the setup used in chapter 4.4 for the experiments with the lamellar lens (Fig. 4.21). For the measurements, the lens

is placed upright about 3 m away from the horn antenna. To change the distance between detector and lens, the lens has to be moved between emitter and receiver as both the detector and the horn antenna are fixed. This method might introduce a small error because the curvature of the incident wave changes slightly when changing the distance between the emitter and the lens. However, due to the small change of the distance, this does not have a big effect on the results.

The horn antenna emits a spherical wave with a Gaussian intensity profile. For a spherical wave, the path length difference Δl between the centre and the outer edge of the lens at a distance z, can be calculated with equation 4.25 in the same manner as for the lamellar lens. By positioning the lens about 3 m away from the source, the maximum path length difference is $0.375\,\mathrm{cm} = 0.125\lambda$. As shown before in chapter 4.4 the phase curvature mainly influences the magnitude of the side lobes.

For each measurement of the field distribution of a plane, the intensity is automatically normalised to 1 by the software, so it is only possible to compare the shape of the beam in each plane with the simulations. The comparison of the intensity between different planes is not possible. However, with the intensity as well as the phase being measured, the propagation of the field can be calculated using the angular spectrum of plane waves (ASPW) algorithm [48]. From this, the complete three dimensional field representation of the experimentally measured field can be calculated.

To find the actual theoretical performance of the designed structure, a rigorous method has to be applied. The simulations for the internal field were performed by J. Nowosielski with the FDTD method [77], using the freely available software package Meep [116]. In the simulations, the structure was defined by hexagonal pixels with refractive indices as calculated in equation 5.3. The calculations were performed with a spatial step size $\Delta s = 0.1\,\mathrm{cm}$ and temporal step size $\Delta t = 1.667 \cdot 10^{-12}\,\mathrm{s}$. The structure is illuminated by a planar wave with wavelength $\lambda = 3\,\mathrm{cm}$. To reduce the computational cost, the FDTD simulations only go 1 cm beyond the back surface of the lens. The computational space is surrounded by a perfectly matched layer to eliminate effects from the boundary conditions. Furthermore, the lens is surrounded by a frame of size 10 cm with refractive index of the tubes ($n = 1.124$).

The free space propagation of the simulated transmitted field is calculated using the ASPW algorithm. As starting point for these calculations, the complex field at the back surface of the lens, calculated by the FDTD method, is used. The ASPW algorithm is based on the Fourier transformation of the field and has therefore periodic boundary conditions in x and in y. In order to prevent interference effects, that are introduced by the periodic boundary conditions, the field at the back surface of the lens is embedded in a larger computational cell. The field values outside the lens structure are set to zero as the lens in the experiments is surrounded by microwave absorbers. Light, that is diffracted at a certain angle, now reaches the

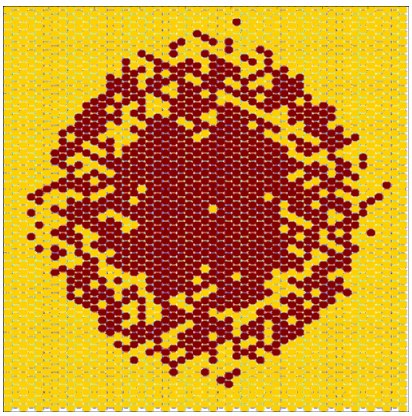

(a) The lens design

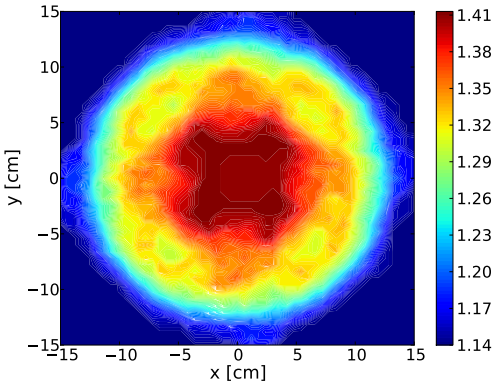

(b) Effective index of the pattern

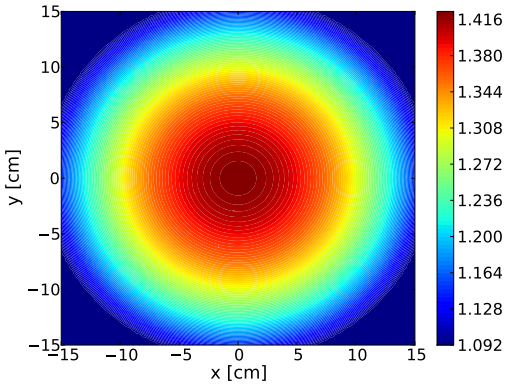

(c) The target refractive index profile

Figure 5.3: (a): The pattern of the spherical design. Yellow circles represent Teflon tubes and red circles represent solid rods. (b): The refractive index profile of the structured calculated for a neighbourhood area with radius $r = 0.8\lambda$. (c) The target index profile has a radial parabolic shape with $n_{max} = 1.407$ and $n_{min} = 1.124$

computational boundary much later. Due to the increased computational cell, the artificial interference starts at a distance further away from the lens than the area of interest. This approach is numerically similar to the method, that was introduced for non-periodic lamellar gratings, analysed by the Fourier modal method in chapter 4.4.

5.1 Spherical Microwave Lens

The spherical microwave lens was designed for a pitch length $p = 150\,\text{cm}$. Figure 5.2a shows a photographic image of the assembled lens. During the stacking of the rods and tubes, the lens structure was slightly distorted. This is due to the Teflon tubes which were bent and thus could not be assembled in a perfect pattern and caused the lens to be slightly elliptical. However, this effect does not cause a large error in the focusing behaviour. The designed pattern of the lens is displayed in figure 5.3a. Red circles are solid PTFE rods, the yellow circles represent the tubes respectively.

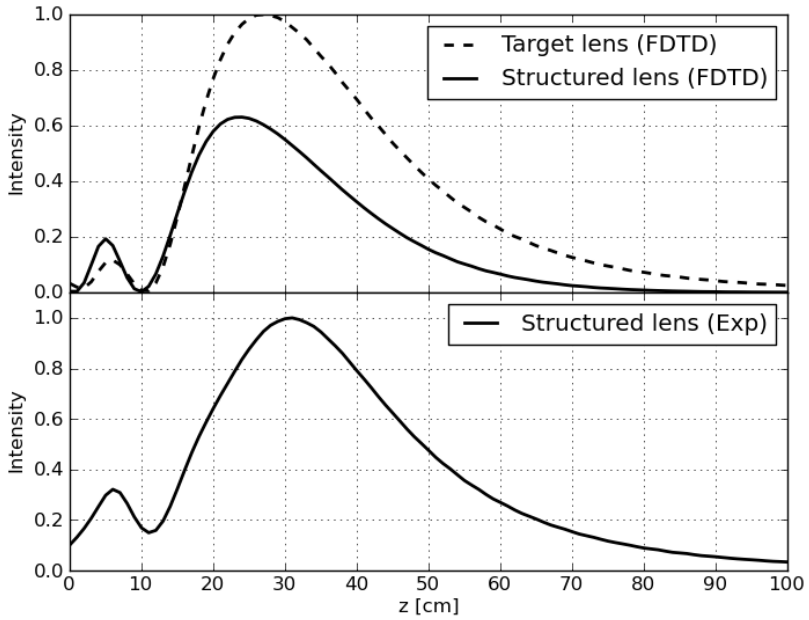

Figure 5.4: The normalised intensity on the optical axis of the spherical microwave lens as a function of the distance to the back surface. The simulations of the target lens (dashed line) and the structured lens (solid line) are displayed in the upper part whereas the propagation of the experimental field is displayed in the lower part of the diagram.

The effective refractive index profile is displayed in figure 5.3b. It is not perfectly symmetric and also has a ring feature at a radius of about 10 cm from the center which has a too high index. This design was produced in an early stage of the project when the parameters for the design algorithm still had to be fine tuned. Figure 5.3c shows the refractive index profile of the associated target GRIN lens. By using the pitch length $p = 150\,\text{cm}$ and the thickness $t = 10\,\text{cm}$, the expected working distance can be calculated from equation 4.12 and 4.11. For this lens, the focal length is $f = 26\,\text{cm}$.

5.1.1 Intensity

The working distance of GRIN lenses is defined as the distance from the back surface of the lens to the plane, where the intensity reaches its maximum. Figure 5.4 shows the intensity on the optical axis as a function of the distance z to the lens. The values for both the simulations and the experiment were calculated with the ASPW algorithm as described in the introduction.

The upper diagram in figure 5.4 shows the simulated results of the intensity on the optical axis of the target GRIN lens (dashed line) and the structured lens (solid line), respectively. The target lens and the structured design were simulated with the same amplitude of the incident field. The focal length of the patterned lens is

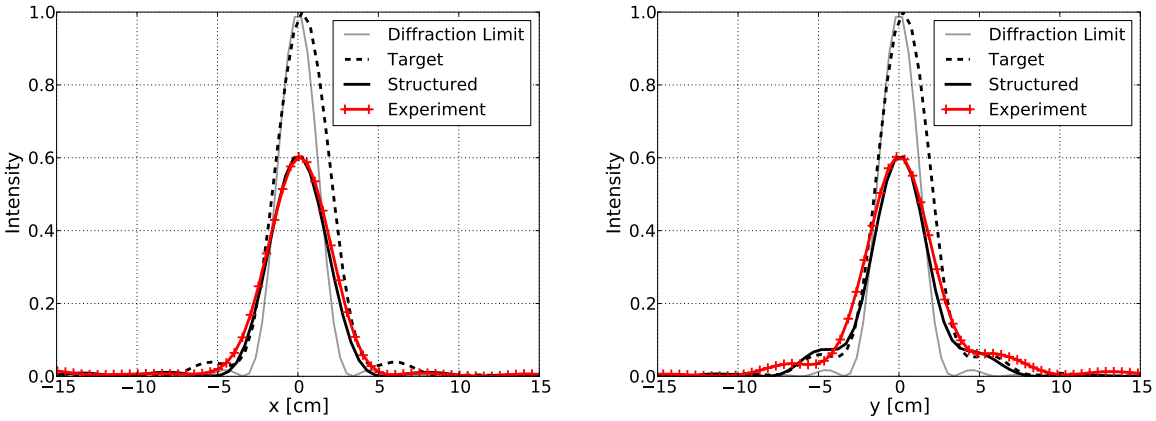

(a) Intensity cross section along the x axis

(b) Intensity cross section along the y axis

Figure 5.5: The cross section of the intensity in the focal plane at $z = 27.5\,\text{cm}$. The spot size of the target lens (dashed line) is nearly diffraction limited. Simulations of the structured lens (solid black line) show that the peak intensity is about 40% lower than the ideal case and show good agreement with the experimental data (red line). Here the intensity of the experiment is normalised to have the same peak value as the simulations.

24.5 cm which is shorter than the focal length of the ideal lens (f=28 cm). However the design of the lens is relatively crude as it was designed at an early stage of the research. Its refractive index profile is not very close to a parabolic shape, therefore it is not surprising that the behaviour is not the same compared to the target GRIN lens. Moreover, the peak intensity of the patterned lens is lower compared to the ideal lens which means, more light is lost due to scattering. Despite the intensity difference of around 40%, the structure focuses the wave to a nearly diffraction limited spot.

The intensity distribution on the optical axis of the experimentally measured field is displayed in the lower diagram of figure 5.4 which was normalised to a maximum intensity of 1. Due to the normalisation of the field in each measurement, the simulated and experimental data can not be compared quantitatively and have to be plotted in separate diagrams. It is however possible to compare the characteristics such as focal length and the shape of the curve. The focal length of the experimental field is $f = 30\,\text{cm}$ which is considerably more than the expected value of 24.5 cm. Reasons for this effect are the diverging phase of the incident wave and errors in the assembly of the rods and tubes. The characteristic features of the curve however match the simulations.

In figure 5.5a and 5.5b the x and the y cross section of the field intensity in a plane near the focal length are shown respectively. The experimental values, which have been measured at z=27.5 cm, are displayed by the red line with '+' markers. They have been normalised to have the same maximum as the simulations of the structure (solid black line). The dashed line marks the simulations of the target GRIN lens. As already shown in figure 5.4, the peak intensity in the focus of the structured lens is

around 40% lower compared to a real GRIN lens.

Owing to the distortion of the lens, the cross sections on the x and y axis are slightly different. In x direction the minimum between the central spot and the first side lobe is not as low as in y direction. Furthermore, the focal length in x is slightly longer than in y, therefore the beam shape is not a Bessel function as it would be expected in the focal plane. The distance between the first two minima in y is about 1.6 times the diffraction limit which is marked by the gray line. Given the large feature size and the crude design this is still a satisfying result. The experimental data, which is a direct measurement at this distance, matches the expected distribution. In the simulations a plane wave illumination is assumed whereas in the experiment the wave is curved and has not a perfectly constant amplitude which causes the small differences.

In figure 5.6, the xz and yz cross sections of the experimental data, the simulations of the structured lens and the simulations of the target grin lens are compared. The cross sections in both directions intersect the optical axis at $x/y = 0$. In all three cases, the field distribution is calculated by propagating it from $z = 0$ using the ASPW algorithm. The spatial resolution of the measured and the simulated field cross section at $z = 0$ is 0.5 cm. As the experiment was performed by surrounding the lens with microwave absorbing material, so that light could only be transmitted through the lens, the simulations need to be cropped to the same dimensions. The field was measured in an area of 35 cm × 35 cm but the field outside the 30 cm × 30 cm lens is blocked by the microwave absorbers. The field from the FDTD simulations is therefore also restricted to an area of 30 cm × 30 cm in order to have the same configuration as in the experiment. To reduce the interference, induced by the periodic boundary conditions of the ASPW algorithm, the field is embedded in a larger optical window, so that the diffracted light reaches the edge of the computational cell behind the area of interest. The total size of the computational cell is 512 × 512 pixels (=256 cm × 256 cm) and the step width of the propagation in z is 1 cm.

Figures 5.6a and 5.6b show the simulations of the target GRIN lens displayed in figure 5.3c. As expected, the beam shape is identical in both planes. The focus area looks like it would be expected for a standard lens.

The simulations of the structured lens (Fig. 5.3a) are displayed in figures 5.6c and 5.6d. In this case, the cross section of the xz plane differs from the yz plane, however only to a small extend. The characteristics of this lens look as would be expected from a slightly elliptical lens. Due to the design, which is not perfectly symmetric, different planes can have different cross sections. Here, the focal length in the xz plane is shorter than in yz, which causes the spot in the yz to be wider in the area just before the focus. In these diagrams, the color scale has a different range compared to the case of the target lens in order to get the best contrast.

Figures 5.6e and 5.6f display the experimental field distribution. The difference of

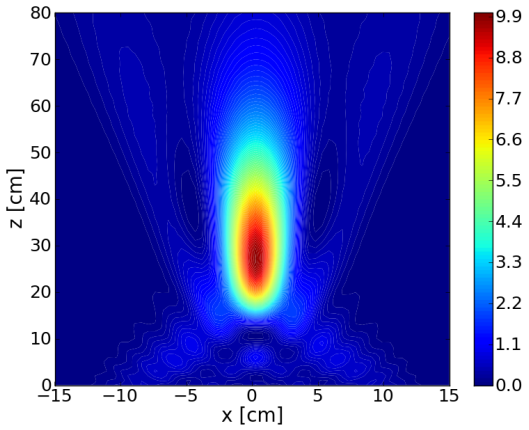

(a) xz cross section of the simulated field of the ideal GRIN lens

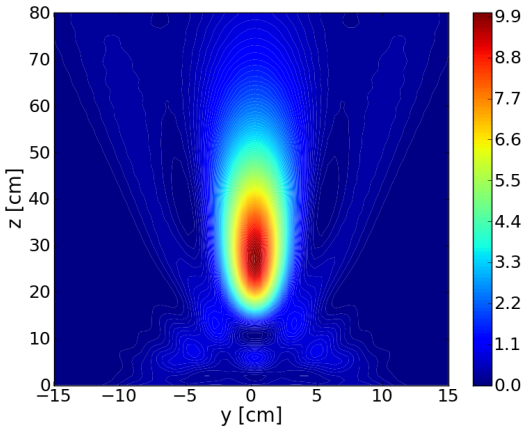

(b) yz cross section of the simulated field of the ideal GRIN lens

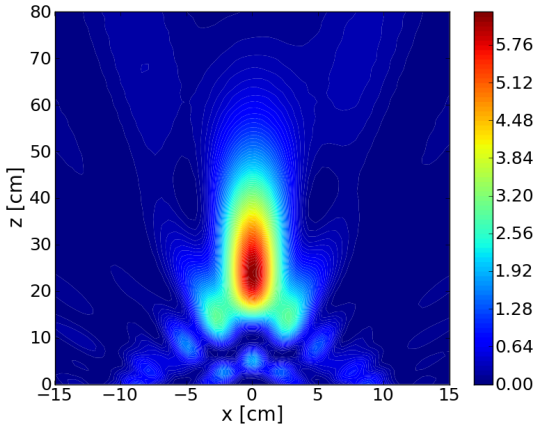

(c) xz cross section of the simulated field of the structured lens

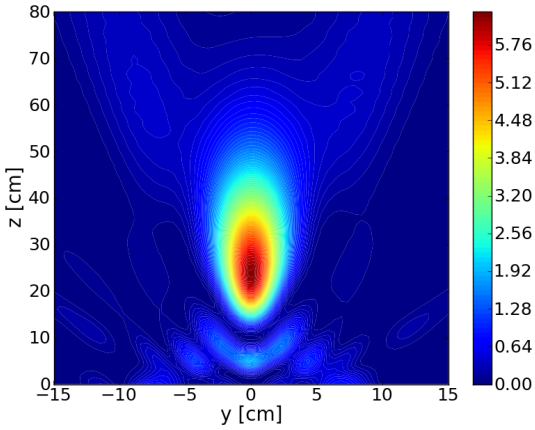

(d) yz cross section of the simulated field of the structured lens

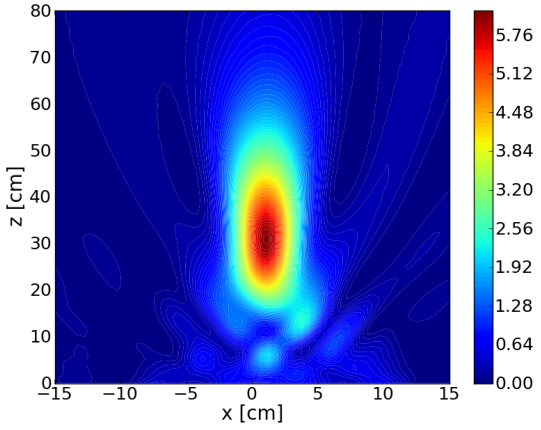

(e) xz cross section of the measured field

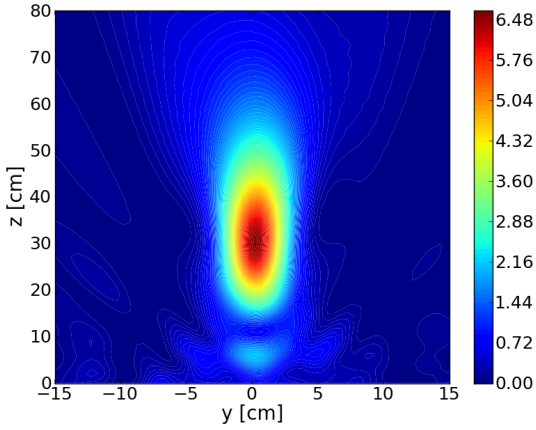

(f) yz cross section of the measured field

Figure 5.6: Cross sections of the xz and yz planes through the optical axis. (a) and (b) show simulations of the target lens, (c) and (d) show the simulations for the structured GRIN lens, and (e) and (f) show the propagated light of the measured field. The field at each distance z is calculated from the complex field at $z = 0$ using the ASPW algorithm.

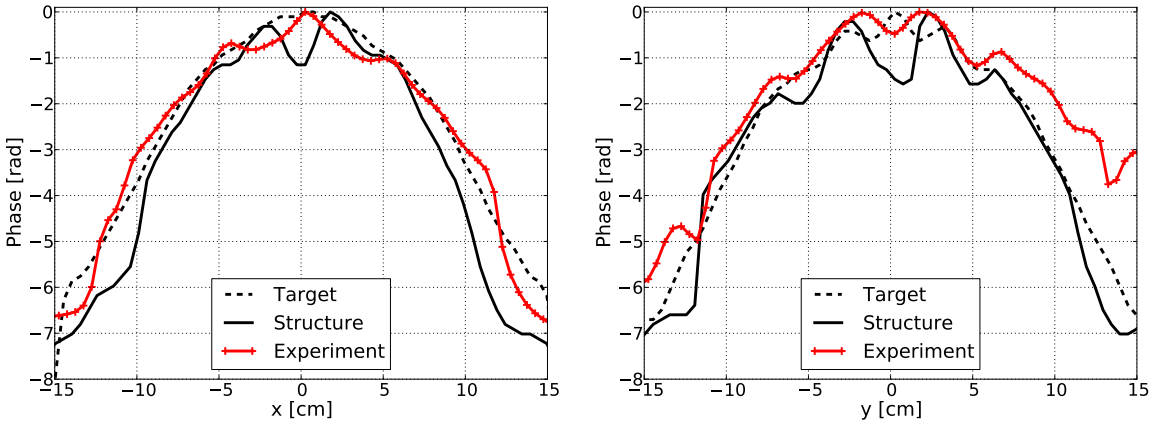

(a) The phase cross section along the x axis (b) The phase cross section along the y axis

Figure 5.7: Unwrapped phase cross sections along the x-axis (a) and the y-axis (b) at $z = 0$. The experimental values (red "+") match the target lens (dashed line) and the simulations of the structured lens (solid black line). The difference in positive y is due to an air gap in the assembled lens.

the intensity of the two planes is very close to the simulations. The same characteristics of a lens with a slightly different focal length in x and y is present. Due to the reasons explained earlier, the absolute value of the intensities cannot be compared to the simulations. The main difference is the position of the focus which is 5 cm farther than in the simulations, which could already be observed in figure 5.4.

5.1.2 Phase

For an ideal macroscopic lens in the paraxial domain, the phase profile of the wavefront at the back surface is parabolic. Lenses, that are only a few wavelengths in diameter however, show a slightly different behaviour as diffraction effects become also important and the thin lens approximation which is used for macroscopic lenses cannot be applied. In this case, the result is a parabolic phase profile with a superimposed diffraction pattern. In figure 5.7, the cross sections of the phase at the back surface of the lens along the x and y axes are displayed. The solid red line with '+' markers shows the experimental values, the black lines show the results from the FDTD simulations for the target lens (dashed) and for the structured lens (solid), respectively.

The experimental phase cross section in x direction agrees very well with the simulations for both structured and target lens. The interference pattern in the center is not as defined as expected from the calculations. These near field effects are changing very quickly with the distance and are very sensitive to the structure of the lens. Small errors in the distance between lens and detector could cause such differences. The errors in the assembly do not have a strong effect on the focus and the far field, but at very close distances they can affect the amplitude and phase distribution of

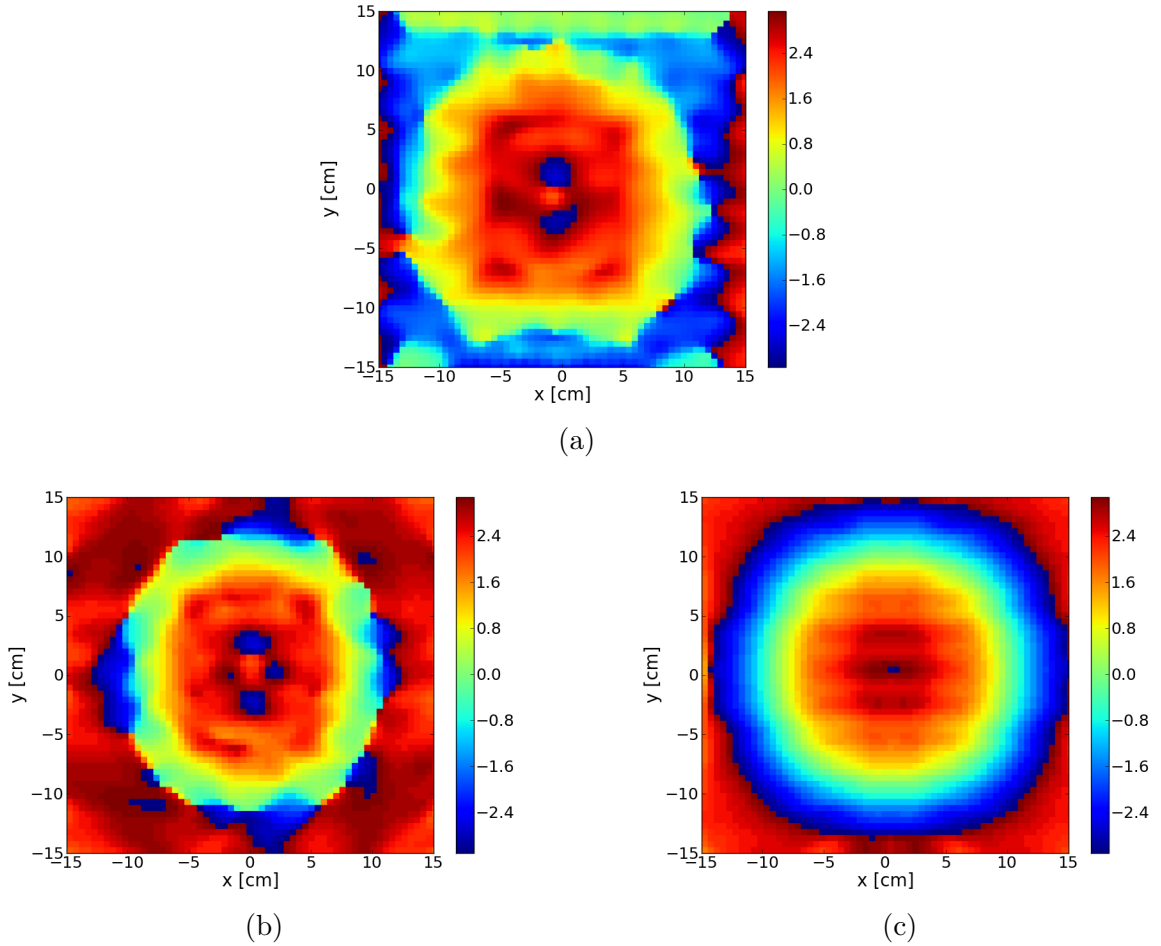

Figure 5.8: The phase profile in the xy plane at $z = 0$. (a) shows the measurements, (b) displays the simulations of the structured lens and (c) displays the simulations of the target lens. The experimental phase was shifted by a constant phase offset to match the simulations.

the near field.

In y direction, the interference pattern in the center of the lens agrees nicely with simulations. For positive y values, the phase does not drop as expected from the model. This is caused by a small part on the upper part of the assembled lens which could not be filled because there were not enough PTFE tubes available at this stage of the project. During the experiments, there was a small air gap above the lens which causes an increase of the phase in this region. This effect is better visible in the false colour plot in figure 5.8a. On the upper part of the lens at the position of the air gap, there is a small area where the phase increases. Apart from this error, the measured phase shows a similar behaviour as the target GRIN lens which is marked by the dashed line. Both, simulation and measurement of the structured lens show a stronger diffraction pattern than the phase cross section of the target lens.

The experimental phase is slightly narrower in the y cross section than in the x cross section. This effect is due to the hexagonal stacking of the rods and tubes that results in a distortion of the effective refractive index distribution.

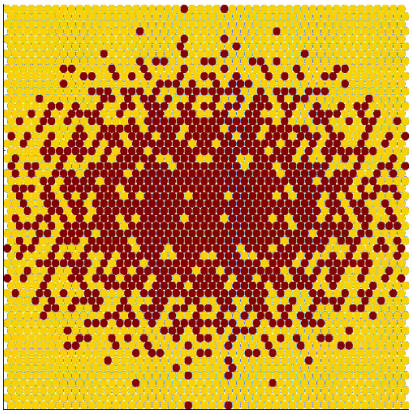

(a) The design of the elliptical microwave lens

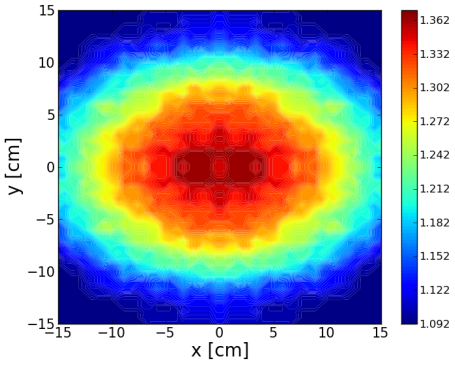

(b) The effective index distribution

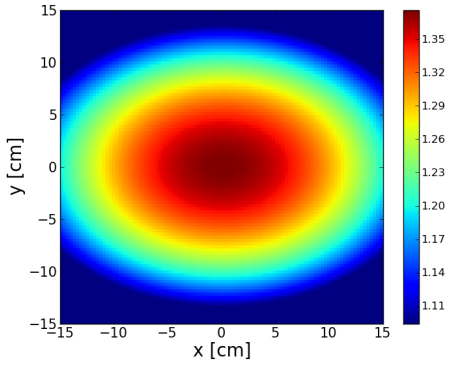

(c) The target refractive index profile of the elliptical microwave lens

Figure 5.9: (a): The pattern of the elliptical microwave lens. Yellow circles represent Teflon tubes and red circles represent solid rods. (b): The refractive index profile of the structured lens calculated for a neighbourhood area with radius $r = 0.8\lambda$. (c): The target index profile has an elliptical parabolic shape with $n_{max} = 1.407$ and $n_{min} = 1.124$

In figure 5.8, the phase profiles at the back surface of the lens are displayed. Apart from the upper 2 cm, the experimental phase (5.8a) shows good agreement with the simulations of the structured lens (5.8b). There is however a distinct difference to the target lens displayed in (5.8c). The expected phase of the target lens is smoother and has less noise on the parabolic profile.

These experiments show that a design for feature sizes of $\lambda/5$ can lead to poor results of the lens performance. However, despite the crude design of the structured GRIN lens, the behaviour is similar to a real GRIN lens.

5.2 Elliptical Microwave Lens

The second lens which was assembled and characterised is an elliptical lens. It was designed with an improved design algorithm. Rather than using a squared neighbour-

hood as in the case of the spherical microwave lens, the effective index was calculated for a circular neighbourhood taking into account that the rods are stacked in a hexagonal pattern. This decreases the risk of getting clustered areas or regular patterns in the design.

Also, the radius of the neighbourhood was optimised. which is directly related to the number of refractive index levels between the two values of the glasses. The number of rods that are taken into account for the calculation of the effective index give the number of possible refractive index values of the effective index profile. A too large radius however can result in a design where index changes on a small spatial range are smoothed out. Therefore it is necessary to choose a radius large enough to insure that the index steps are not too coarse and small enough in order to get a strong enough localization. In the case of the spherical lens, a too small area was used, which resulted in the very large area of constant index in the center.

Another improvement in the design algorithm is that symmetries are used if applicable. In this case, the structure was designed to have mirror symmetry along the x and the y axes.

Figure 5.9a shows the pattern of the elliptical microwave lens. Its pitch length is $p_x = 200\,\text{cm}$ in x direction and $p_y = 150\,\text{cm}$ in y direction, the thickness of the lens is 10 cm and the side lengths are 30 cm × 30 cm.

Figures 5.9b and 5.9c show the effective index profile of the structured lens and the target profile, respectively. The effective index shows much better agreement with the target compared to the spherical microwave lens in the previous section. In the design algorithm and for the calculation of figure 5.9b a neighbourhood with radius of four pixels was used. The symmetry in the design is slightly skewed, which is due to the hexagonal pattern where every second line is shifted by half a pixel.

With equations 4.11 and 4.12 the working distance can be calculated, i.e. the distance of the focal plane to the back surface of the lens. The focal length for the two main axes are

$$f_x = 71.63 \pm 6.56\,\text{cm}, \qquad f_y = 34.73 \pm 1.88\,\text{cm} \tag{5.4}$$

5.2.1 Intensity

Figure 5.10 shows the normalised intensity on the optical axis as a function of the distance to the back surface of the lens. The upper part of the diagram shows the simulated results of the target lens (dashed line) and the structured lens (solid line), respectively. The focal length of the structured lens is a bit longer than the focal length of the target: it peaks at 34 cm compared to 31 cm for the target. The peak intensity is only 3% lower, so the scattering loss is nearly negligible.

The experimental field matches the simulations very well. The peak intensity is

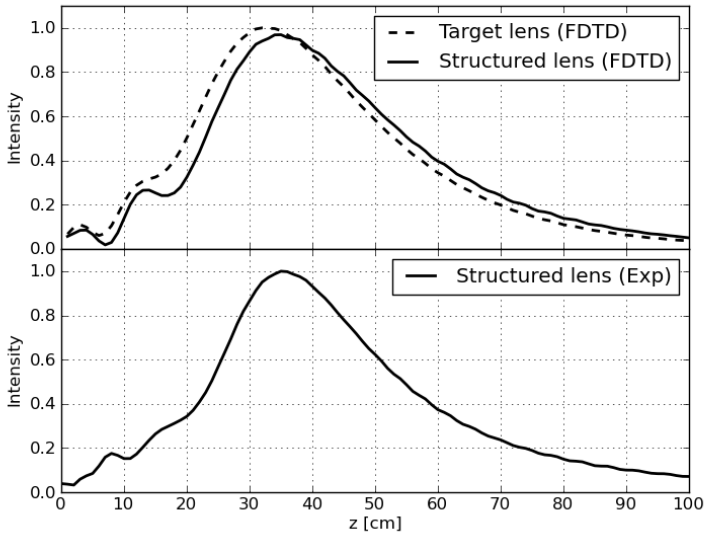

Figure 5.10: The intensity on the optical axis of the elliptical microwave lens as a function of the distance to the back surface. The simulations of the target lens (dashed line) and the structured lens (solid line) are displayed in the upper part whereas the propagation of the experimental field is displayed in the lower part of the diagram.

identical to the expected value from the simulations of 34 cm and only 1 cm longer than the prediction from the GRIN formulas. The behaviour in the near field differs a bit from the simulations but in the area of the focus and beyond, the curve has almost identical characteristics to the calculated data.

The second focus at $z = 71\,\text{cm}$ does not appear on the intensity curve of the optical axis. Due to the strong divergence in y direction the longer focal length does not cause a second focus but an asymmetry in the focus at $z = 34\,\text{cm}$. The focal spot changes from an elongated shape parallel to the x axis before the intensity peak to an elliptical spot parallel to the y axis. This behaviour is characteristic for elliptical lenses.

Figure 5.11 shows the x and y cross section through the focal plane at a distance $z = 35\,\text{cm}$. The red line with '+' markers shows a direct field measurement at this distance. The peak intensity of the simulations is nearly identical for both the target lens and the structured design. In this diagram, the intensity of the simulations is normalised so that the peak intensity of the target GRIN lens is one. The experimental data is normalised to the same peak as the simulations of the structured lens.

Both simulated cases are nearly identical around the central peak and the experimental data shows good agreement with the theoretical predictions. The main difference between the three curves lies in the first side lobe. In the x cross section (figure 5.11a), the first order sidelobes of the simulations for the structured lens have slightly higher intensity compared to the target lens. However, this difference vanishes

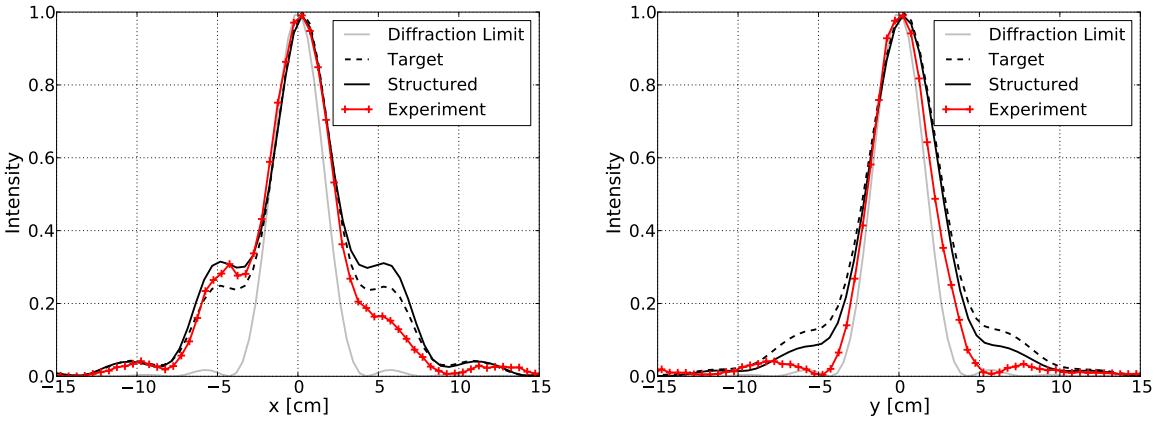

Figure 5.11: The cross section of the intensity at the focal plane ($z = 35\,\text{cm}$) of the x-axis (a) and of the y-axis (b). Experimental values are marked by red '+', the simulated data for the structured lens (solid black line) is very similar to the target lens (dashed black line). The asymmetry of the experimental data in the x cross section is due to the incident amplitude profile. In y direction the spot size is nearly diffraction limited (gray line)

at higher order sidelobes. In the experiment, the side lobe on the right hand side is lower than on the left hand side. This is caused by a not perfectly symmetric illumination. The peak of the Gaussian intensity profile from the horn antenna was not exactly centered, but shifted a bit to the left. This causes more light to be diffracted into the left side than the right side. As described in chapter 4.4, the alignment of the wave source was very difficult and a perfect centering could not be achieved.

In the y cross section (figure 5.11b) the intensity of the sidelobes is much lower compared to the x cross section which is due to the elliptical index profile. The reason for this is, that the measurement was performed at a distance of $z = 35\,\text{cm}$, which is the focus of the y axis. The spot is therefore more confined in this direction. Furthermore, the first sidelobe of the experimental data is also lower than the simulations of the target lens as well as of the structured lens. This effect becomes more evident in figure 5.12 where the xz cross section of the fields are displayed. There it is apparent, that the intensity in the two small local peaks at $z \approx 20\,\text{cm}$ are lower than in the simulations. This is probably caused by the fact that the intensity profile of the incident wave is not perfectly constant but slightly Gaussian.

In figure 5.12, the xz and yz intensity cross sections of the simulations and the experiment are displayed. In the same way as for the spherical microwave lens, the field values were calculated from the field at $z = 0$ using the ASPW algorithm. Figures 5.12a, 5.12c and 5.12e show the xz plane of the target lens, the structured lens and the experiment, respectively. Figures 5.12b, 5.12d and 5.12f show the yz cross section in the same order. The difference in the two orientations is clearly visible. As expected from a symmetric structure, the field of the simulations is mirror symmetric for both

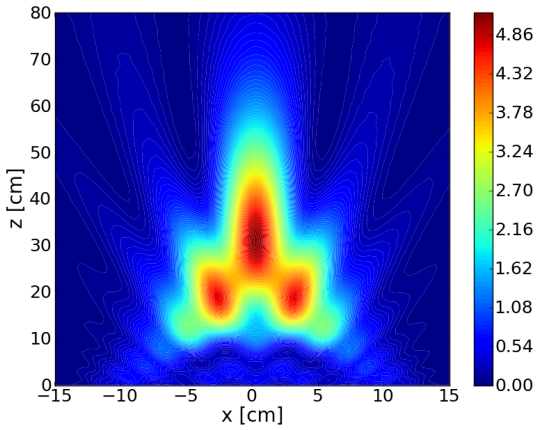

(a) xz cross section of the simulated field of the ideal GRIN lens

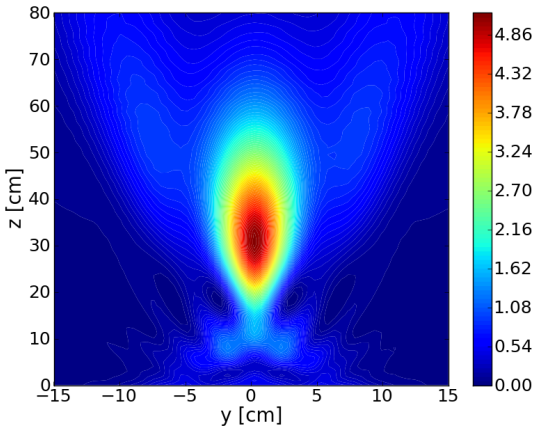

(b) yz cross section of the simulated field of the ideal GRIN lens

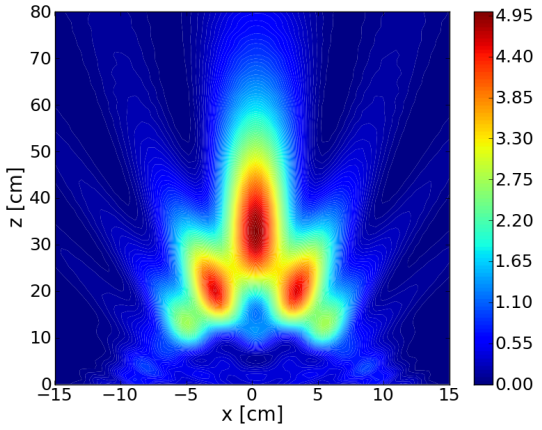

(c) xz cross section of the simulated field of the structured lens

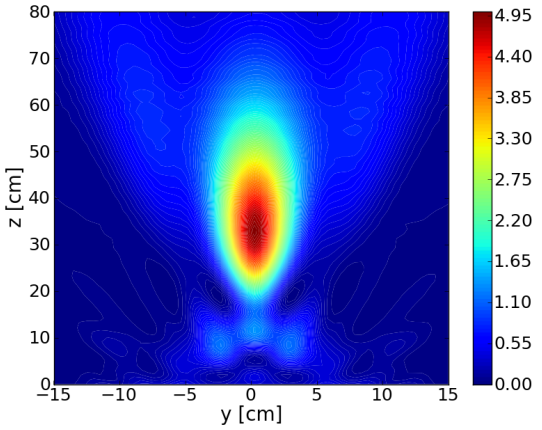

(d) yz cross section of the simulated field of the structured lens

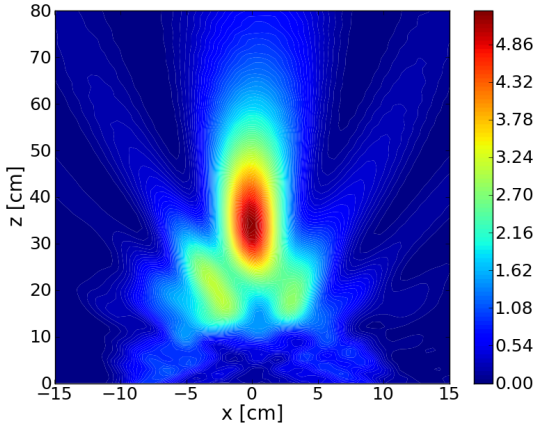

(e) xz cross section of the measured field

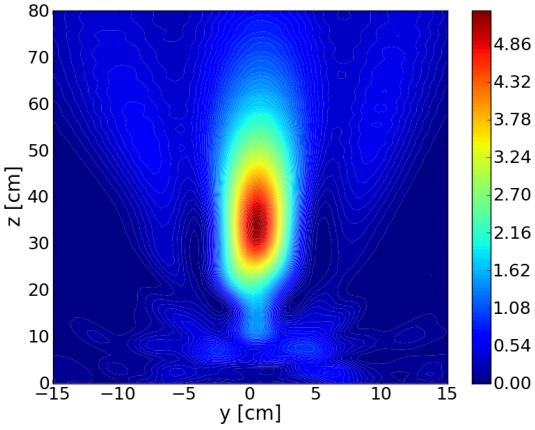

(f) yz cross section of the measured field

Figure 5.12: Cross sections of the xz and yz planes through the optical axis. (a) and (b) simulations of the target lens, (c) and (d) show the simulations for the structured GRIN lens and (e) and (f) show the propagated light of the measured field. The field at each distance z was calculated from the complex field at $z = 0$ using the ASPW algorithm.

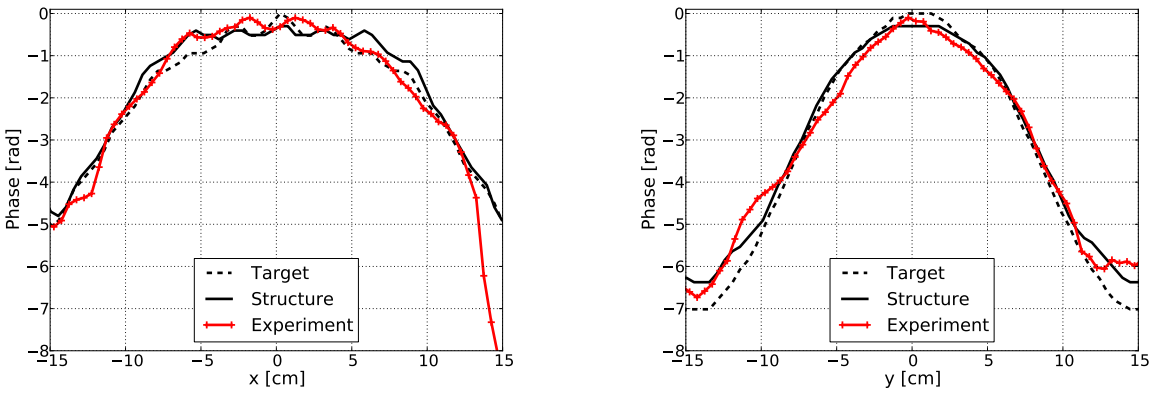

(a) (b)

Figure 5.13: Phase cross sections along the x-axis (a) and the y-axis (b) at $z = 0$. The experimental values (red line with '+' markers) match the target lens (dashed line) and the simulations of the structured lens (solid black line). The different phase curvature of the two main axes results in the two focal lengths for x and y.

the xz and the yz plane. Although the distribution of the field in both simulated cases is nearly identical, the peak intensity differs by a few percent. In order to get a high colour contrast in the diagrams, the maximum value of the colour scales in the two cases was chosen for each case independently.

As already shown in figure 5.11a, the xz cross section of the experimental data is asymmetric with more intensity on the left hand side of the beam. This effect is also visible here in figure 5.12e. The overall beam shape in xz of the experimental field, especially in the focal spot, has very good agreement with the simulations of the structure.

The cross section of the yz plane, which is the axis with the smaller focal length, has a distribution as expected for a standard lens. Again both simulations have a very good agreement, the difference of the two cases is hardly visible. The experimental cross section has a negligible asymmetry between the negative and the positive values of y. As expected from figure 5.11b, the width of the focal spot is slightly narrower than in the simulations. Again, like in the previous diagrams, the absolute values of the intensity cannot be compared between the simulations and the experiment.

5.2.2 Phase

In the same way as for the spherical microwave lens, the cross sections of the phase at the back surface of the elliptical microlens are compared in figure 5.13. The difference of the profile for x and y are clearly visible.

The cross section along the x-axis has a wider shape than along the y-axis. The simulations for the target and the structured lens are very similar. Like in the diagrams of the spherical lens, the superimposed intensity oscillations do not match perfectly,

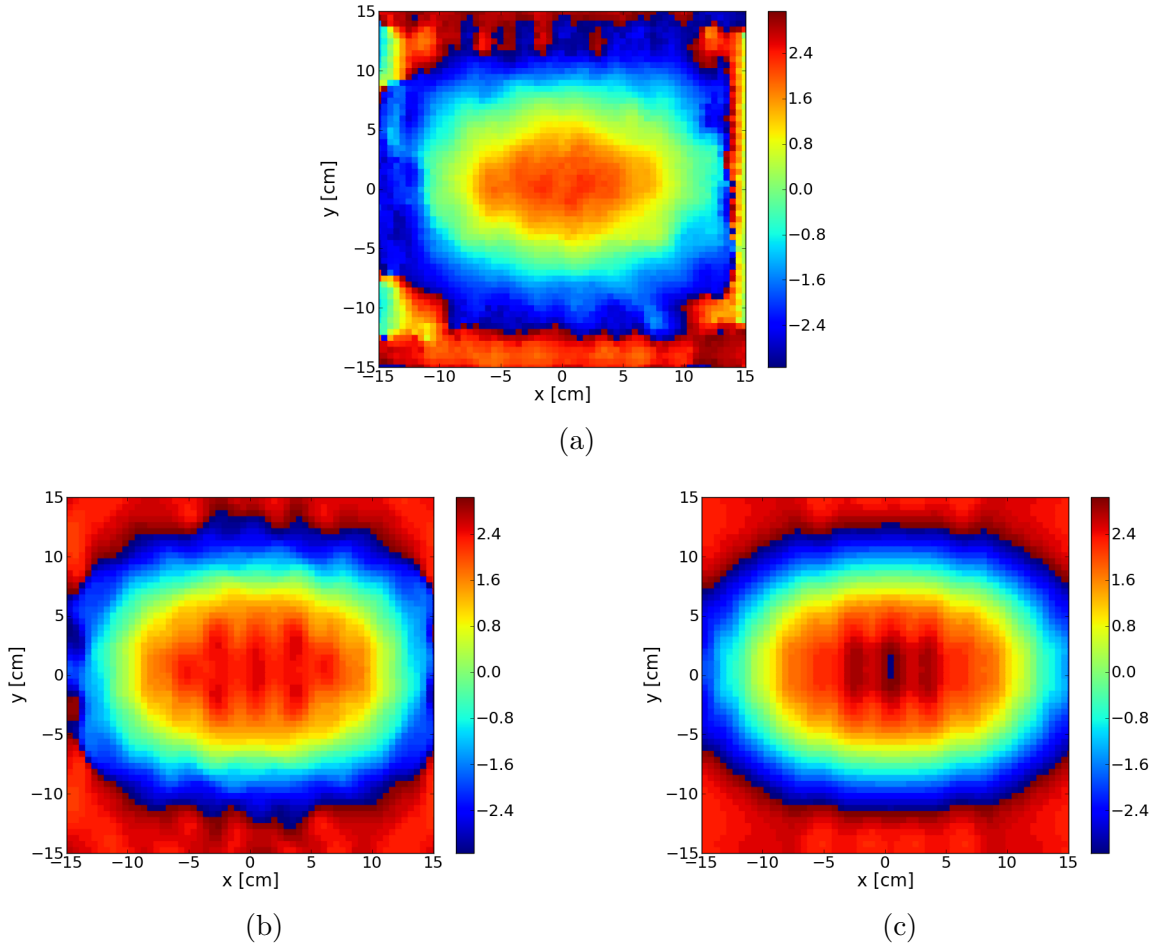

Figure 5.14: The phase profile of the elliptical microwave lens in the xy-plane at $z = 0$. (a) shows the measurements, (b) displays the simulations of the structured lens and (c) displays the simulations of the target lens.

however the spatial frequency and the strength of the modulation is comparable. The experimental data does not match the simulations perfectly but the values differ only by a few percent. For $x > +13\,\text{cm}$, the experimental phase drops much quicker than the theoretical values which is probably an effect of the material of the perspex box or the microwave absorbers.

The match of the phase cross section along the y axis also shows very good agreement. Here, all three curves are nearly identical. The experimental data has a minor asymmetry which is also reflected in the intensity cross section in figure 5.12f.

Figures 5.14a - 5.14c show the phase in the xy-plane at $z = 0\,\text{cm}$. Like in the line cross sections, the distributions of the two simulated cases are nearly identical. The profile of the structured lens has a slightly higher modulation at the boundary of phase values between $\pm\pi$. The experimental data matches the simulations much better than in the case of the spherical lens in figure 5.8. In order to get a good visual comparison, the experimental phase was shifted by a constant phase offset to match the simulations. The experimental phase of the input beam is not necessarily the same as in the simulations as it depends on the exact distance between lens and

source.

In this chapter, theoretical and experimental evidence has been given, that justifies the approach of applying the effective medium theory to nanostructured GRIN lenses. It was shown, that structures with feature sizes in the order of $\lambda/5$ can have properties that are very close to conventional GRIN lenses. However, in this regime the distribution of the materials is critical. Small errors in the design can lead to a strong decrease of the performance as it was shown with the example of the spherical microwave lens.

Due to the scalability of Maxwell's equations, the knowledge, gained from these investigations, can be directly applied for lenses in the optical regime. In the design of optical microlenses the number of rods is limited due to the maximum size of the preform that can be processed in the fibre draw tower and the manual stacking process. Depending on the requirements, the feature sizes can be chosen flexibly, i.e. if the quality of the focal spot is not critical, so a larger feature size can be used and thus the maximal lens diameter, that is achievable, is larger.

Chapter 6

Characterisation of NSGRIN Lenses

In order to prove the capabilities of the stack-and-draw technology for the fabrication of NSGRIN microlenses, two different microlens arrays were made. The first lens structure that was fabricated is a spherical microlens fabricated from F2 and NC21 glass. The structure was assembled to form an array of lens arrays with various diameters. This structure was fabricated to show the ability of the stack-and-draw technology to be used for more complex and larger structure than photonic crystal fibres and image guides.

The second lens is an elliptical microlens with diameter $d = 16\,\mu\text{m}$. During the fabrication of this lens, greater caution was taken to preserve its shape in order to be able to characterise it experimentally as well as theoretically.

6.1 Spherical Microlens

As a first proof of concept a spherical microlens with dimension of 50×50 pixels was designed using the algorithm introduced in chapter 4.3.1 with a radial symmetric parabolic refractive index distribution as target. Symmetry considerations were applied during the design process, so the pattern is mirror symmetric around the x axis as well as the y axis. However, for the calculation of the effective index, a square neighbourhood was used which lead to some clustering of the materials distribution. Figure 6.1a shows the design of the spherical NSGRIN lens. The black pixels represent the lower index glass NC21 ($n_D = 1.518$) and the white areas represent F2 ($n_D = 1.619$). Similarly to the spherical microwave lens, the transition between the central area, which mainly contains F2, and the edge of the lens, which consists of NC21 glass, is not smooth and continuous. Here again, the pattern accumulates pixels of the same material in ring like structures. Especially on the left and right hand side edges, more pixels are set to the higher index as intuitively would be expected. As in the case of the microwave lens, these effects are due to a wrong configuration of the parameters in the calculation of the effective refractive index.

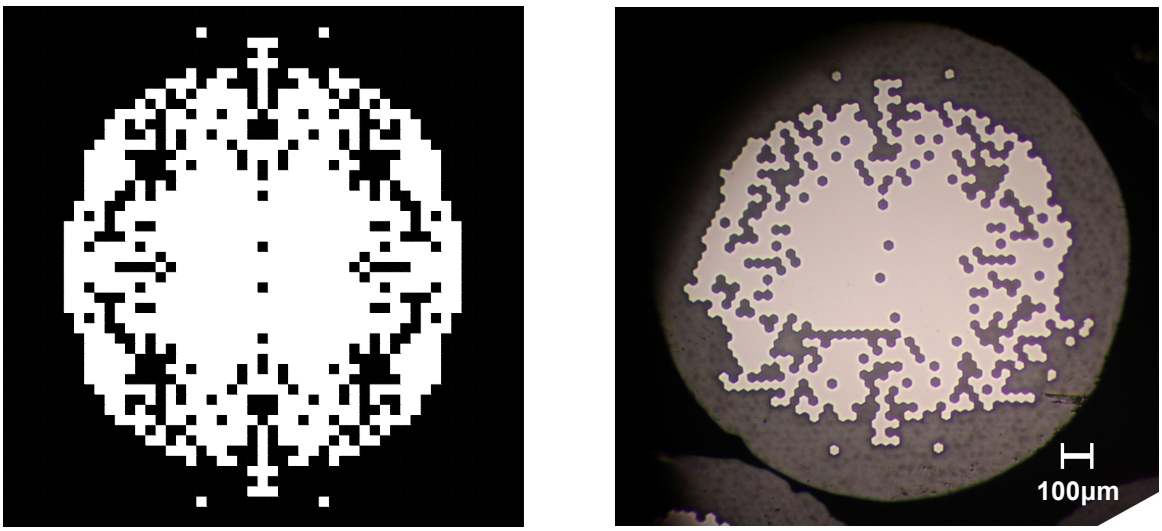

(a) (b)

Figure 6.1: The spherical microlens: the design obtained from the simulated annealing algorithm (a) and a microscope picture from the first intermediate preform (b)

This spherical lens was assembled and fabricated at ITME from the two glasses F2 and NC21. Figure 6.1b shows a microscopic photograph of the intermediate preform after the first drawing step. The assembly of the microlens has a few errors compared to the design. Some of the errors are naturally introduced owing to the different patterns - square pixels in the design and hexagonal close-packed in the preform. Other errors, such as the horizontal line of NC21 in the lower left part of the preform, are introduced by misplacements of rods. Due to the large and irregular pattern, it requires long experience and patience to assemble the preform accurately.

After drawing the structure the first time, the pattern will be fixed, the only error that can be introduced in a later stage, is deformation of the lens due to internal stress, or inhomogeneous heating of the preform in the furnace of the fibre draw tower.

In the second fabrication step, the intermediate preforms were assembled to a hexagonal array. The air gaps between the circular rods are filled with NC21 rods with a smaller diameter. The new array contains a regular hexagonal pattern of around 350 lenses. This new intermediate preform is again scaled down in the fibre draw tower to rods of various diameters by changing the draw speed during the process.

In the last step the rods containing the lens arrays, are assembled to a second intermediate preform. Due to the various diameters of the rods, the structure could not be assembled in a regular pattern. In this last step, the rods were deformed strongly, which caused the lenses to distort particularly at the edges of the array.

6.1.1 Theoretical Characterisation

The treatment of this microlens in the paraxial domain with the scalar equations for GRIN lenses has only limited informative value. Here the refractive index is relatively

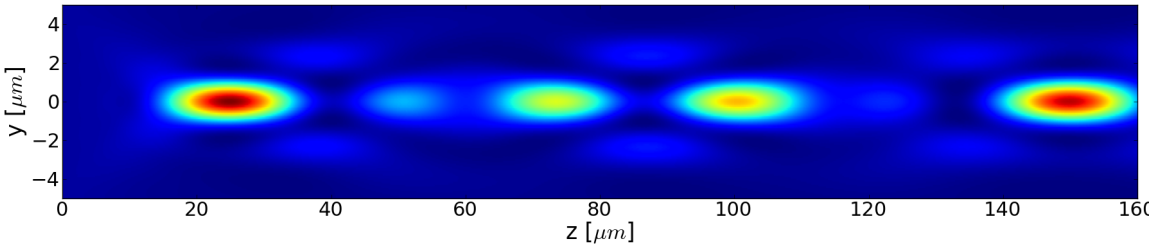

(a) Ideal lens

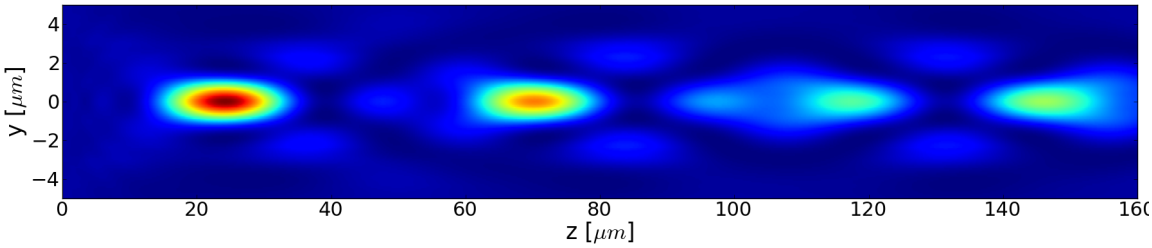

(b) Structured lens

Figure 6.2: Cross section of the intensity in the yz-plane for the propagation inside the microlenses. The field distribution of the ideal lens (a) shows a relatively good periodicity up to $z \approx 150\,\mu m$. In the structured lens (b), the intensity profile is roughly similar to the ideal case, however the intensity drops due to scattering loss. Up to the first quarter pitch the error is very small.

high and the radius of the lens with $r = 5\,\mu m$ is very small. However the equations should get an approximate value for the pitch length. The expected pitch length for this lens lens is $p = 89\,\mu m$ which was calculated from equations 4.9 and 4.11.

In order to get a reliable theoretical characterisation, the light propagation through the spherical NSGRIN lens was modeled with the FDTD algorithm and then compared to the performance of an ideal GRIN lens with the target refractive index profile. In the simulations, the diameter was chosen to be $10\,\mu m$ with an illuminating wavelength $\lambda = 1\,\mu m$. They were performed with a plane wave illumination, a spatial step size of 40nm and a temporal step size of $6.67{\cdot}10^{-17}\,s$. The computational space is terminated by the perfectly matched layer boundary condition [117]. The simulations were run at the University of Warsaw and analysed at Heriot-Watt University.

Figures 6.2a and 6.2b show the cross section of the yz-plane of the light intensity distribution inside the ideal GRIN microlens and the NSGIN microlens, respectively. In both cases, the lenses are illuminated by a plane wave at $z = 0$. The focus in the first quarter pitch at $z \approx 25\,\mu m$ is nearly identical for the two lenses. The position of the highest intensity is very close: $z = 24.96\,\mu m$ for the ideal lens and $z = 24.24\,\mu m$ for the structured lens. It is slightly higher than the values from the GRIN equations which is probably a result of the approximations of the paraxial calculations which loose their validity in this regime. At distances further away however, the field of the structured lens differs from the desired distribution. In both lenses, the intensity

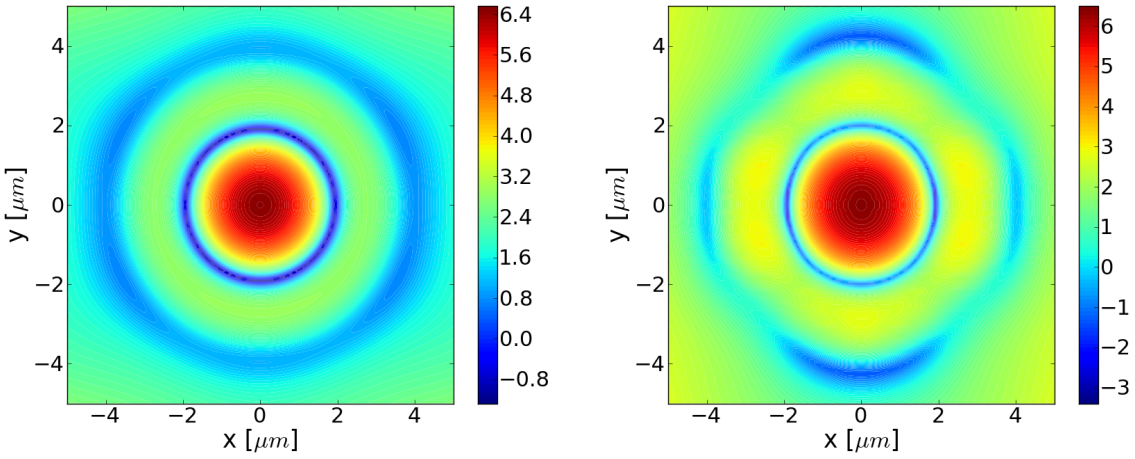

(a) Ideal lens

(b) Structured lens

Figure 6.3: Intensity distribution in the focal plane at $z = 25\,\mu m$. Due to the small difference between the ideal lens (a) and the structured lens (b) the diagrams are plotted in a logarithmic intensity scale. As expected the ideal lens is perfectly symmetric, the structured lens shows some intensity variations in the sidelobes.

oscillates and has six maxima between $z = 0$ and $z = 150\,\mu m$ with strongly varying peak intensity. The position of the middle two peaks differs between the two lenses but the trend is similar. The intensity of the structured lens at the last maximum at $150\,\mu m$ is much lower than in the ideal lens which is due to scattering losses. To really understand the behaviour of the light propagation in such small GRIN lenses, more simulations will have to be conducted in the future. Especially the strongly varying peak intensities will have to be understood.

These simulations show that a micro structured gradient index lens can guide light similarly to a real GRIN rod lens. As already concluded in chapter 5 for structures with feature sizes of $\lambda/5$ in the microwave regime, the design of the pattern in this regime is critical for the performance. This implies that NSGRIN structures with such large features, have a low robustness to errors in the assembly.

Up to the first half pitch length the two lenses show a very good agreement of their internal field. The lenses, which are used to focus or collimate light, would have a thickness of less than a quarter pitch which is in this case 25µm or less. At short distances up to a half pitch length, the simulations in both cases are still very close. Such thin elements are very difficult to handle and also to polish, therefore a smaller refractive index contrast will have to be chosen to achieve a longer pitch length.

Figure 6.3a and 6.3b show a colour plot with a logarithmic scale of the intensity in first focal plane at $z = 25\,\mu m$. On a linear colour scale, the difference between the fields would not be visible. The focus area is nearly identical, only in the sidelobes the field of the nanostructurd lens has some asymmetric features. These asymmetries are at a very low intensity, so for most applications they can be neglected. Figure 6.4 shows the intensity cross sections at the first focus of the ideal lens, as well as the x

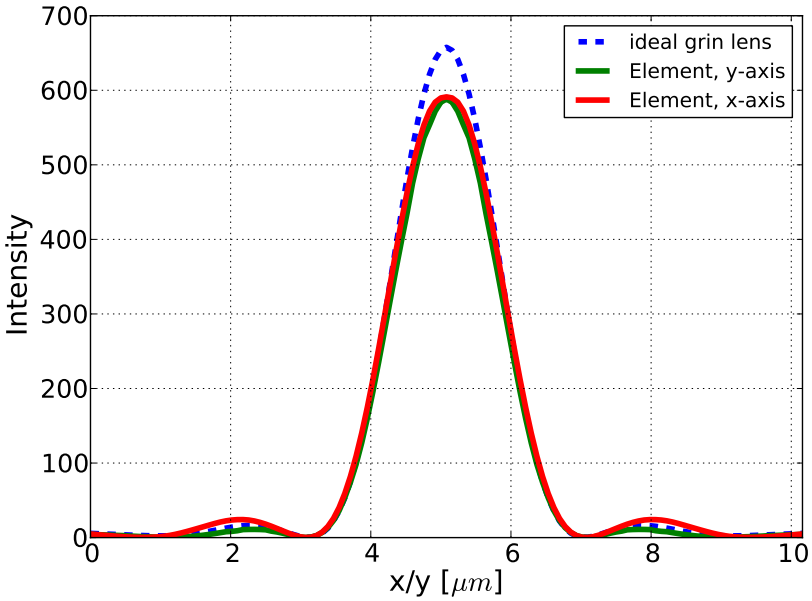

Figure 6.4: Cross section of the intensity through the first focus inside the GRIN lens. The intensity of the ideal lens (blue dashed line) is about 10% higher than in the structured lens (solid lines). Both, the x and y cross section of the structured lens are nearly identical.

and the y cross section of the structured lens. The peak intensity of the NSGRIN lens at this point is around 10% lower compared to the ideal case, the spot width however matches well. A small difference in the first sidelobe is visible but it is also in the order of a few percent.

These simulations agree with the findings from the microwave lenses, that nanostructured lenses with a pixel size of $\lambda/5$ behave similar to real GRIN materials but the performance can be rather poor and is strongly dependent on the quality of the design and the precision of the assembly.

6.1.2 Experimental Characterisation

Figure 6.5 shows phase contrast pictures of the final lens array. The parts of the structure that were used for the analysis are marked by the numbers 1, 2 and 3. The picture in figure 6.5a was taken with an $\times 5$ microscope objective, for figure 6.5b, a $\times 50$ objective was used and for figure 6.5c, a $\times 100$ objective, respectively. The diameters of the lenses range from 20 µm in region 1 down to less than 6 µm in region 2 and smaller.

The distortion of the lens arrays is clearly visible in figure 6.5a. The individual arrays should ideally be circular, but due to the different diameters of the rods, the shapes were deformed strongly. Each array consists of about 350 lenses which can be seen as white spots inside the different fields in figure 6.5a.

A magnified picture of field 2 is shown in figure 6.5b. During the last drawing

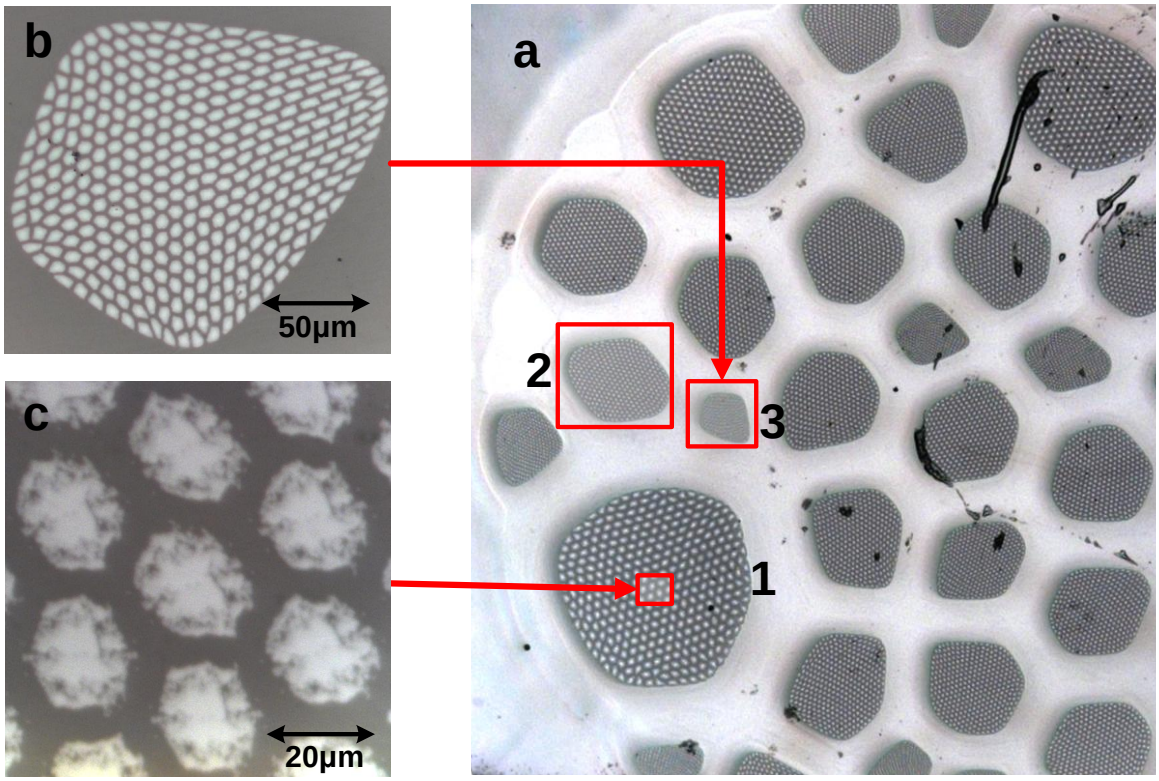

Figure 6.5: Phase contrast image of the final array of the microlenses: (a) shows the final structure containing lens arrays of various sizes; Area 1, 2 and 3 will be used for more detailed analysis. (b) shows area 3 in a higher magnification. The individual lenses of the array are visible. (c) shows a small part of area 1 with the largest lenses. Here the lens structure is recognizable.

process, the deformation is introduced due to internal stress and surface tensions at the boundaries between the rods. Therefore, lenses on the edge of an array are distorted the most. In the center of the arrays, some lenses are still in the intended shape. The pattern of the rods is not visible in this magnification.

The magnified picture of region 1, displayed in figure 6.5c, shows a small section of the center where the distortion is the least pronounced. The larger features of the lens structure can be identified, the individual rods however are too small to be resolved with the optical microscope.

The phase contrast pictures, taken with the ×100 microscope objective, are used to investigate the phase profile of the lenses depending on the diameter and feature size. Figures 6.6a - 6.6c show a cross section of the phase contrast data through the centre of one selected lens from area 1, 2 and 3, respectively. To obtain the cross sections, one lens was extracted from each of the three different arrays with lens diameters d=20 µm, d=10 µm and d=6 µm, respectively. Thus, the feature sizes range from 0.4 µm down to 0.14 µm.

The feature size of the largest lens is in the order of the wavelength of visible light and will act as a diffractive element rather than an effective medium. In figure 6.6a the distribution of the rods is clearly visible. The single rods however, cannot be resolved

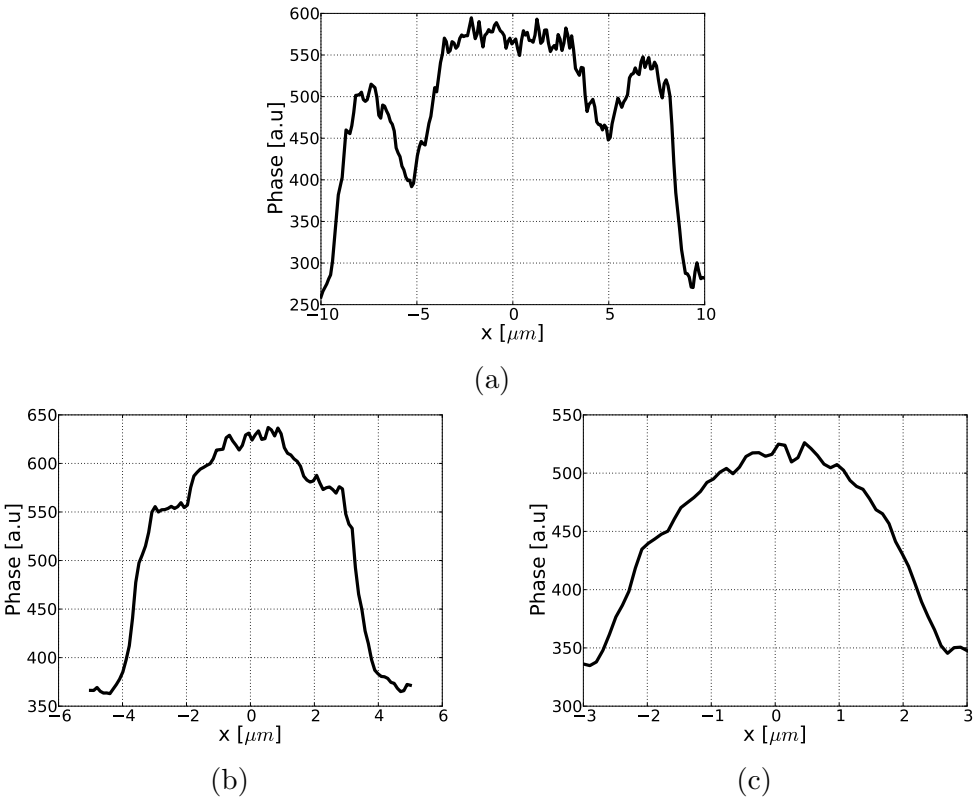

Figure 6.6: Cross sections of the phase contrast images of one lens from region 1 (a), region 2 (b) and region 3 (c). The smallest lens, displayed in (c), shows the best agreement with the phase profile that would be expected for an ideal GRIN lens whereas in the signal of the largest lens (a) the features of the structure are still present.

because the resolution of the microscope objective is not high enough to distinguish features of 0.4 µm. In the design there is a ring around four pixels away from the lens edge where the concentration of the lower index glass NC21 increases. This feature is clearly visible in the phase cross section of the largest lens as a local minimum of the signal at $x \approx \pm 5\,\mu\text{m}$. With a better design the phase profile could have been improved, however for such large feature sizes, the profile will never be perfect.

The lenses from field 2 have a diameter of $d \approx 10\,\mu\text{m}$ which is about half the size compared to the first case. The feature sizes are in the order of $\lambda/5$, so the ratio of wavelength to features is similar to the configuration in the microwave experiments. The phase cross section looks more parabolic, the drop from the largest lens appears now only as a flattening of the signal in this area at $x \approx \pm 2.5$.

As expected, the lens with the smallest diameter has a phase profile that matches the desired parabolic shape the best. Here, the feature size is only 0.1 µm which is well within the limits of the effective medium theory.

The comparison of these three lenses confirms the earlier made assumptions that the NSGRIN lenses become more robust against errors with decreasing feature sizes and the effective medium theory represents the physical effects more accurately.

These measurements however need to be looked at carefully, as the resolution of the microscope is in the order of 0.5-1 µm. Therefore the smallest lens can only be resolved by maximum 10 by 10 distinguishable pixels. This is a much lower resolution than the spatial frequency of the index changes which makes it impossible to resolve the actual structure. Nanostructured GRIN materials can never be resolved with light in the optical window, because the concept of NSGRIN lenses is based on the fact, that the light is only affected by the average of the refractive index at each point. The simulations show that the light, after propagating through the microlens, has a smooth distributions with no high spatial frequencies. The only way to get definite experimental confirmation of the simulations is to check the propagation properties of the transmitted field by imaging the intensity profile at several distances behind the lens. Due to the small size of these lenses such experiments could not be conducted.

In figure 6.7, the measured phase profile of the lenses is compared with the effective index structure, calculated using three different radii for the neighbourhood. The similarities of the diagrams show a correlation between feature size and radius of the effective index calculations. The general rule seems to be, the larger the features of a structure, the fewer pixels ought to be used for the effective medium approximation. A very simplified explanation could be that the area over which the effective index is calculated, should always be in the order of one wavelength. Therefore, for lenses with large features, the number of pixels included in the calculations is smaller than for lenses with very small feature sizes.

The phase profile of the largest lens with diameter $d \approx 20\,\mu\text{m}$ (fig. 6.7b) resembles the effective index distribution calculated with a neighbourhood of 3 pixels (fig. 6.7a). The areas, where pixels of the same refractive index or material accumulate, are clearly visible in both phase and effective index. Particularly the isolated drop of the phase at position $(x, y) = (6\,\mu\text{m}, 6\,\mu\text{m})$ and the associated symmetric points is present in the effective index profile.

Figure 6.7d displays the phase profile of a lens with diameter $d \approx 10\,\mu\text{m}$. Some features of the pattern are still visible, very high spatial frequencies however appear smoothed out. This lens behaves better like a nanostructured GRIN medium and has the best resemblance with the effective medium in figure 6.7c which was calculated taking a neighbourhood with 5 pixels radius into account.

The effects most similar to an ideal GRIN microlens are observed from the smallest microlens with diameter $d \approx 5\mu\text{m}$. Comparing it to the effective refractive index with a neighborhood of 6 pixels as radius, shows very good agreement. Even though the lens has an elliptical shape, which is due to the distortions from the last drawing step, the qualitative similarities between the effective index profile in figure 6.7e and the phase contrast image in figure 6.7f are apparent.

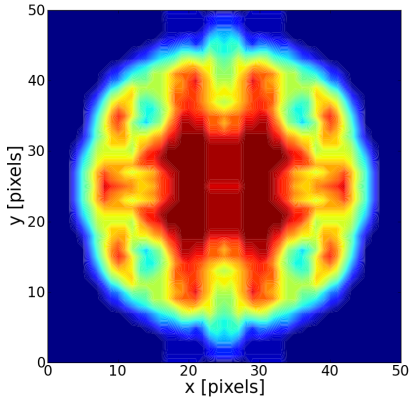

(a) Effective index with r=3

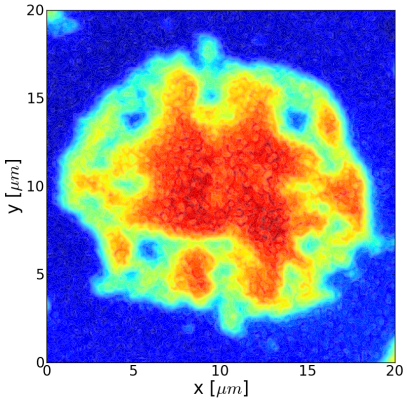

(b) Phase contrast picture from array 1

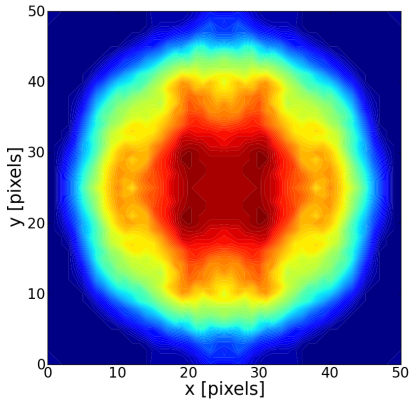

(c) Effective index with r=5

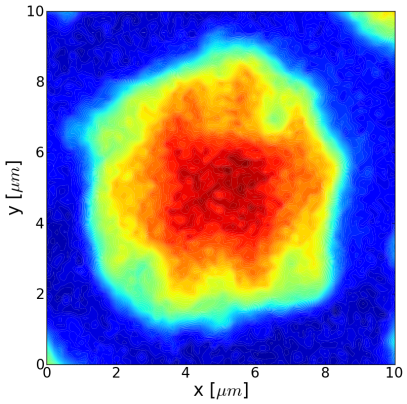

(d) Phase contrast picture from array 2

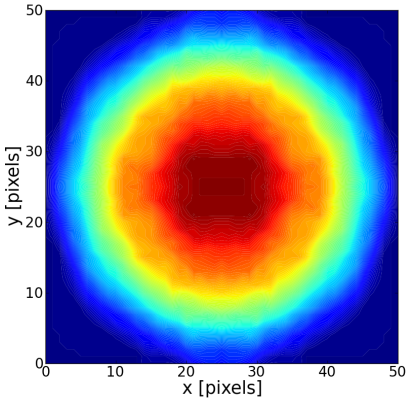

(e) Effective index with r=6

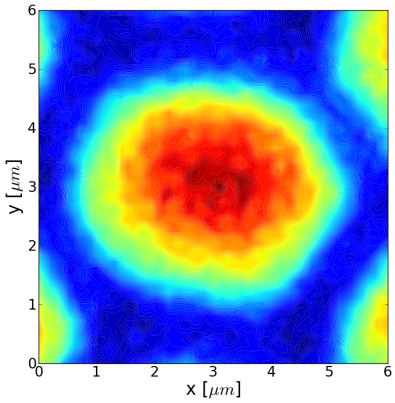

(f) Phase contrast picture from array 3

Figure 6.7: Comparison of the effective index distribution calculated for neighbourhoods with different radii with the phase contrast images of three lenses. The effective index with the smallest neighbourhood (a) matches the largest lens best. The lens with 10 µm shows the best agreement for an averaging radius of 5 pixels and the smallest lens agrees best with the largest averaging radius of 6 pixels.

This experiment was conducted to show the validity of the approximation only qualitatively. It gives an indication of the validity of the effective medium theory introduced before. It also shows that the performance and accuracy of effective medium structures increase with the decrease of the feature sizes. The exact correlation between the pixels sizes and the accuracy of the effective index approximation still has to be understood better. A more comprehensive and detailed analysis will have to be carried out to give more detailed information and understanding on this issue. Knowing the connection will give a useful measure to judge the required feature size and thus complexity of the pattern for optical elements with certain demands. From a practical point of view, the number of rods to form a structure should be minimised due to the limitation of being able to stack them accurately to a desired pattern. Another limitation of the preform diameter is the size of the furnace in the fibre draw tower.

6.2 Elliptical NSGRIN Microlens

Edge emitting diode lasers have an elliptical beam shape because of their rectangular light emitting surface. The coupling of these beams into an optical fibre is problematic and very lossy when using a standard spherical lens. Owing to the different numerical apertures (NA) of the two main axes, the light cannot be focused into a circular spot. One solution to this problem is to use two cylindrical lenses with different focal lengths. This is however very difficult to align and cannot be used in compact optical systems. By employing elliptical microlenses with the correct parameters, it is possible to couple light directly from the laser into optical fibres or other waveguides. Elliptical microlenses have different NAs along their two axes. A lens that has an identical NA in the two main axes as the laser, will focus the emitted wave into a single circular spot.

6.2.1 Design and Fabrication

An elliptical nanostructured microlens was designed, fabricated and characterised in order to demonstrate the ability of the stack-and-draw technology to fabricate non-spherical microlenses accurately.

The design algorithm was run by J. Nowosielski using the simulated annealing algorithm with the effective medium theory as described in chapter 4. The pattern was designed for a glass pair with a relatively low refractive index contrast: NC25 ($n_D = 1.5295 \pm 2 \cdot 10^{-4}$) and NC21A ($n_D = 1.5275 \pm 2 \cdot 10^{-4}$) [97]. This index contrast ensures that the pitch length of this lens is long enough so that errors in the thickness do not have a very strong effect. Furthermore, the effective medium theory is more accurate for low refractive index contrasts, because the correction term in equation 4.6 is smaller compared to the spherical lens described in section 5.1.

The pattern of the elliptical lens consists of 100×100 pixels with a final diameter of 16 µm. The target profile of the refractive index is expressed as a function of the quarter pitch length of the x-axis and of the y-axis respectively. Due to the mixing approach, the refractive index can only take values between the refractive index of the lower index glass and the higher index glass. The equation of the lens is then

$$n(x,y) = \max\left\{ n_{max} \cdot \left[1 - 0.5 \left(\frac{\pi x}{2 \cdot p^x_{1/4}} \right)^2 - 0.5 \left(\frac{\pi y}{2 \cdot p^y_{1/4}} \right)^2 \right], n_{min} \right\}. \qquad (6.1)$$

n_{max} and n_{min} are the indices of the two glasses; $p^x_{1/4} = 246 \pm 12\,\mu\text{m}$ and $p^y_{1/4} = 518 \pm 116$ are the quarter pitch length on the x-axis and on the y-axis, respectively. The error in y is very large because the difference between the maximum index in the centre and the minimum index at the edge is much smaller compared to the fast axis,

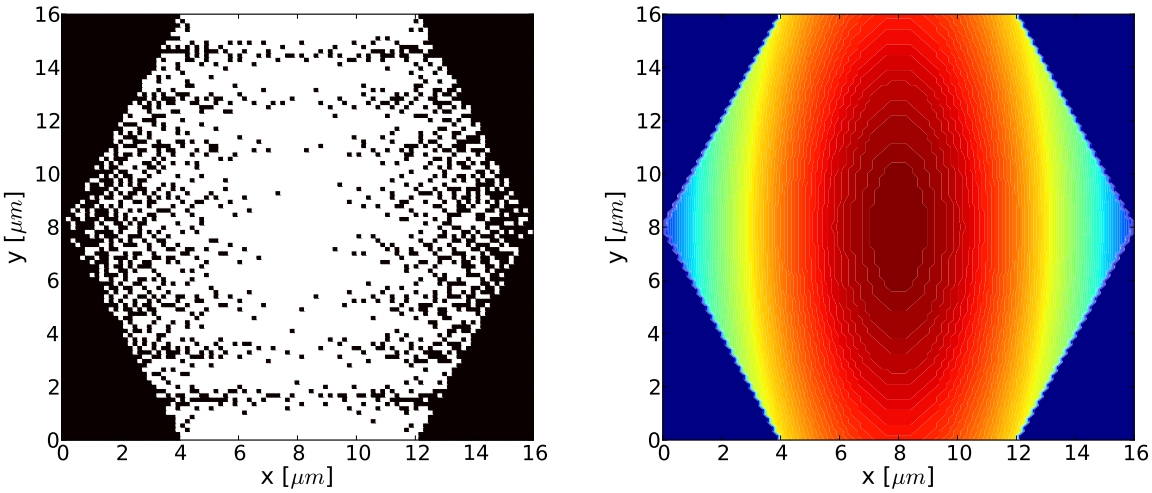

(a) (b)

Figure 6.8: (a): The design of the elliptical microlens. Black pixels represent the lower index glass NC21A and white pixels represent the higher index glass NC25. (b): The target refractive index profile with a smooth distribution with $n = 1.5275$ as minimum at the edge and $n = 1.5295$ in the center

so the error of the refractive index of the two glasses becomes more important.

Figure 6.8b shows the refractive index profile of the ideal GRIN lens. The design to match this profile is displayed in figure 6.8a, where the black pixels represent the lower index glass NC21A and the white pixels represent NC25, respectively. The pattern shows some horizontal lines with a higher density of NC21A which is induced by the way how the effective index was calculated in the design algorithm. Like in the designs of the spherical microlens and the spherical microwave lens, a square neighbourhood was used to calculate the effective index profile.

Additionally, there is a higher concentration of the high index glass NC25 at the top and bottom edge of the lens, which is caused by assuming that the material around the lens is NC21A. The required average index at the boundary is higher than the refractive index of NC21A. At these edges, in order to achieve this higher average index, the concentration of the higher index glass NC25 must be denser than expected. In combination with a square neighbourhood for the effective index calculations, this leads to a periodical concentration of the two glasses in y direction. Owing to the fixed boundaries, which are determined by the surrounding material, the oscillations of the material densities are the strongest near the edges. This effect does not appear along the other edges of the hexagon because the design was performed for the whole 16 µm × 16µm square and the target index at the boundaries in y direction is closer to the refractive index of the material in the vicinity of the lens.

These issues could be improved at a later stage of the project by using a circular neighbourhood, and by only using pixels inside the lens pattern without making any assumptions about the surrounding.

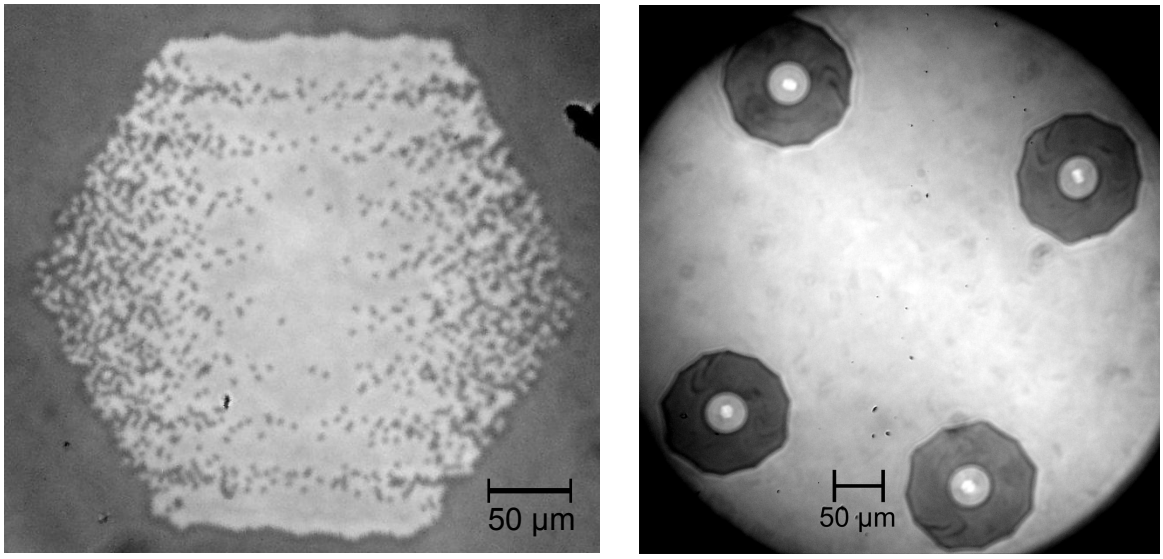

(a) (b)

Figure 6.9: Microscopic pictures of the elliptical microlens: A standard optical microscope picture of the intermediate preform (a) and a phase contrast picture of the final 2×2 array (b)

The microlens was stacked and fabricated at ITME in Warsaw. Figure 6.9a shows a picture of the post preform after the second drawing step. At this stage, the structure has a diameter of around 300 µm and a feature size of 3 µm. This structure has not yet the properties of an effective medium as the feature sizes are still several times larger than the wavelength in the optical spectrum.

Figure 6.9b shows a phase contrast image of the final microlens array. In the last drawing step, four rods of the lens structure were assembled into a 2×2 array by incorporating them in a preform of NC21A rods.

The edges of each intermediate preform are clearly visible as concentric rings in the picture. In the third drawing step a different glass composition was used as filling material. Even though, the rods also consist of NC21A the properties are slightly different because the glass that was used comes from a different fabrication run. Small variations in the composition causes a refractive index which differs a little bit from the one in the lens. It therefore causes a different phase delay relative to the other areas, which has a different colour in the phase contrast picture. The elliptical white spots in the centre of the gray circle, which is enclosed by the dark rings, are the microlenses.

In this sample, the main axes of all four lenses are oriented in different angles. The main objective of this structure was to demonstrate the fabrication capabilities and to characterise the lenses to give experimental evidence of the effective medium theory. A precise placement and orientation of the individual lenses was therefore not required.

The diameter of the lenses is 16 µm with a spacing of around 250 µm between

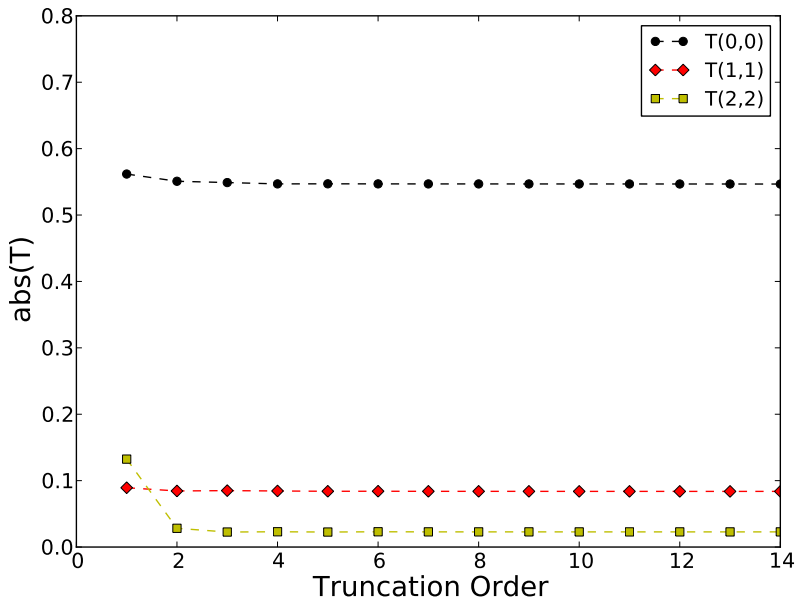

Figure 6.10: The convergence of the magnitude of the (0,0), (1,1) and (2,2) transmission order when solving the elliptical lens structure with the FMM

each other. In the final production step, the rods were cut to disks and polished to a thickness of 120 µm. With equation 4.12 the expected focal lengths can then be calculated. For the fast axis with $n_0 = 1.5292$ and $n_R = 1.528$ the focal length is f=133.3 ± 13.5 µm.

6.2.2 Theoretical characterisation using the Fourier modal method

The Fourier modal method is a very efficient approach to solve the NSGRIN lenses. For low refractive index contrasts and very small feature sizes, i.e. in the regime of the effective medium theory, the transmission coefficients converge extremely fast to a constant value. Figure 6.10 shows the convergence of the absolute value of three different transmission coefficients, when solving the lens displayed in figure 6.8a. The simulations were performed for $\lambda = 633$ nm with angles of incidence $\theta = 0$ and $\phi = 0$. The grating has a size of $d_x = d_y = 25$ µm and consists of the lens structure in the center with a 5 µm frame of NC21A around it. Unlike in the case of the elliptical microwave lens (Fig. 3.6b) the result is already stable for a truncation rank of ±5 orders which only takes a few seconds computation time. This gives the FMM a great advantage over other rigorous algorithms such as FDTD.

In figure 6.11 the change of the field when increasing the truncation rank is calculated by comparing the field at the back surface of the lens. Foe each truncation rank, the field was calculated in a grid of 100×100 pixels. The difference of two truncation

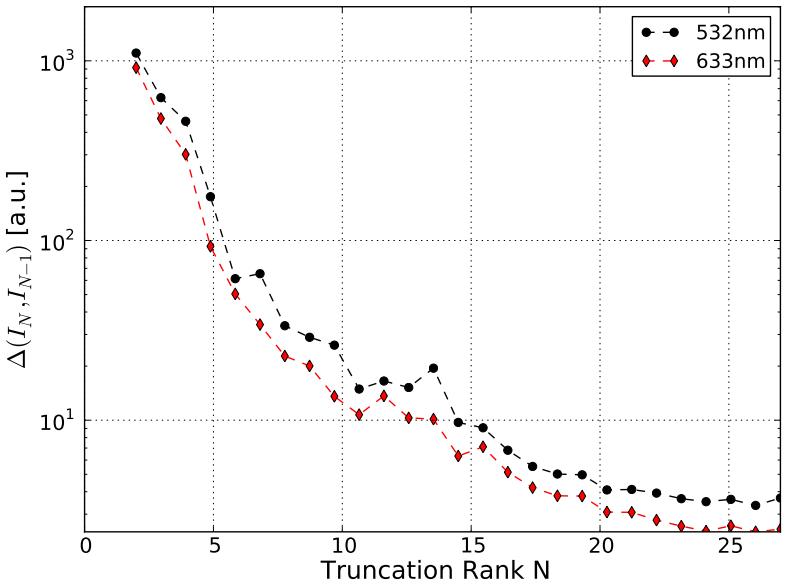

Figure 6.11: The convergence of the field for an increasing truncation order of the FMM simulations

ranks n and n-1 is then calculated by

$$\Delta(n) = \sum_{p,q=1}^{100} \left| I^n(p,q) - I^{n-1}(p,q) \right| \tag{6.2}$$

where p and q denote the coordinate of the pixels. In the case of this spherical microlens, the field distribution converges very fast despite the large number of pixels. This can be explained with the effective index which is a simple low contrast elliptical profile. A higher spatial resolution is not necessary because the light matter interaction takes place on a larger length scale.

To simulate this elliptical lens with the FDTD algorithm, the memory requirements of the simulations exceed 15 GB and the calculation would take up to several days.

The elliptical microlens was analysed using the Fourier modal method for crossed gratings. In the FMM simulations, the periodic boundary conditions play a very important role for the result. If the unit cell of the simulations is chosen as displayed in figure 6.8a, the transmitted field of the lens will be very different from that of an isolated lens. Due to the periodicity of the discrete Fourier transform representation of the electromagnetic field, the solution represents an infinite array of the lens where adjacent unit cells introduce cross talk and change the interaction properties of the lens with the incident light. By adding a frame with a constant refractive index of NC21A, the simulation represent the lens structure more realistically.

Figure 6.12 shows the phase and the intensity of the electric field at the back surface of the structured lens (a, b) and of the target lens (c, d), respectively. To simulate the realistic case of an isolated lens, a 5 µm frame with the same index as

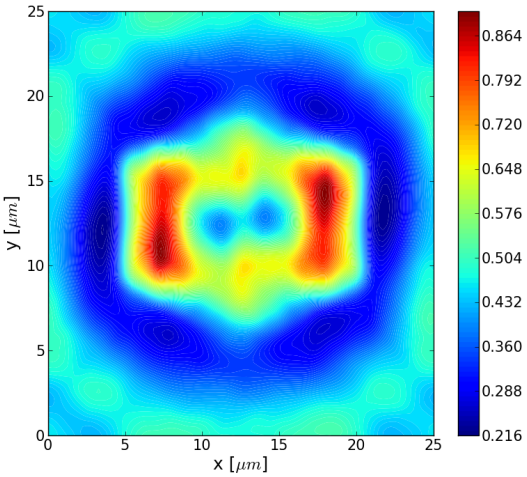

(a) Intensity profile of the structured lens

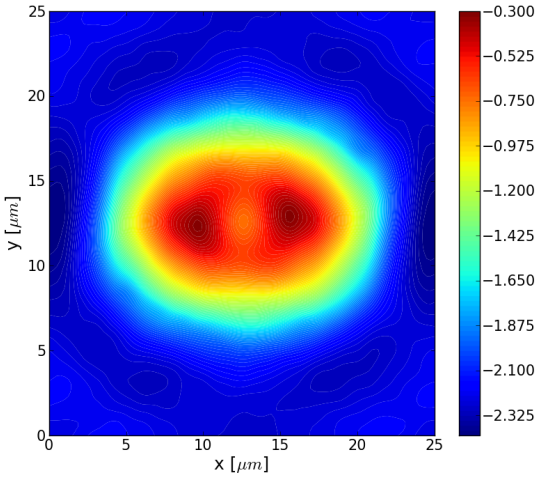

(b) Phase profile of the structured lens

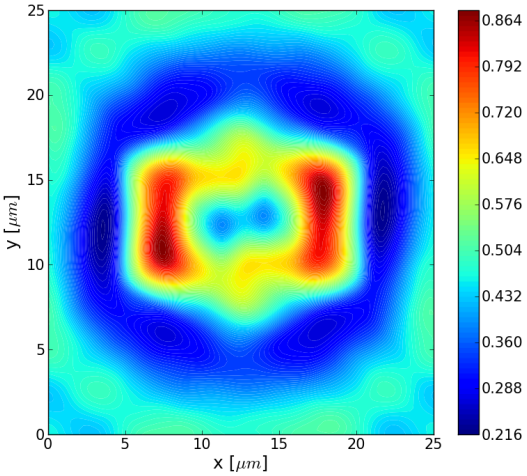

(c) Intensity profile of the target lens

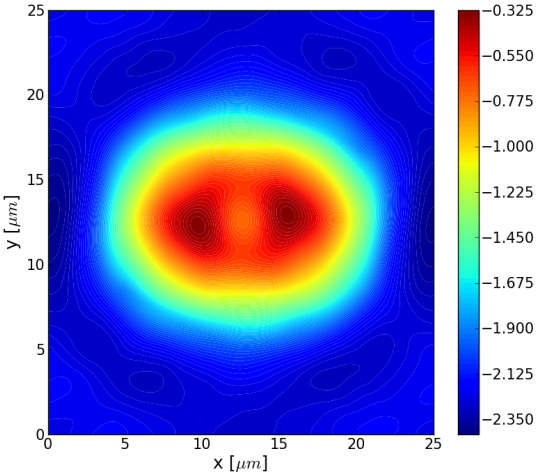

(d) Phase profile of the target lens

Figure 6.12: The phase and intensity of the structured elliptical microlens (a,b) and of the target GRIN lens (c,d). The field profile of the xy-plane at $z = 0$ was obtained by the FMM. A 5 µm padding with $n_{low} = 1.417$ was added on each side to suppress effects induced by the periodic boundary conditions

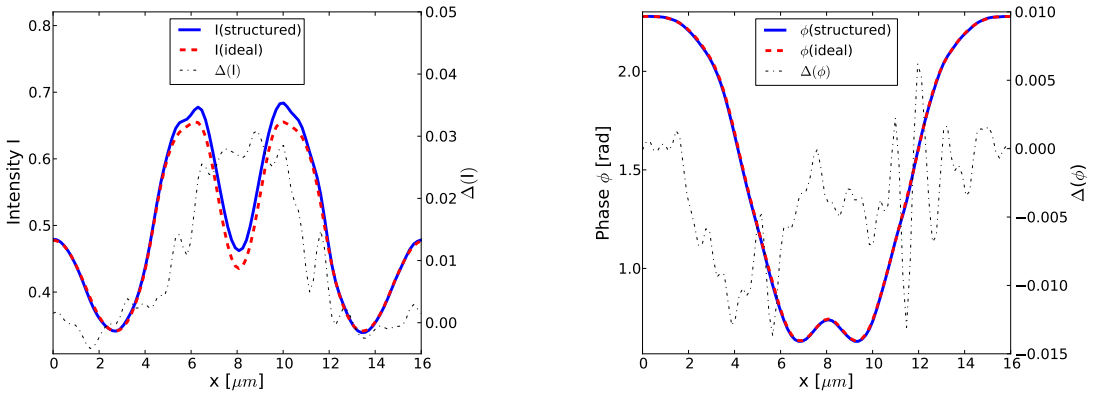

(a) (b)

Figure 6.13: The cross section of the intensity (a) and phase (b) at the back surface of the microlens. The structured lens (blue solid line) has a nearly identical result as the target lens (red dashed line), the difference is marked by the black dashed line (right scale)

the lower index glass was added around the lens structure. The field further away than 5 µm is not influenced by the lens and does not have to be taken into account in the simulations. For the calculations, a a truncation rank of ±25 and a plane wave illumination in normal incidence with wavelength $\lambda = 532\,\text{nm}$ were chosen. Despite having a very fast convergence of the transmission orders, the phase as well as the intensity have some asymmetric features which diminish only very slowly with an increasing truncation rank. The asymmetry for the truncation rank of 25 is very small and hardly affects the propagation properties of the transmitted field. Both elements have a nearly identical field profiles. The slight asymmetry occurs in both cases which indicates, that this is probably a numerically induced issue as the target index profile is perfectly symmetric.

In order to compare the performance of the nano structured lens to its associated ideal GRIN lens, the light propagation through the target GRIN lens has also been calculated, using the same parameters as for the structured lens. Figure 6.13 shows a cross section of the field in the xy-plane along the x-axis at $z = 0$ behind the lens. The intensity of the nanostructured and the target lens are displayed in figure 6.13a, the phase is displayed in figure 6.13b, respectively. The cross section of the complex field of the two lenses is very similar. The phase cross section is nearly identical and differs by less than 2%. This result shows, that the effective medium theory is a very good approximation for nano structured GRIN elements in this regime. The intensity difference between the structured lens and the target shows a higher discrepancy than the phase, especially in the central part of the lens. The difference is still very small and only confined to some areas in the field profile which is apparent when comparing figures 6.12b and 6.12d.

To calculate the propagation of the transmitted light, the ASPW algorithm is used

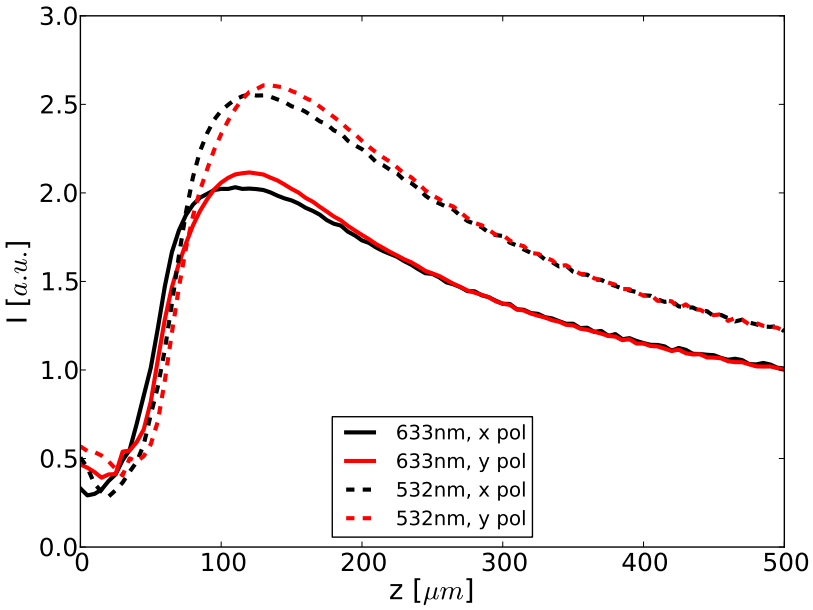

Figure 6.14: The intensity on the optical axis of the structured lens as a function of the distance. Due to the anisotropic material distribution, x polarised light has a slightly different behaviour than y polarised light. The green light ($\lambda = 532\,\text{nm}$) has a higher peak and longer focal length than the red light ($\lambda = 633\,\text{nm}$). In these calculations the material dispersion was not taken into account.

in the same way as for the microwave lenses. The field at the back surface of the lens is calculated with the FMM. In the area of 25 µm × 25 µm the electric field is calculated from the transmission coefficients for 100 × 100 pixels. This field is then embedded in the centre of a larger matrix of 512 × 512 pixels. The overall size of the computational cell has then a size of $(128\mu\text{m})^2$ with the lens in the centre. The area around the lens is set to the field value of the point $(x, y) = (0, 0)$ from the FMM simulations. Owing to the padding used in the FMM, the field at this distance is undisturbed and can be assumed constant (see figure 6.12).

Figure 6.14 shows the intensity on the optical axis as function of z. The lens was simulated for $\lambda = 532\,\text{nm}$ and $\lambda = 633\,\text{nm}$. For both wavelengths, the x polarised light has a slightly longer focal length and higher peak intensity. In an ideal GRIN lens, the intensity profile should be polarisation invariant. However, in the case of this structured lens, where the material distribution has some regular patterns with lamellar features along the x axis, the effective index has polarisation sensitive properties. Furthermore the behaviour is wavelength sensitive, the focal length in the case of $\lambda = 532\,\text{nm}$ is longer than for 633 nm.

6.2.3 Experimental characterisation of the elliptical microlens

In this section, the simulated results are compared with experimental measurements from two different experiments. Due to the nearly identical properties of the structured and the target lens, the experimental data will only be compared to the simu-

lations of the structured lens.

The experimental characterisation of a microlens with a diameter of only 16 µm is very challenging. For a microlens with this diameter and a focal length of 133 µm, diffraction effects are expected to dominate the field behind the lens [118](page 181). Furthermore, optical microscopes have a limited resolution which is determined by the illuminating wavelength and the NA of the microscope objective. High magnification objectives generally have a resolution between 0.35 µm and 0.5 µm so the number of distinguishable points of the measurements is very limited.

The resolution limit Δ defines the shortest distance for that two points of an object can be distinguished. It is calculated from the NA and wavelength by

$$\Delta = \frac{\lambda}{\mathrm{NA}} \tag{6.3}$$

Therefore, the experimental data has to be treated with care as the measured intensity at a certain point represents a weighted integral of the field in its immediate vicinity. However, as the expected size of the focal spot is approximately 10 µm, the resolution is still high enough to obtain meaningful data. Additionally, if the lens would cause variations of the electromagnetic field with spatial frequencies faster than the resolution, these variations will only be present in the very near field.

Phase measurements using a Mach-Zehnder Interferometer

During a visit at the Friedrich-Alexander University in Erlangen, the elliptical NSGRIN lens was characterised with a Mach-Zehnder interferometer. The interferometer is operated in a single transmission mode using a Helium-Neon laser with wavelength $\lambda = 633\,\mathrm{nm}$, and it is calibrated to give quantitative phase values.

Figure 6.15 shows a schematic diagram of the optical setup. The intensity of the laser beam is modulated with the first polarisation plate, the second plate ensures a fixed orientation of the polarisation. In the first beamsplitter, the beam is split into a reference beam and an object beam. The microlens is placed in front of a microscope objective which magnifies the wavefront of the object beam behind the lens onto the CCD camera. Object beam and reference beam are interfered with each other in the second beamsplitter and recorded with a CCD camera. The exact position of the object beam can be altered with the mirror that is mounted on a piezo element. If the position of the two beams does not match exactly, the interference pattern is modulated strongly by interference rings induced by the relative shift. A comprehensive description of the setup is given in the Ph.D. thesis by H. Sickinger [119] and in reference [118].

Due to the small size of the microlenses, the highest available magnification had to be chosen which is a ×50 microscope objective with NA=0.8. Hence, the spatial

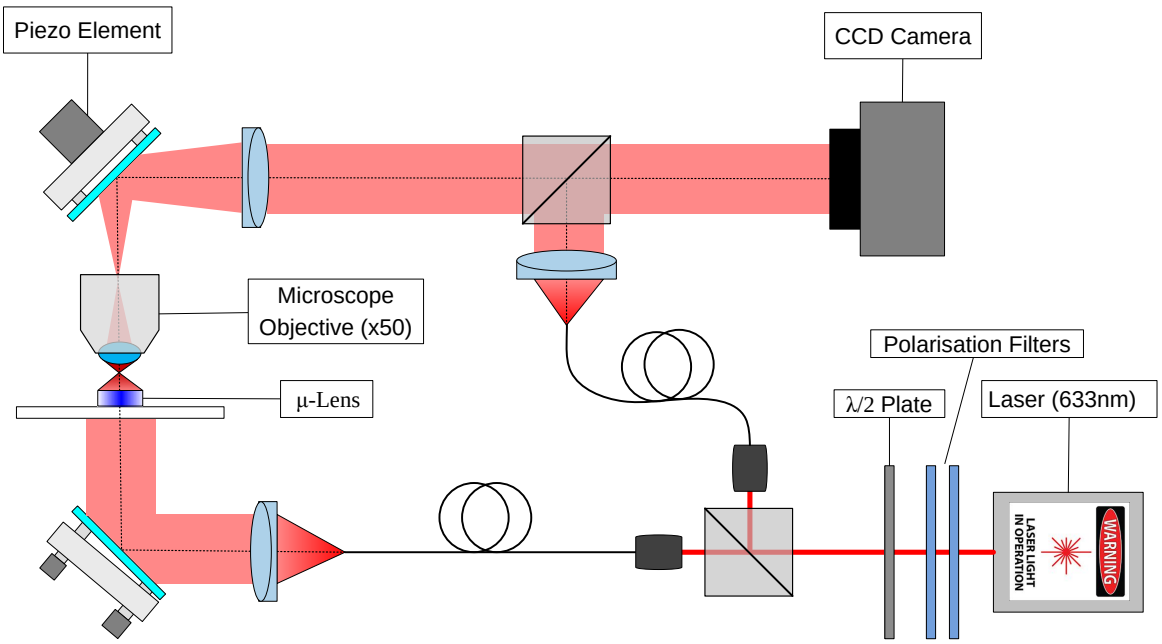

Figure 6.15: Setup of the Mach Zehnder interferometer with fibre illumination. The coherent beam is split in reference beam and object beam. Both beams are coupled in optical fibres. The object beam is used to illuminate the microlens which is then imaged onto the CCD camera by the microscope objective. The two beams are interfered with each other by the second beam splitter in front of the CCD camera. The mirror with the piezo element is used to accurately control the phase difference between the object beam and the reference beam.

resolution is $\Delta = \lambda/\mathrm{NA} = 0.4\,\mu\mathrm{m}$. The longer main axis of the lens measures $16\,\mu\mathrm{m}$, so the number of distinguishable points for the whole lens is about 40.

Several sources for errors and noise can be identified:

- The microscope objective and the collimating lenses are not anti-reflection coated which resulted in visible interference rings from the Fresnel reflections.
- The temporal signal stability of the laser is limited, therefore the phase changes slightly during one measurement. Furthermore, the signal stability is affected by air flux and vibrations. To reduce these effects, the interferometer is enclosed in a box and mounted on a floating optical bench. Before taking a measurement, the system takes a few minutes to stabilize after each adjustment on the interferometer or the sample.
- Dust in the system perturbs the wavefront and creates a speckle like pattern that varies on a scale of about $\leq 1\,\mu\mathrm{m}$ which is visible in the phase measurements
- The polarising beamsplitter has a selection rate of around 100:1 so the polarisations are slightly mixed which reduces the visibility of the phase contrast.

As apparent from Figure 6.16a, the orientation of each lens differs from the other ones. A rotation stage for the sample was not available, so the data had to be taken

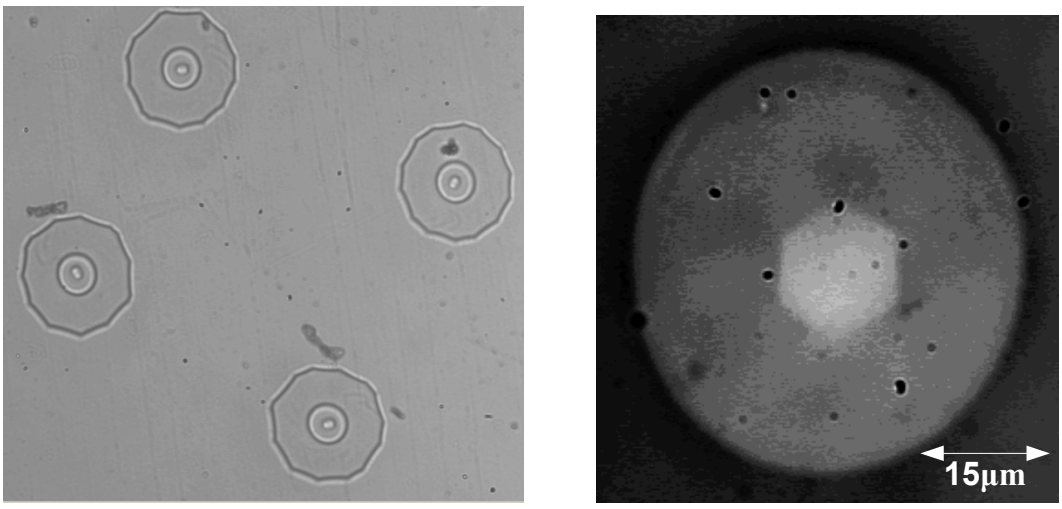

(a) (b)

Figure 6.16: Pictures of the elliptical microlens array taken with the Mach-Zehnder microscope by only using the object beam. (a): The array in x20 magnification. The orientation of the elliptical lens can be identified approximately. (b): For an exact measurement of the orientation angle of the lens a picture with ×50 magnification is taken. After increasing the contrast the hexagonal shape of the lens is clearly visible.

by aligning the sample with the translation stage only in x, y and z.

The rotation of the data is done numerically by applying a rotation matrix, in order to be able to compare the phase cross section of the two main axes. This is done with the following coordinate transform:

$$\begin{pmatrix} x' \\ y' \end{pmatrix} = \begin{bmatrix} \cos(\alpha) & -\sin(\alpha) \\ \sin(\alpha) & \cos(\alpha) \end{bmatrix} \begin{pmatrix} x \\ y \end{pmatrix} \quad , \tag{6.4}$$

where α is the rotation angle in anticlockwise direction. The value at point (x', y') is interpolated from the raw data with a rectangular bivariate spline.

The shape of the lens is clearly visible when using only the object beam to image the sample. In this configuration, the system works like a standard optical microscope. The rotation angle is obtained from the pictures in ×20 and ×50 magnification (Figures 6.16a and 6.16b). From the lower magnification, the approximate orientation of the ellipse can be found. In order to get the exact angle, the hexagonal image from the ×50 magnification is used. With this method, the angle can be found to an accuracy of about ±3°. It is however impossible to distinguish between lenses that are rotated by 180° because the pattern has a nearly perfect 180° rotational invariance. As this error in the orientation leads to almost identical results in the transmitted field, it can be neglected.

The individual measurements of one lens differ from each other by a mutually constant phase offset. To get all curves to one level, the mean phase value of each

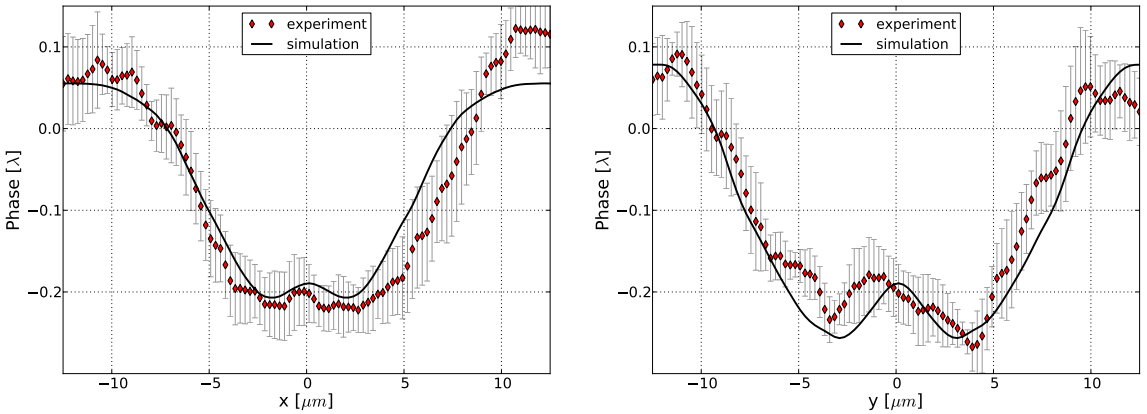

(a) (b)

Figure 6.17: Cross section of the phase along the two main axis of the elliptical microlens. The red diamonds show the experimental data with error bars which mark the standard deviation of the measurements. The black line shows the expected values from the FMM simulations. (a) shows the x cross section with the lower curvature, (b) shows the y cross section.

measurement is subtracted from every point of this measurement:

$$\phi'(x,y) = \phi(x,y) - <\phi> \tag{6.5}$$

Figures 6.17a and 6.17b show the cross section of the phase along the x-axis and along the y-axis, respectively. The experimental phase is the average of one measurement series with 14 measurements, the error bars mark the standard deviation at each point. The expected phase cross section from the FMM is marked by the solid line. In both directions the theoretical values are mostly within the error range. The phase of the experimental values is a bit steeper than the simulations, which could be due to small errors in the thickness of the polished lens or in the values of the refractive indices that were used in the simulations.

Intensity measurements

To measure the intensity distribution of the field at several distances behind the lens, a setup as sketched in figure 6.18 was used. The position and angle of the laser beam is controlled by the two adjustable mirrors. The microlens is mounted perpendicular to the laser beam on an xyz translation stage. A rotation stage for the lens mount was not available, so the angle of the lens with respect to the incident beam to the beam could only be aligned approximately. The imaging system consists of a $\times 40$ microscope objective mounted at 16 cm distance from the chip of the CCD camera. It is mounted on a computer controlled xy micrometer translation stage. In this configuration, the object plane has a fixed distance to the microscope objective. By moving the imaging system along the optical axis of the microlens, the object plane

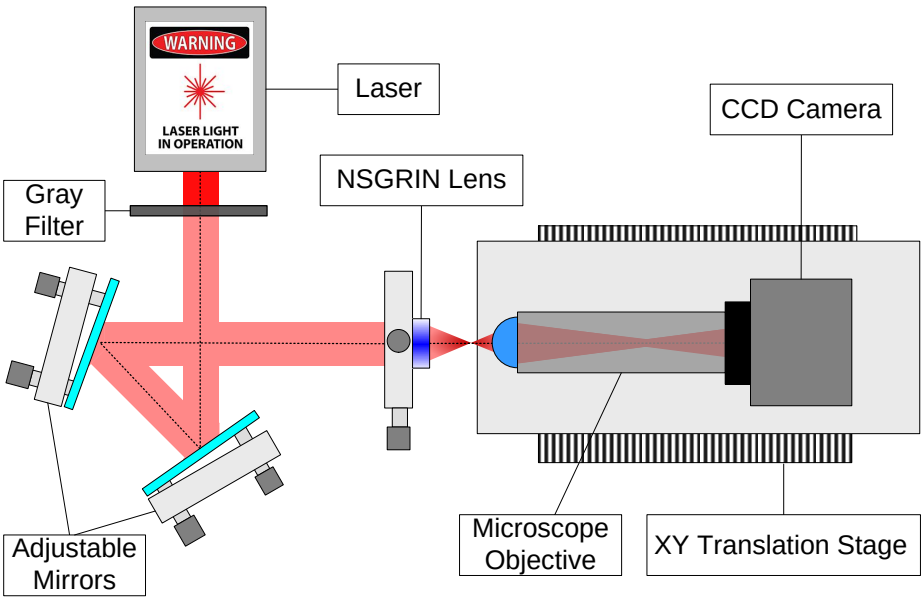

Figure 6.18: The optical setup for the intensity measurements: The laser beam is positioned with the two adjustable mirrors to be in line with the optical axis of the microlens. The imaging system, consisting of a microscope objective and a CCD camera, is mounted on an xy translation stage. By moving the imaging system along the optical axis, the field distribution at several planes behind the lens can be measured.

scans through the beam which is imaged onto the CCD chip.

The lenses were characterised for two different wavelengths: $\lambda = 633\,\mathrm{nm}$ using a Helium Neon laser and $\lambda = 532\,\mathrm{nm}$ using a frequency doubled YAG laser with diode pumping. Both lasers emit a collimated single mode beam with a diameter of around 1 mm. Due to the small size of the microlens, a beam expander is not required. If the lens is placed directly in the center of the beam, the intensity can be assumed constant, as it varies on a scale much larger than the lens diameter.

Each measurement starts by finding the position of the imaging system, where the surface of the microlens is imaged. In each series, the camera is moved away from the lens in steps of 5 µm from $z = 0$ to $z = 600\,\mu\mathrm{m}$. Owing to the high magnification, which is required to image the field behind the lens, even very small errors of the angle of incidence cause the spot to drift to one side of the CCD chip when moving the camera along the optical axis. To compensate for this in the analysis, each picture is shifted, so that the beam centre remains at a constant position for all distances.

The range of the intensities is very large when moving from the lens surface through the focus. In order to get a good contrast for each measurement, the electronic gain factor is changed at several distances. As the gain could only be varied manually by using a dial, the gain increase or decrease is calculated later numerically. By taking one measurement before changing the gain and a second one at the same distance after changing the gain, the new gain factor is evaluated by calculating the ratio of

the total intensity before and after changing the gain:

$$g_{new} = g_{old} \frac{\sum_{p=1}^{P} I_{new}(p)}{\sum_{p=1}^{P} I_{old}(p)} \tag{6.6}$$

where g_{old} is the gain factor before changing the gain, P is the total number of pixels of the CCD camera and $I(p)$ is the intensity signal at pixel p.

After adjusting the relative intensity and the position of the spot for all measurements, the pictures are rotated in the same way, as described for the phase measurements in equation 6.4. With this method, it is ensured that the main axes of all lenses are parallel to the x and the y axes. As the position $z = 0$ could not clearly be identified during the experiments, the field was measured from a plane around 20 µm - 50 µm inside the lens to make sure, not to start from somewhere behind the lens. During the data processing, the exact position of the lens could be found by comparing the intensity distribution on the optical axis. The field intensity on the optical axis has a steep increase between 20 µm and 100 µm behind the back surface of the lens. The offset in z direction can be found by matching the position of this intensity increase. After adjusting the orientation and offset for each of the four characterised lenses, the average intensity distribution and standard deviation can be calculated.

The false colour plots in figure 6.19 show the xz and yz cross sections of the measured intensity and the simulations for the illuminating wavelength $\lambda = 532\,\text{nm}$.

Figures 6.19a and 6.19b display the measured field which was measured in 5µm steps in z direction, figures 6.19c and 6.19d show the ASPW simulations with an extended computational space by assuming the extended field to be the same as at position $(x, y) = (0, 0)$ of the FMM simulations as shown in figure 6.20a.

At distances smaller than 150 µm, the measured intensity profile shows good agreement with the simulations. The different effect of the two main axes is clearly visible in the near field. In the region, both axes have a similar profile to the elliptical microwave lens (fig. 5.12). At distances larger than 150 µm however, strong interference patterns appear in the experimental data. At $z = (250 \pm 50)\,\mu\text{m}$, there is a very defined drop of the intensity around the optical axis, which reaches a very low value. In both experimental cross sections, an interference pattern from outside the lens is modulating the transmitted field of the lens. At the point of the intensity drop two diffraction orders can be identified that intersect at this point and cause destructive interference.

When looking at the phase contrast picture of the lens array (Fig. 6.9b) it is apparent that the filling rods in the second last drawing step induce a different phase delay which is due to a slightly different composition of the glass as explained in the introduction. The interference pattern of the experimental data is probably caused by diffraction at this boundary. The diameter of the inner radius of this ring is

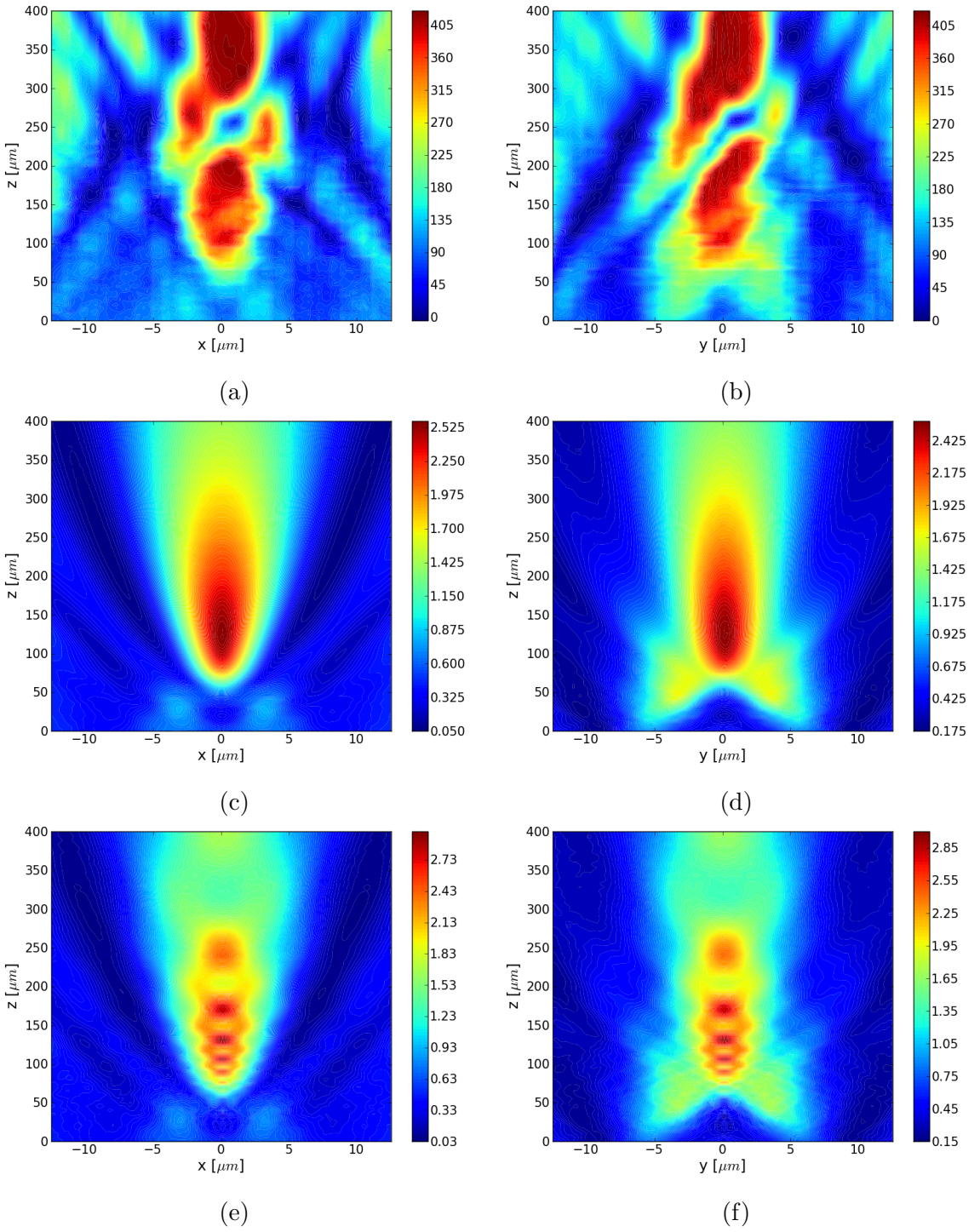

Figure 6.19: Intensity cross sections in the xz plane and yz plane of the measurements (a),(b), the simulations in the ideal case (c), (d) and when introducing a phase offset outside a circle with 50 µm around the lens (e), (f). The lens is illuminated by a plane wave with $\lambda = 532\,\mathrm{nm}$.

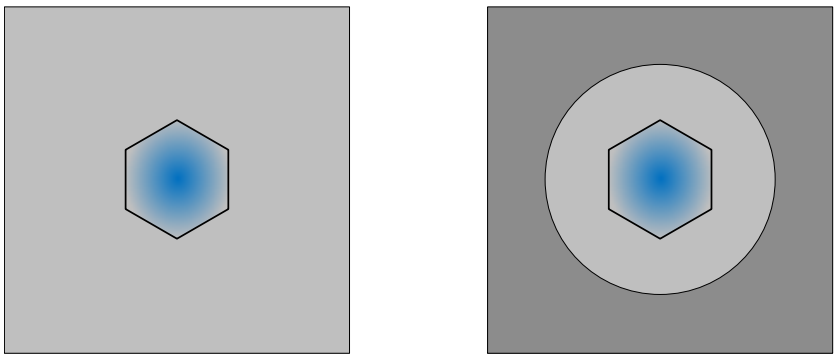

(a) (b)

Figure 6.20: The two configurations for extending the field for the ASPW calculations. (a): The amplitude and phase are continued by a constant value. (b): At a distance further than 25 µm a constant phase offset is introduced

approximately 50 µm.

Figures 6.19e and 6.19f show the field profile of the simulations when introducing a phase delay of $\Delta\phi = 0.095\pi$ to the field outside a circle of 50 µm around the lens as shown in figure 6.20b. This perturbation induces an interference pattern on the focal spot with some maxima and minima. At $z = 250\,\mu m$, there is an area of around 50 µm length with destructive interference. This is in agreement with the experimental findings. However, the intensity drop is not as strong and isolated as in the measurements and there are more local maxima and minima at shorter distances.

In order to get a more detailed picture, the intensity on the optical axis is displayed in 6.21. The upper part of the diagram shows the experimental data with the error bars being calculated as the standard deviation from the four measurements. All four lenses have a very similar field up to $z \approx 300\,\mu m$. At $z = 100\,\mu m$ up to 200 µm, the intensity oscillates slightly around a constant value before dropping to the earlier discussed minimum. For distances above 300 µm, the intensity profile of the four lenses are strongly disturbed by destructive and constructive diffraction orders from outside the lens. Small errors in the alignment have a strong effect on the interference pattern in this area which cause the large error bars.

The lower part of figure 6.21 displays the simulations for the ideal case and for the case where a phase delay has been introduced. The ideal case, marked with the solid line has similar characteristics to the elliptical microwave lens (Fig. 6.21). At distances before the interference pattern disturbs the signal in the experiments, the simulations are very similar to the measurements. The minimum at around $z = 25\,\mu m$ as well as the steep intensity increase have the same characteristics in both curves.

In the curve where a constant phase delay to the surrounding area was applied (dashed line), the intensity has a minimum at the same position as the experiment, however not as low and not as defined. Closer to the lens however, the intensity has much stronger oscillations than the experimental data.

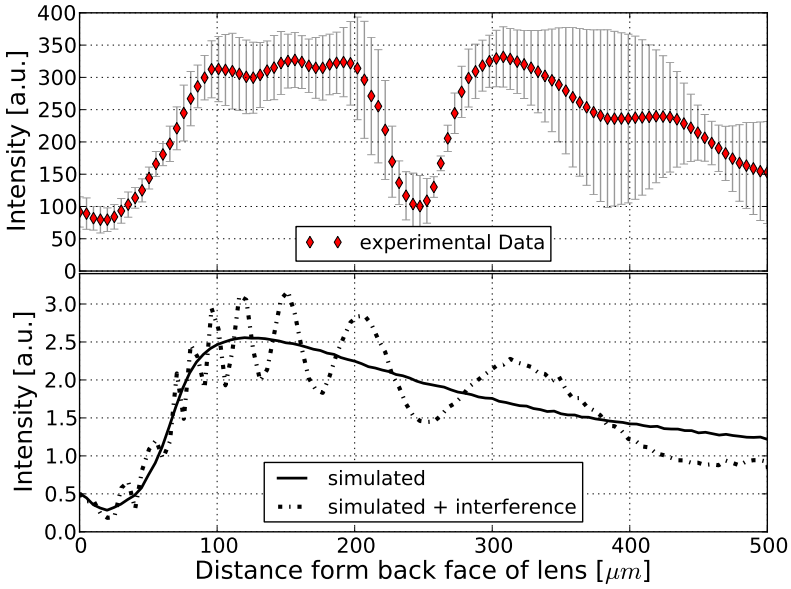

Figure 6.21: Intensity on the optical axis as a function of the distance to the back surface of the lens for $\lambda = 532\,\text{nm}$. The upper diagram shows the experimental data, in the lower diagram the simulations of the lens are displayed. The ideal case is marked by the solid line and the case where a phase offset was introduced is marked by the dashed line.

These simulations suggest that the filling material of the second last drawing step is probably causing the observed interferences. However, the simple picture of including a phase delay was not successful to fully explain the experimental phenomena. The simulations were carried out for a range of phase offsets and intensities. To determine the similarity with the experimental data, the intensity on the optical axes were compared. A phase only variation with $\Delta\phi = 0.095\pi$ gives the best agreement that could be achieved. Additionally, the effects of introducing only a 2 µm wide ring where the field was altered were investigated, which however did not lead to satisfying results. One reason for not seeing the intensity oscillations in the close field in the experiment could be that the phase might not change in one discrete step but continuously. This could result in several slightly different diffraction orders which average each other out at all positions apart from the big drop. Due to the wide range of possibilities that could influence the field, more experiments will have to be conducted to really understand the physics behind this problem and to be able to find an exact theoretical explanation.

From figure 6.21 the theoretical focal length of the faster axis is found to be $z = 120\,\mu\text{m}$. Figures 6.22a and 6.22b show the cross-sections of the beam with $\lambda = 532\,\text{nm}$ at this distance in x and in y direction respectively. The upper diagrams show the experimental data with error bars. In the lower diagrams, the results of the simulations are displayed. The two polarisations of the incident light nearly give the same intensity profile when comparing the theoretical and experimental data.

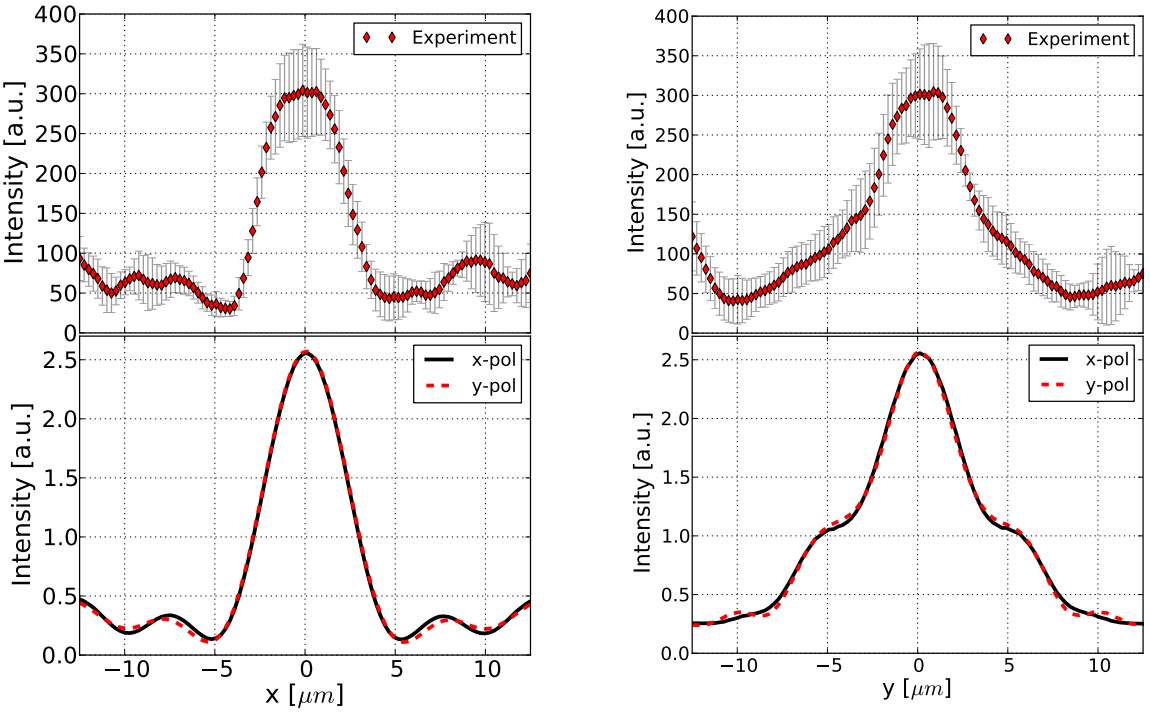

(a) (b)

Figure 6.22: Cross section through the focal plane along the x-axis (a) and the y-axis (b). The upper diagrams show the experimental data, in the lower diagram the simulations of x-polarised light (solid black line) and y-polarised light (dashed red line) are shown. In all cases, the wavelength of the illuminating light is $\lambda = 532\,\text{nm}$.

For both cross sections, the measured spot width and it characteristics are nearly identical to the predictions. In the experiment, the ratio between peak intensity and background level is lower than in the simulations, i.e. more light is diffracted into the sidelobes. The scattering effect becomes stronger for distances further away from the lens which, like the intensity drop on the optical axis in figure 6.21, is due to some external diffraction effects. Cross sections further away than the focus will have less or very little agreement between simulations and experiment.

The same experiments as for $\lambda = 532\,\text{nm}$ were conducted with a Helium Neon laser with wavelength $\lambda = 633\,\text{nm}$. Figures 6.23a and 6.23b show the xz and the yz cross sections of the measured field, and figures 6.23c and 6.23d show the results of the simulations for the ideal case, respectively. Here, the intensity also has a distinct minimum on the optical axis, but at a slightly closer distance $z = (230 \pm 30)\mu\text{m}$. The occurrence of this effect, when illuminating the same lenses with a different laser, confirms the earlier made conclusions, that the interference patterns are caused by the element and are not due to properties of the incident light.

The theoretical predictions show that the lens would perform worse for $\lambda = 633\,\text{nm}$ compared to $\lambda = 532\,\text{nm}$. In the direct comparison of the simulations in figure

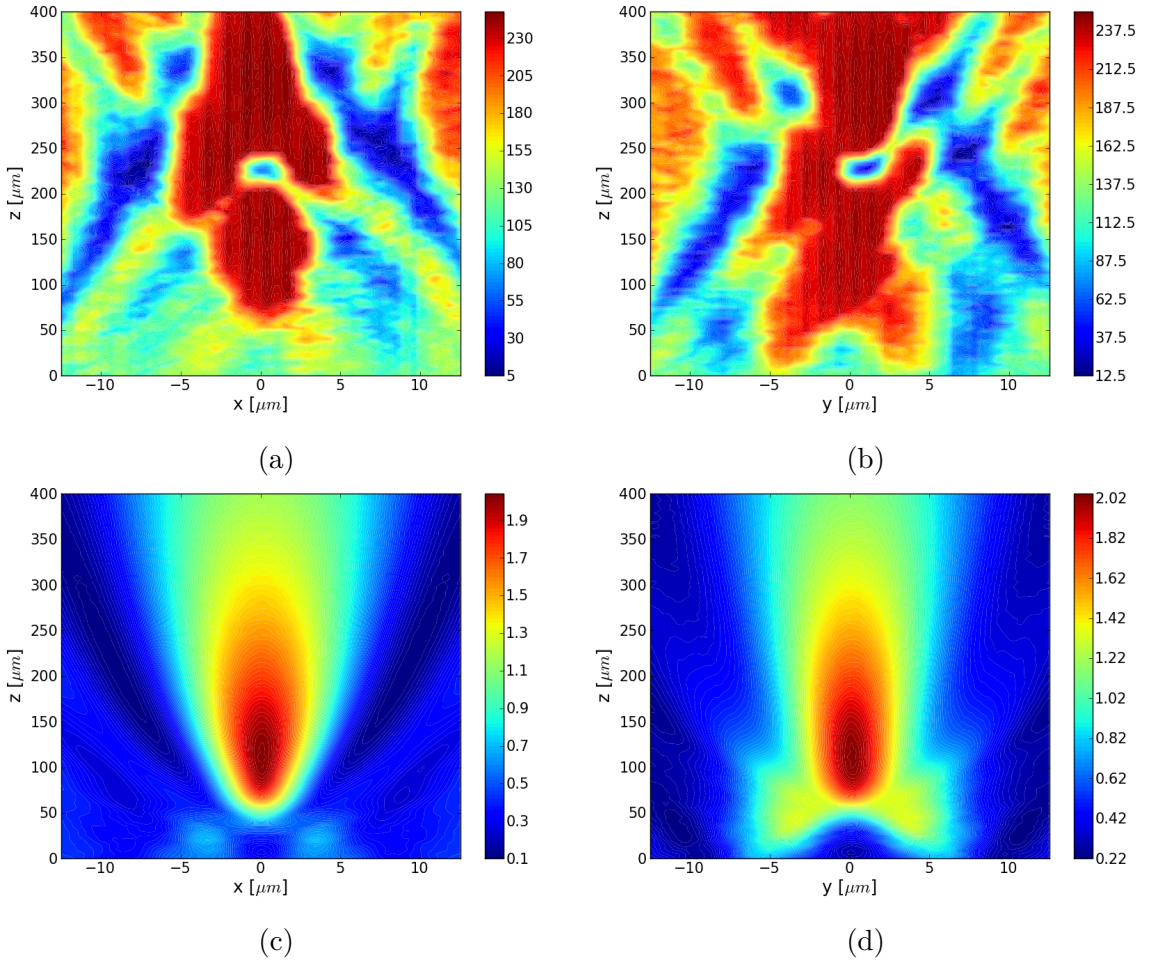

Figure 6.23: Intensity cross sections in the xz plane and yz plane of the measurements (a),(b) and the simulations in the ideal case (c), (d). The lens is illuminated by a plane wave with $\lambda = 633\,\text{nm}$.

6.14, the peak intensity for 633 nm is around 20% lower than for 532 nm. The cross sections of the simulations in figure 6.23 still show a nice lens like behaviour. In the experimental data however, the intensity of scattered light is much higher compared to the peak intensity than in the previous case with $\lambda = 532\,\text{nm}$.

Figure 6.24 shows the intensity distribution on the optical axis as a function of z. Simulations and experimental values do not agree well in this case. The steep increase of the intensity happens at the same distance for simulations and experiment. At distances $z > 100\,\mu\text{m}$, the experimental intensity remains nearly constant apart from a distinct drop between 200 µm and 250 µm. Analogue to the green light illumination, the simulations for red light result in an intensity drop at the same distance as the measured drop, when introducing a phase shift of $\Delta\phi = 0.095\pi$ in the area outside a circle with 50 µm diameter. Again, there is a stronger intensity oscillation for shorter distances and the drop at $z = 230\,\mu\text{m}$ is not as low as in the experiments.

Figure 6.25 shows the x and y cross sections through the focal plane at $z = 110\,\mu\text{m}$. The upper diagrams show the experimental data, the lower diagrams display the

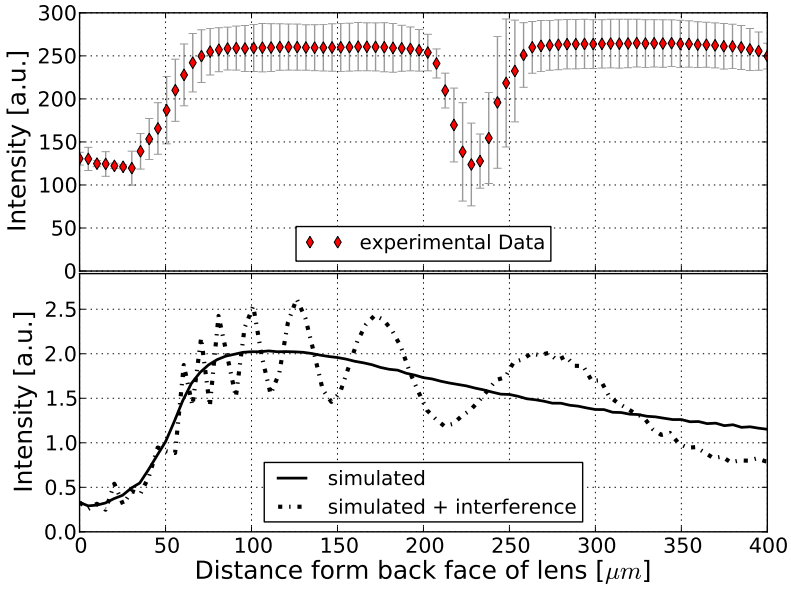

Figure 6.24: Intensity on the optical axis as a function of the distance to the back surface of the lens for $\lambda = 633\,\text{nm}$. The upper diagram shows the experimental data, in the lower diagram the simulations of the lens are displayed. The ideal case is marked by the solid line and the case where a phase offset was introduced is marked by the dashed line.

simulations for x and y polarised light. The ratio between the peak intensity and background signal is only around 2.5 as opposed to 8 as expected from the simulations. This shows, that much of the light is lost due to scattering. In the experimental curves, the central area of the focus is much flatter compared to the simulations and to the experiments for $\lambda = 532\,\text{nm}$. It is however, qualitatively apparent that the spot size along the x axis is smaller than along the y axis.

The theoretical characterisation of the elliptical microlens could confirm the validity of the effective medium theory. Comparisons of the theoretical performance of the NSGRIN lens with the target GRIN lens show very good agreement. For the simulations, the Fourier modal method was shown to be a very fast and efficient way to solve such low index contrast, sub-wavelength structures.

The phase measurements with the Mach-Zehnder interferometer, verified the theoretical phase of the transmitted field. Despite the fact that the interferometer is designed for lenses with diameters of $\geq 50\,\mu\text{m}$, reasonable results could be achieved.

The characterisation of the beam profile and focal area brought up some problems that will have to be solved in the fabrication of future elements. In the close proximity to the back surface of the lens, the measured intensity is very similar to the simulations. However, at distances beyond the focal length, the experimental field differs strongly from the predictions. A few indications could be found that these differences are due to interferences, induced from the surrounding of the lens. Similar

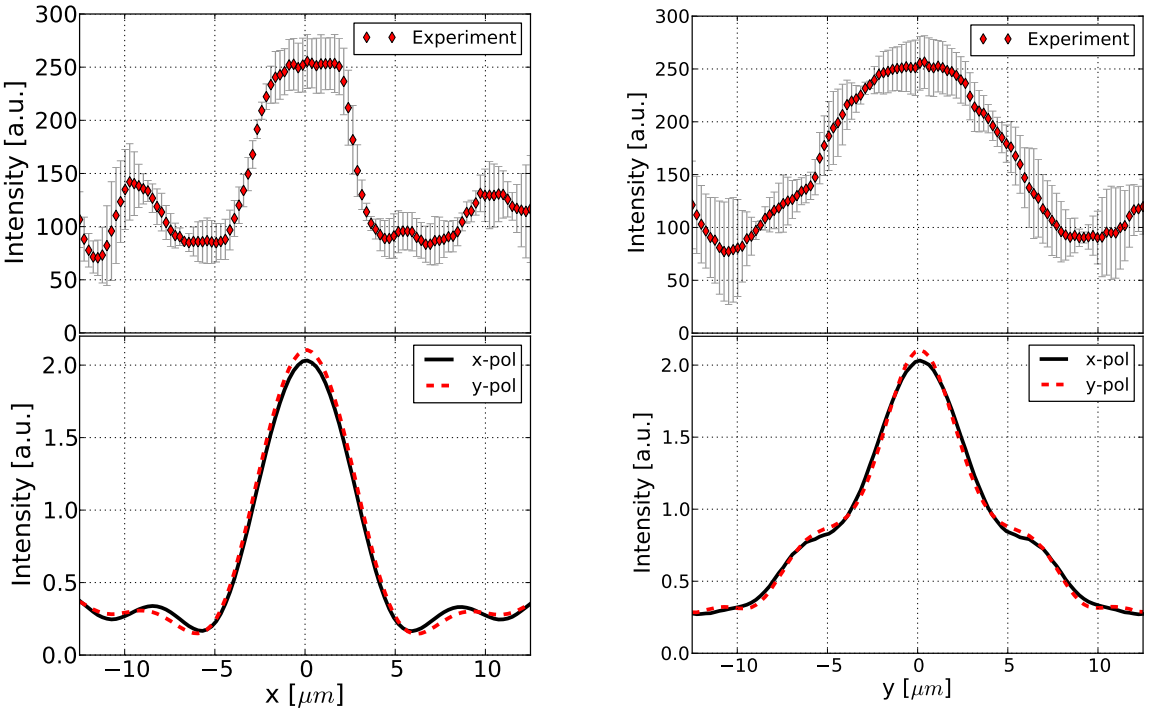

(a) (b)

Figure 6.25: Cross section through the focal plane along the x-axis (a) and the y-axis (b). The upper diagrams show the experimental data, in the lower diagram the simulations of x-polarised light (solid black line) and y-polarised light (dashed red line) are shown. In all cases, the wavelength of the illuminating light is $\lambda = 633\,\text{nm}$.

effects appeared for the two wavelengths, therefore these errors are introduced by the element and is not related to the incident beam.

Due to the small size of the microlenses it was not possible to use an aperture, which could prevent light to illuminate a large area around the microlens. Any pin hole thicker than a few micrometres would have already caused diffraction in the beam before the lens. This experiment shows that the surrounding material around the lens is crucial to its performance. For such small lenses with a diameter of around 16 µm and 120 µm thickness, diffraction on boundaries can cause non negligible effects, even if the refractive index modulation is very small.

In contrast to the predictions that NSGRIN structures perform better for larger wavelength to feature size ratios, the lens focuses green light ($\lambda = 532\,\text{nm}$) better than red light ($\lambda = 633\,\text{nm}$). This effect is seen in the simulations, and much stronger in the measurements. So far, only one sample has been fabricated to be tested, therefore it was not possible to investigate these phenomena further.

In actual applications however, only the lens will be illuminated, e.g. to collimate the light emitted by a diode laser. In these cases the surrounding material would have no influence on the transmitted light and would therefore be of no importance.

Chapter 7

Conclusion and Outlook

7.1 Conclusion

The work presented in this thesis covers theoretical and experimental investigations of nanostructured gradient index lenses. In this chapter the developments which have been presented will be summarised and possible further work is discussed.

Several nanostructured gradient index lenses were designed, fabricated and characterised theoretically and experimentally in the microwave regime and for the optical spectrum. Theoretical models have been derived and developed in order to be able to simulate one dimensional as well as two dimensional sub-wavelength structures.

The Fourier modal method for lamellar gratings as well as for crossed gratings was introduced in **Chapter 2**. It was developed from Maxwell's equations by decomposing the fields and permittivity to discrete Fourier series. The T-Matrix approach and the S-Matrix approach to calculate the boundary conditions were introduced, which can be used for both the 1D and the 2D Fourier modal method.

In **Chapter 3**, the field stitching algorithm for crossed gratings was introduced. It enables the rigorous analysis of very large gratings with sub-wavelength feature sizes. To further decrease the computation time a scheme was derived to exploit symmetric features in the grating structure. The numerical performance was shown to decrease the maximum memory requirements by a factor of $1/M^4$, if the grating is split into a regular grid of $M \times M$ sub-gratings. A second advantage of the field-stitching algorithm is the dramatically decreased computation time. A 2×2 splitting of the grating reduces the computation time by more than an order of magnitude compared to the standard FMM with the same spatial resolution. The validity of the field stitching algorithm was shown by means of an example of a diffractive element consisting of 32×32 pixels.

Chapter 4 covers various aspects of nano-structured gradient index materials. In the first part, the historic development of nano-structured elements was given, and

the equations of the effective medium theory were derived from Maxwell's equations. Furthermore, the main equations for gradient index lenses were introduced, which were used to evaluate the simulations and experiments on nanostructured gradient index lenses.

In the second section, the stack-and-draw technology to fabricate NSGRIN microlenses was described in detail. This technology was used to fabricate the microlenses that were characterised experimentally. All fabrication steps from the stacking of the initial preform and the various drawing stages are described. The final result are several metres of the NSGRIN structure which can bu cut and polished to a thickness of typically 100 µm to 250 µm.

The third section contains the design algorithm to find the required pattern with the same optical properties like a smooth gradient index element. It was shown, that the direct binary search algorithm converges much faster to a constant distribution compared to the simulated annealing algorithm with a finite start temperature. The best way of assigning the initial pattern for the design process was found to be a probabilistic approach which gives a distribution close to the optimum.

For the design of lamellar structures, a method to calculate the transmitted field of a non-periodic element was derived. In contrast to other approaches this method does not require modifications of FMM algorithm. The computational space for the transmitted field is increased to a period of several times the grating size for which the new transmission coefficients can be calculated by a simple formula. With the help of an example it was shown that the interference, which is induced by the periodic boundary conditions, can be suppressed by embedding the grating in a larger area with field intensity $I = 0$. In the presented example, an added frame of 6 times the diameter of the lens on either side results in an undisturbed transmitted field. This method was used in conjunction with the simulated annealing algorithm to design a multi layer lamellar lens for the microwave regime. The simulations were verified experimentally by characterising the designed lens with 5 mm pixel size and an illuminating wavelength of $\lambda = 3\,\mathrm{cm}$.

In **Chapter 5**, two structured GRIN lenses were tested in the microwave regime. Owing to the timely process of fabricating NSGRIN lenses for the optical regime, large models of the lenses were assembled using PTFE rods and tubes. The transmitted field of the spherical and the elliptical lens were compared to FDTD simulations of the structure as well as to simulation of the target GRIN lens. The spherical microwave lens, which was designed at an early stage of the project focuses the light. However, the focal length is shorter compared to the target, and the peak intensity is around 40% lower than expected from the ideal GRIN lens.

Simulations of the elliptical lens, which was designed with an improved design scheme, showed very good agreement between target and structure. The peak in-

tensity in the focus of the structured lens differs only by less than 5% compared to peak of the ideal refractive index profile. The characteristics of the experimental measurements are nearly identical to the simulations.

Chapter 6 covers theoretical and experimental characterisations of two NSGRIN lenses. The first element to be fabricated was an array of spherical micro lenses to prove the capabilities of the stack-and-draw technique to fabricate structures with large irregular patterns. The probe to be characterised contained lenses, that are too small to be tested for their focusing properties. FDTD simulations showed that light in these lenses would have propagation properties similar to a real grin lens.

The elliptical microlens was characterised in detail using a Mach-Zehnder interferometer for the phase and an imaging system to measure the focusing properties. The interferometric measurements showed good agreement with the simulations. The intensity measurements agree well with the simulations in the area up to a distance of 100 µm. At farther distances however, the experiments showed a strong interference pattern, which was not expected from the simulations. This effect is probably caused by interference from an area outside the lens where a different type of glass was used as filling material in one drawing step. The different refractive index in this area causes a phase offset and maybe some internal stress at the boundary which can effect the light propagation. However, the experimental results could not be reproduced perfectly in the simulations. More experimental and theoretical work will be conducted to thoroughly understand this system.

7.2 Future Work

When considering what further work should be undertaken, the suggestions can be categorised in four main themes: extending the FMM simulations, design of new structures, fabrication of NSGRIN lenses and their characterisation.

The FMM simulations were implemented in an object oriented way which makes it easy to add improvements and modifications to the standard algorithm. There are several possible approaches to improve the convergence of the Fourier modal method. For configurations such as the elliptical microwave lens (see Fig. 3.6b), the FMM converges only very slowly to a stable field distribution. The exploitations of symmetries, as suggested by Bai and Li, can improve the performance significantly. If the structure of the grating has mirror symmetry along the x-axis and the y-axis, the effective truncation rank is four times higher compared to the standard implementation [41]. Other symmetries such as rotational symmetry would increase the performance by the same amount [42]. These improvements would also be ideally suited to be used in conjunction with the field-stitching method.

As of now, only plane wave illumination has been used in the simulations of NSGRIN lenses. In order to be able to simulate systems such as the collimation of the light from diode lasers and waveguides, it would be necessary to implement point sources and other non-planar incident waves.

The field-stitching method, which has been derived in chapter 3, could be extended and tested more extensively. The required number of sub-gratings and their overlap is at the moment determined by an educated guess, or by trying several configurations. It might be possible to find a heuristic or an analytic approach to determine the best combination of number of sub-gratings and required overlap for a given grating. Furthermore, a detailed study on the use of differently sized sub-gratings would be interesting for the analysis of gratings, that combine areas with very small features and areas with relatively large features.

As of now, the main obstacle to analyse gratings with the Fourier modal method is the high memory requirement even when using the field-stitching algorithm. The available computer with 14 GB memory is just sufficient for a truncation rank of ± 28. A parallel implementation with distributed memory management could be run on a high performance cluster and increase the maximum possible truncation rank as well as reduce the computation time.

In this thesis the design of structures has so far been restricted to GRIN microlenses. Lu and Vučković [120] recently introduced an inverse design method of nanophotonic structures by using a complementary convex optimisation. With this algorithm, waveguides with very complex modes can be designed which could then be translated into a nanostructured binary refractive index pattern.

Form birefringence is an effect of the effective medium theory that describes dielectric lamellar subwavelength gratings which have a different effective index for TE and TM polarised light [121]. They therefore interact with light like a birefringent material. Elements with a high form birefringence could be fabricated by fusing slabs of two different glasses or by stacking rods to a lamellar pattern and draw the obtained preform to a feature size of less than half the wavelength of the incident light. Another way to achieve form birefringence was shown by Genereux et al. in 2001 [122]. Two dimensional photonic crystals show strong birefringent behaviour in the spectral range below the first photonic band edge, i.e. for large wavelengths compared to the pitch length. By drawing regular all solid photonic crystals from two glass types with a high refractive index contrast, a tailored birefringent material could easily be fabricated with the stack-and-draw technology.

Other possible new designs are multilevel refractive index structures, which are assembled from intermediate meta-rods. The meta-rods are intermediate post-preforms with an isotropic material distribution and a certain fill factor to create a constant

refractive index with a value somewhere between the refractive indices of the two glasses. This can be used to fabricate larger microlenses and for the mass production of scalar diffractive optical elements. This approach could be combined with from-birefringent pixels to create polarisation sensitive diffractive elements.

In order to get a better understanding of the effects that disturb the focusing, more experiments have to be conducted. In the first experiments on NSGRIN lenses, the intensity drop just after the focal plane is not fully understood yet, therefore it would be important to characterise other structures and find ways to suppress the interference effects that were found in the intensity characterisation.

As the NSGRIN microlenses are intended to be used for the collimation of diode lasers, an experimental test setup for point sources or other non-planar wave fronts would be very beneficial. Apertures with different shapes could be used to simulate the light emitting area of various different lasers.

Author's Journal Contributions

[1] F. Hudelist, R. Buczynski, A. J. Waddie, and M. R. Taghizadeh, *Design and fabrication of nano-structured gradient index microlenses*, Opt. Express **17**(5) (2009), 3255–3263.

[2] F. Hudelist, J. M. Nowosielski, R. Buczynski, A. J. Waddie, and M. R. Taghizadeh, *Nanostructured elliptical gradient-index microlenses*, Opt. Lett. **35**(2) (2010), 130–132.

[3] Florian Hudelist, Andrew J. Waddie, and Mohammad R. Taghizadeh, *Analysis of crossed gratings with large periods and small feature sizes by stitching of the electromagnetic field*, J. Opt. Soc. Am. A **26**(12) (2009), 2648–2653.

[4] Florian Hudelist, Andrew J. Waddie, and Mohammad R. Taghizadeh, *Design of all-glass multilayer phase gratings for cylindrical microlenses*, Opt. Lett. **34**(11) (2009), 1681–1683.

[5] Jedrzej M. Nowosielski, Ryszard Buczynski, Florian Hudelist, Andrew J. Waddie, and Mohammad R. Taghizadeh, *Nanostructured GRIN microlenses for Gaussian beam focusing*, Optics Communications **283**(9) (2010), 1938 – 1944.

Author's Conference Contributions

[1] F. Hudelist, A. J. Waddie, R. Busczynski, and M. R. Taghizadeh, *Design and fabrication of irregular sub-wavelength diffractive phase elements*, Photon08, 2008.

[2] F. Hudelist, A. J. Waddie, R. Busczynski, and M. R. Taghizadeh, *Simulation and optimisation methods for non-periodic subwavelength structures*, Micro-Optics 2008 6992(1), SPIE, 699210, 2008.

[3] F. Hudelist, A. J. Waddie, J. M. Nowosielski, R. Buczynski, and M. R. Taghizadeh, *Nanostructured graded index materials*, CLEO/Europe, 2009.

[4] T. Kämpfe, F. Hudelist, A. J. Waddie, M. R. Taghizadeh, E. Kley, and A. Tunnermann, *Comparison of different simulation methods for multiplane computer generated holograms*, Micro-Optics 2008 6992(1), SPIE, 69920M, 2008.

[5] I. Kujawa, A. Filipkowski, D. Pysz, F. Hudelist, A. Waddie, R. Stepien, R. Buczynski, and M. Taghizadeh, *Photonic glass: novel method for fabrication of volume 2d photonic crystals*, Optical Fibers and Their Applications 2008 7120(1), SPIE, 71200M, 2008.

References

[1] LG Cohen and MV Schneider. Microlenses for coupling junction lasers to optical fibers. *Appl. Opt.*, 13(1):89–94, 1974.

[2] CB Burckhardt. Diffraction of a Plane Wave at a Sinusoidally Stratified Dielectric Grating. *OSA*, 36(11):1502–1509, 1966.

[3] F.G. Kaspar. Diffraction by thick, periodically stratified gratings with complex dielectric constant. *J. Opt. Soc. Am. A*, 63(1):37–45, 1973.

[4] K. Knop. Rigorous diffraction theory for transmission phase gratings with deep rectangular grooves. *J. Opt. Soc. Am. A*, 68(9):1206–1210, 1978.

[5] M. G. Moharam and T. K. Gaylord. Diffraction analysis of dielectric surface-relief gratings. *J. Opt. Soc. Am.*, 72(10):1385–1392, 1982.

[6] MG Moharam and TK Gaylord. Rigorous coupled-wave analysis of planar-grating diffraction. *J. Opt. Soc. Am. A*, 71(7):811–818, 1981.

[7] M. G. Moharam and T. K. Gaylord. Three-dimensional vector coupled-wave analysis of planar-grating diffraction. *J. Opt. Soc. Am.*, 73(9):1105–1112, 1983.

[8] M. G. Moharam, Drew A. Pommet, Eric B. Grann, and T. K. Gaylord. Stable implementation of the rigorous coupled-wave analysis for surface-relief gratings: enhanced transmittance matrix approach. *J. Opt. Soc. Am. A*, 12(5):1077–1086, 1995.

[9] MG Moharam, E.B. Grann, D.A. Pommet, and TK Gaylord. Formulation for stable and efficient implementation of the rigorous coupled-wave analysis of binary gratings. *J. Opt. Soc. Am. A*, 12(5):1068–1076, 1995.

[10] J. Chandezon, G. Rauolt, and D. Maystre. A new theoretical method for diffraction gratings and its numerical application. *Journal of Optics*, 11(4):235–241, 1980.

[11] Chandezon, Dupuis, Cornet, and Maystre. Multicoated gratings: a differential formalism applicable in the entire optical region. *J. Opt. Soc. Am. A*, 72(7):839–846, 1982.

[12] G. Granet, J. Chandezon, J.P. Plumey, and K. Raniriharinosy. Reformulation of the coordinate transformation method through the concept of adaptive spatial resolution. Application to trapezoidal gratings. *J. Opt. Soc. Am. A*, 18(9):2102–2108, 2001.

[13] Joshua N. Winn John D. Joannopoulos, Robert David Meade. *Photonic crystals : molding the flow of light*. Princeton University Press, 2nd edition, 2008.

[14] Daniel Courjon. *Near-field microscopy and near-field optics*. Imperial College Press, London, 2003.

[15] L. Li. Justification of matrix truncation in the modal methods of diffraction gratings. *J. Opt. A: Pure Appl. Opt*, 1:531–536, 1999.

[16] G. Granet and B. Guizal. Efficient implementation of the coupled-wave method for metallic lamellar gratings in TM polarization. *J. Opt. Soc. Am. A*, 13(5):1019–1023, 1996.

[17] P. Lalanne and G.M. Morris. Highly improved convergence of the coupled-wave method for TM polarization. *J. Opt. Soc. Am. A*, 13(4):779–784, 1996.

[18] Antoni Zygmund. *Trigonometric Series*, volume 1&2. Cambridge University Press, 3rd edition, 2002.

[19] L. Li. Use of Fourier series in the analysis of discontinuous periodic structures. *J. Opt. Soc. Am. A*, 13(9):1870–1876, 1996.

[20] D.Y.K. Ko and J.R. Sambles. Scattering matrix method for propagation of radiation in stratified media: attenuated total reflection studies of liquid crystals. *J. Opt. Soc. Am. A*, 5(11):1863, 1988.

[21] N. P. K. Cotter, T. W. Preist, and J. R. Sambles. Scattering-matrix approach to multilayer diffraction. *J. Opt. Soc. Am. A*, 12(5):1097–1103, 1995.

[22] Lifeng Li. Formulation and comparison of two recursive matrix algorithms for modeling layered diffraction gratings. *J. Opt. Soc. Am. A*, 13(5):1024–1035, 1996.

[23] Lifeng Li. Note on the S-matrix propagation algorithm. *J. Opt. Soc. Am. A*, 20(4):655–660, 2003.

[24] Hwi Kim, Il-Min Lee, and Byoungho Lee. Extended scattering-matrix method for efficient full parallel implementation of rigorous coupled-wave analysis. *J. Opt. Soc. Am. A*, 24(8):2313–2327, 2007.

[25] Eng Leong Tan. Note on formulation of the enhanced scattering- (transmittance-) matrix approach. *J. Opt. Soc. Am. A*, 19(6):1157–1161, 2002.

[26] D. M. Pai and K. A. Awada. Analysis of dielectric gratings of arbitrary profiles and thicknesses. *J. Opt. Soc. Am. A*, 8(5):755–762, 1991.

[27] Lifeng Li. Bremmer series, R-matrix propagation algorithm, and numerical modeling of diffraction gratings. *J. Opt. Soc. Am. A*, 11(11):2829–2836, 1994.

[28] Benfeng Bai, Yuri Svirko, Jari Turunen, and Tuomas Vallius. Optical activity in planar chiral metamaterials: Theoretical study. *Phys. Rev. A*, 76(2):023811, Aug 2007.

[29] R. Bräuer and O. Bryngdahl. Electromagnetic diffraction analysis of two-dimensional gratings. *Opt. Commun.*, 100(1-4):1 – 5, 1993.

[30] Eero Noponen and Jari Turunen. Eigenmode method for electromagnetic synthesis of diffractive elements with three-dimensional profiles. *J. Opt. Soc. Am. A*, 11(9):2494–2502, 1994.

[31] Philippe Lalanne. Improved formulation of the coupled-wave method for two-dimensional gratings. *J. Opt. Soc. Am. A*, 14(7):1592–1598, 1997.

[32] L. Li. Reformulation of the Fourier modal method for surface-relief gratings made with anisotropic materials. *J. Mod. Opt.*, 45(7):1313–1334, 1998.

[33] Lifeng Li. Fourier modal method for crossed anisotropic gratings with arbitrary permittivity and permeability tensors. *J. Opt. A: Pure and Appl. Opt*, 5(4):345, 2003.

[34] G. Granet and J.-P. Plumey. Parametric formulation of the Fourier modal method for crossed surface-relief gratings . *J. Opt. A: Pure and Appl. Opt*, 4:145–+, September 2002.

[35] T. Vallius and M. Honkanen. Reformulation of the Fourier modal method with adaptive spatial resolution: application to multilevel profiles. *Opt. Express*, 10(1):24–34, 2002.

[36] E. Popov, M. Neviere, and N. Bonod. Factorization of products of discontinuous functions applied to Fourier-Bessel basis. *J. Opt. Soc. Am. A*, 21(1):46–52, 2004.

[37] T. Schuster, J. Ruoff, N. Kerwien, S. Rafler, and W. Osten. Normal vector method for convergence improvement using the RCWA for crossed gratings. *J. Opt. Soc. Am. A*, 24(9):2880–2890, 2007.

[38] B Bai and L Li. Reduction of computation time for crossed-grating problems: a group-theoretic approach. *J. Opt. Soc. Am. A*, 21(10):1886–1894, 2004.

[39] Benfeng Bai and Lifeng Li. Group-theoretic approach to the enhancement of the Fourier modal method for crossed gratings: C2 symmetry case. *J. Opt. Soc. Am. A*, 22(4):654–661, 2005.

[40] B. Bai and L. Li. Group-theoretic approach to enhancing the Fourier modal method for crossed gratings of plane group p3. *J. Mod. Opt.*, 52:1619–1634, November 2005.

[41] B. Bai and L. Li. Group-theoretic approach to enhancing the Fourier modal method for crossed gratings with one or two reflection symmetries. *Journal of Optics-A-Pure and Applied Optics*, 7(7):271–278, 2005.

[42] Benfeng Bai and Lifeng Li. Group-theoretic approach to enhancing the Fourier modal method for crossed gratings with C4 symmetry. *J. Opt. A: Pure and Appl. Opt*, 7(12):783–789, 2005.

[43] Benfeng Bai and Lifeng Li. Group-theoretic approach to enhancing the Fourier modal method for crossed gratings with square symmetry. *J. Opt. Soc. Am. A*, 23(3):572–580, 2006.

[44] Lifeng Li. New formulation of the fourier modal method for crossed surface-relief gratings. *J. Opt. Soc. Am. A*, 14(10):2758–2767, 1997.

[45] B. Layet and M.R. Taghizadeh. Analysis of gratings with large periods and small feature sizes by stitching of the electromagnetic field. *Opt. Lett.*, 21:1508–1510, 1996.

[46] B. Layet and M.R. Taghizadeh. Electromagnetic analysis of fan-out gratings and diffractive cylindrical lens arrays by field stitching. *J. Opt. Soc. Am. A*, 14:1554–1561, 1997.

[47] Dennis W. Prather, Shouyuan Shi, and Jonathan S. Bergey. Field stitching algorithm for the analysis of electrically large diffractive optical elements. *Opt. Lett.*, 24(5):273–275, 1999.

[48] Born and Wolf. *Principles of Optics*. Cambridge University Press, 7 edition, 1999.

[49] TBCI. http://plasimo.phys.tue.nl/TBCI/.

[50] E. Anderson, Z. Bai, C. Bischof, S. Blackford, J. Demmel, J. Dongara, J. Du Croz, A. Greenbaum, S. Hammarling, A. McKenney, and D. Sorensen. *LAPACK Users' Guide*. Siam, http://www.netlib.org/lapack/lapack_lug.html, 3rd edition, 1999.

[51] Ari Sihvola. *Electromagnetic mixing formulas and applications*. Institution of Electrical Engeneers, London, UK, 1999.

[52] A. Yariv and P. Yeh. Electromagnetic propagation in periodic stratified media. II. Birefringence, phase matching, and x-ray lasers. *Phys. Lett*, 28:735, 1976.

[53] Dale C. Flanders. Submicrometer periodicity gratings as artificial anisotropic dielectrics. *Appl. Phys. Lett.*, 42(6):492–494, 1983.

[54] R.C. Enger and S.K. Case. Optical elements with ultrahigh spatial-frequency surface corrugations. *Appl. Opt.*, 22(20):3220–3228, 1983.

[55] W. Stork, N. Streibl, H. Haidner, and P. Kipfer. Artificial distributed-index media fabricated by zero-order gratings. *Opt. Lett.*, 16(24):1921–1923, 1991.

[56] Michael W. Farn. Binary gratings with increased efficiency. *Appl. Opt.*, 31(22):4453–4458, 1992.

[57] Gene Campbell and Raymond K. Kostuk. Effective-medium theory of sinusoidally modulated volume holograms. *J. Opt. Soc. Am. A*, 12(5):1113, 1995.

[58] E.B. Grann, MG Moharam, and D.A. Pommet. Artificial uniaxial and biaxial dielectrics with use of two-dimensional subwavelength binary gratings. *J. Opt. Soc. Am. A*, 11(10):2695–2703, 1994.

[59] H. Kikuta, Y. Ohira, H. Kubo, and K. Iwata. Effective medium theory of two-dimensional subwavelength gratings in the non-quasi-static limit. *J. Opt. Soc. Am. A*, 15(6):1577–1585, 1998.

[60] L. Pajewski, R. Borghi, G. Schettini, F. Frezza, and M. Santarsiero. Design of a binary grating with subwavelength features that acts as a polarizing beam splitter. *Appl. Opt.*, 40(32):5898–5905, 2001.

[61] W. Yu, T.i Konish, T. Hamamoto, H. Toyota, T. Yotsuya, and Y. Ichioka. Polarization-multiplexed diffractive optical elements fabricated by subwavelength structures. *Appl. Opt.*, 41(1):96–100, 2002.

[62] Mark S. Mirotznik, David M. Pustai, Dennis W. Prather, and Joseph N. Mait. Design of two-dimensional polarization-selective diffractive optical elements with form-birefringent microstructures. *Appl. Opt.*, 43(32):5947–5954, 2004.

[63] Uriel Levy, Chia-Ho Tsai, Hyo-Chang Kim, and Yeshaiahu Fainman. Design, fabrication and characterization of subwavelength computer-generated holograms for spot array generation. *Opt. Express*, 12(22):5345–5355, 2004.

[64] Uriel Levy, Hyo-Chang Kim, Chia-Ho Tsai, and Yeshaiahu Fainman. Near-infrared demonstration of computer-generated holograms implemented by using subwavelength gratings with space-variant orientation. *Opt. Lett.*, 30(16):2089–2091, 2005.

[65] Frederick T. Chen and Harold G. Craighead. Diffractive lens fabricated with mostly zeroth-order gratings. *Opt. Lett.*, 21(3):177–179, 1996.

[66] Joseph N. Mait, Dennis W. Prather, and Mark S. Mirotznik. Binary subwavelength diffractive-lens design. *Opt. Lett.*, 23(17):1343–1345, 1998.

[67] Joseph N. Mait, Dennis W. Prather, and Mark S. Mirotznik. Design of binary subwavelength diffractive lenses by use of zeroth-order effective-medium theory. *J. Opt. Soc. Am. A*, 16(5):1157–1167, 1999.

[68] Joseph N. Mait, Axel Scherer, Oliver Dial, Dennis W. Prather, and Xiang Gao. Diffractive lens fabricated with binary features less than 60 nm. *Opt. Lett.*, 25(6):381–383, 2000.

[69] Di Feng, Pan Ou, Li-Shuang Feng, Shu-Ling Hu, and Chun-Xi Zhang. Binary sub-wavelength diffractive lenses with long focal depth and high transverse resolution. *Opt. Express*, 16(25):20968–20973, 2008.

[70] Di Feng, Ningfang Song, Lishuang Feng, Pan Ou, and Chunxi Zhang. Generation of an extended depth of focus using diffractive micro-lenses with binary structures in the non-paraxial domain. *J. Opt. A: Pure and Appl. Opt*, 11(6):065704 (8pp), 2009.

[71] Philippe Lalanne, Simion Astilean, Pierre Chavel, Edmond Cambril, and Huguette Launois. Design and fabrication of blazed binary diffractive elements with sampling periods smaller than the structural cutoff. *J. Opt. Soc. Am. A*, 16(5):1143–1156, 1999.

[72] Christophe Sauvan, Philippe Lalanne, and Mane-Si Laure Lee. Broadband blazing with artificial dielectrics. *Opt. Lett.*, 29(14):1593–1595, 2004.

[73] Céline Ribot, Philippe Lalanne, Mane-Si-Laure Lee, Brigitte Loiseaux, and Jean-Pierre Huignard. Analysis of blazed diffractive optical elements formed with artificial dielectrics. *J. Opt. Soc. Am. A*, 24(12):3819–3826, 2007.

[74] Robert Halir, Pavel Cheben, Siegfried Janz, Dan-Xia Xu, Inigo Molina-Fernández, and Juan G. Wangüemert-Pérez. Waveguide grating coupler with subwavelength microstructures. *Opt. Lett.*, 34(9):1408–1410, 2009.

[75] Przemek J. Bock, Pavel Cheben, Jens H. Schmid, André Delâge, Dan-Xia Xu, Siegfried Janz, and Trevor J. Hall. Sub-wavelength grating mode transformers in silicon slab waveguides. *Opt. Express*, 17(21):19120–19133, 2009.

[76] Lifshitz Landau. *Electrodynamics of Continuous Media*. Pergamon Press, 1960.

[77] A. Taflove and S.C. Hagness. *Computational Electrodynamics: The Finite-Difference Time-Domain Method*. Artech House, Norwood, MA, 2005.

[78] W.D. Niven and C.H. Dwight. The Scientific Papers of James Clerk Maxwell. *American Journal of Physics*, 35:361, 1967.

[79] Duncan T. Moore. Gradient-index optics: a review. *Appl. Opt.*, 19(7):1035–1038, 1980.

[80] M. Bass. *Handbook of Optics, chapter 9*, volume 2. McGraw-Hill Professional, 2000.

[81] C. Gomez-Reino, M. V. Perez, and C. Bao. *Gradient-Index Optics - Fundamentals and Applications*. Springer, 2002.

[82] Joseph C. Palais. Fiber coupling using graded-index rod lenses. *Appl. Opt.*, 19(12):2011–2018, 1980.

[83] W. J. Tomlinson. Applications of grin-rod lenses in optical fiber communication systems. *Appl. Opt.*, 19(7):1127–1138, 1980.

[84] Miao He, Xiaocong Yuan, Nam Q. Ngo, Wai C. Cheong, and Jing Bu. Reflow technique for the fabrication of an elliptical microlens array in sol-gel material. *Appl. Opt.*, 42(36):7174–7178, 2003.

[85] Eugene Hecht. *Optics*. Addison Wesley, 4 edition, 2002.

[86] Takaaki Ishigure and Yusuke Takeyoshi. Polymer waveguide with 4-channel graded-index circular cores for parallel optical interconnects. *Opt. Express*, 15(9):5843–5850, 2007.

[87] Risto-Pekka Salmio, Jyrki Saarinen, Jari Turunen, and Ari Tervonen. Graded-index diffractive elements by thermal ion exchange in glass. *Appl. Phys. Lett.*, 66(8):917–919, 1995.

[88] Lv Hao, Bangren Shi, Jijiang Wu, Lijun Guo, and Aimei Liu. Fabrication of gradient refractive index ball lenses using the method of combination of ion exchanging and sagging. *Opt. Commun.*, 276:310–316, AUG 15 2007.

[89] Dmitry K. Tagantsev, Andrey A. Lipovskii, Peter C. Schultz, and Boris V. Tatarintsev. Phosphate glasses for grin structures by ion exchange. *J. Non-Cryst. Solids*, 354(12-13):1142 – 1145, 2008. Proceedings of the 2005 International Conference on Glass - In conjunction with the Annual Meeting of the International Commission on Glass.

[90] Rui-Li Huang, Shen-Kang Ruan, Zhen-Chuan Kang, and Mian-Zeng Su. Radial gradient-index glass prepared by the sol-gel process. *Mater. Res. Bull.*, 30(5):543 – 548, 1995.

[91] S.N. Houde-Walter and D.T. Moore. Gradient-index profile control by field-assisted ion exchange in glass. *Appl. Opt.*, 24(24):4326–4333, 1985.

[92] Dmitry K. Tagantsev, Andrey A. Lipovskii, Peter C. Schultz, and Boris V. Tatarintsev. Phosphate glasses for GRIN structures by ion exchange. *J. Non-Cryst. Solids*, 354(12-13):1142–1145, 2008.

[93] Warren J. Smith. *Modern optical engineering: the design of optical systems.* McGraw-Hill Professional, 4 edition, 2007.

[94] J.C. Knight. Photonic crystal fibres. *Nature*, 424(6950):847–851, 2003.

[95] Xian Feng, Tanya Monro, Periklis Petropoulos, Vittoria Finazzi, and Dan Hewak. Solid microstructured optical fiber. *Opt. Express*, 11:2225–2230, 2003.

[96] F. Luan, A. K. George, T. D. Hedley, G. J. Pearce, D. M. Bird, J. C. Knight, and P. St. J. Russell. All-solid photonic bandgap fiber. *Opt. Lett.*, 29:2369–2371, 2004.

[97] D. Lorenc, M. Aranyosiova, R. Buczynski, R. Stepien, I. Bugar, A. Vincze, and D. Velic. Nonlinear refractive index of multicomponent glasses designed for fabrication of photonic crystal fibers. *Appl. Phys. B: Lasers Opt.*, pages 531–538, 2008.

[98] T Huang, Z.X. Li, M. Li, D.G. Chetwynd, and C.M. Gosselin. Conceptual design and dimensional synthesis of a novel 2-DOF translational parallel robot for pick-and-place operations. *Journal of Mechanical Design*, 126:449–455, 2004.

[99] Kiam Heong Ang, G. Chong, and Yun Li. Pid control system analysis, design, and technology. *Control Systems Technology, IEEE Transactions on*, 13(4):559 – 576, july 2005.

[100] S. Kirkpatrick, CD Gelatt Jr, and MP Vecchi. Optimization by Simulated Annealing. *Science*, 220:671, 1983.

[101] V. Černỳ. Thermodynamical approach to the traveling salesman problem: An efficient simulation algorithm. *Journal of Optimization Theory and Applications*, 45(1):41–51, 1985.

[102] P. Salamon, P. Sibani, and R. Frost. *Facts, conjectures, and improvements for simulated annealing*. Society for Industrial Mathematics, 2002.

[103] Yongqi Fu, Ngoi Kok Ann Bryan, and Ong Nan Shing. Integrated micro-cylindrical lens with laser diode for single-mode fiber coupling. *Photonics Technology Letters, IEEE*, 12(9):1213–1215, 2000.

[104] J. F. Monjardin, K. M. Nowak, H. J. Baker, and D. R. Hall. Correction of beam errors in high power laser diode bars and stacks. *Opt. Express*, 14(18):8178–8183, 2006.

[105] D.P. Shepherd, S.J. Hettrick, C. Li, J.I. Mackenzie, R.J. Beach, S.C. Mitchell, and H.E. Meissner. High-power planar dielectric waveguide lasers. *J. Phys. D: Appl. Phys.*, 34(16):2420–2432, 2001.

[106] M. Ares, S. Royo, and J. Caum. Shack-Hartmann sensor based on a cylindrical microlens array. *Opt. Lett.*, 32(7):769–771, 2007.

[107] A. Nakai, K. Matsumoto, and I. Shimoyama. A stereoscopic display with a vibrating microlens array. In *Micro Electro Mechanical Systems, 2002*, pages 524–527, 2002.

[108] C. H. Lin, L. Jiang, Y. H. Chai, H. Xiao, S. J. Chen, and H. L. Tsai. Fabrication of microlens arrays in photosensitive glass by femtosecond laser direct writing. *Appl. Phys. A - Mat. Sci& Proc.*, 97(4):751–757, 2009.

[109] Eric G. Johnson and Mustafa A. G. Abushagur. Microgenetic-algorithm optimization methods applied to dielectric gratings. *J. Opt. Soc. Am. A*, 12(5):1152–1160, 1995.

[110] Jean Paul Hugonin and Philippe Lalanne. Perfectly matched layers as nonlinear coordinate transforms: a generalized formalization. *J. Opt. Soc. Am. A*, 22(9):1844–1849, 2005.

[111] R.F. Harrington. *Field Computation by Moment Methods*. Krieger Publishing Co., Inc. Melbourne, FL, USA, 1982.

[112] J.H. Li, G.J. Burke, D.A. White, C.A. Thompson, and K.J. Webb. Design of near-field irregular diffractive optical elements using a multi-resolution direct binary search method. *Opt. Lett.*, 31(9):1181–1183, 2006.

[113] T. Shimizu and Y. Kobayashi. Millimeter wave measurements of some low-loss dielectric plates by a novel cut-off circular waveguide method. *32nd European Microwave Conference*, 32:825–828, 2002.

[114] UC Hasar and O. Simsek. An accurate complex permittivity method for thin dielectric materials. *Progress In Electromagnetics Research*, 91:123–138, 2009.

[115] Jerzy Krupka, Krzysztof Derzakowski, Bill Riddle, and James Baker-Jarvis. A dielectric resonator for measurements of complex permittivity of low loss dielectric materials as a function of temperature. *Meas. Sci. Technol.*, 9(10):1751–1756, 1998.

[116] S.G. Johnson, J.D. Joannopoulos, and M. Soljacic. Meep. http://ab-initio.mit.edu/wiki.

[117] ZS Sacks, DM Kingsland, R Lee, and JF Lee. A Perfectly Matched anisotropic absorber for use as an absorbing boundary condition. *IEEE T. Antenn. Propag.*, 43:1460–1463, 1995.

[118] J. Jahns and K.-H. Brenner, editors. *Microoptics: from technology to applications*. Springer, New York, 2004.

[119] H. Sickinger. *Charakterisierung von sphärischen und zylindrischen Mikrolinsen mit einem Mach-Zehnder Interferometer*. PhD thesis, Friedrich-Alexander-Universität Erlangen-Nürnberg. Naturwissenschaftliche Fakultät, 2001.

[120] Jesse Lu and Jelena Vuckovic. Inverse design of nanophotonic structures using complementary convex optimization. *Opt. Express*, 18(4):3793–3804, 2010.

[121] R. Bräuer and O. Bryngdahl. Design of antireflection gratings with approximate and rigorous methods. *Appl. Opt.*, 33(34):7875, 1994.

[122] F. Genereux, S. W. Leonard, H. M. van Driel, A. Birner, and U. Gösele. Large birefringence in two-dimensional silicon photonic crystals. *Phys. Rev. B*, 63(16):161101, Apr 2001.